EEMAGINE - MEDICAL IMAGING SOLUTIONS GMBH

Functional Imaging based on swLORETA and phase synchronization

Author:

Ernesto Palmero Soler

Supervisor:

Prof. Dr. Jens Haueisen

SUBMITTED IN PARTIAL FULLFILMENT OF THE REQUIREMENTS FOR THE DEGREE OF

DOCTOR IN SCIENCE

May 18, 2010

To my family, especially
To my parents, Lourdes and Emilio
To my grandparents, Margarita and Angelo
To my angel of every day, Esther

Acknowledgements

In my experience, a PhD work is not possible without the help of many people, some of whom are not even aware of their contribution. For that reason and taking advantage of the synchronization between my brain and my heart I would like to thank to:

my colleagues at EEMAGINE for their kindness and support, especially to Jacob Kanev and Christoph Demmer who always have a word of comfort and understanding.

my friend Frank Zanow. I really enjoyed to work and talk with him and, in general, he and his family made the distance to my homeland shorter.

to my first supervisor in neuroscience research and personal friend Nelson Trujillo, for his invaluable comments and support during more that 7 years, for clearing up the clouds during obscure times.

especially, I thank my friend Eduardo Aubert who has shared his knowledge and wisdom and has been always there for me.

Particularly fruitful has been the collaboration with my friend Kevin Dolan who introduced me to the art of C++ programming and signal processing and with whom I have spend many hours enjoying good movies and food.

The time spend with my former colleagues at the Research Center Juelich Dr. Jurgen Dammers and Andrea Muren was a very useful one. Specially, Andrea Muren's ability with the MEG system was of invaluable help.

I greatly valuable Prof. Dr. Jens Haueisen for supervising my work.

My whole-life friend and teacher Jesus Novoa Blanco who introduced me to science when I was still a kid and forever became a beacon during dark hours and a constant memory in my mind.

To my family, specially my brother Emilio, who have educated, sheltered and supported me in all aspects of my life.

To my parents Lourdes and Emilio not only for the obvious reason of giving me the Life, but also for giving me the best of their life and supporting me even when I was an stubborn child: this thesis is dedicated to them.

I breathless thank to my grandparents Margarita and Angelo for their care and great advice which

have helped me throughout the worst moments of my life.

I would like to thanks Esther Alonso for helping review this manuscript.

Abstract

In order to overcome some of the limitations of the distributed inverse solution algorithms, a new algorithm named Standardized Weighted Low Resolution Tomography (swLORETA) was developed. The swLORETA algorithm incorporates a singular value decomposition (SVD) based lead field weighting to compensate the tendency of the linear inverse procedures in general, and sLORETA in particular, to reconstruct the sources close to the location of the sensors. It also contributes to decrease the sensitivity of the solution to the presence of noise. An extension of the swLORETA to the time-frequency domain was also developed by applying the Hilbert transform to the time series obtained with the swLORETA. Finally, the coherence and phase synchronization imaging methods were introduced to assess functional connectivity within the brain.

The tomographic properties of swLORETA and sLORETA were compared using both simulated and real data. In the simulation studies, the reconstruction of single and multiple current dipoles was simulated varying their position and orientation across the source space and taking into account the presence of noise. The real data was obtained from healthy subjects who performed a classical spatial attention experiment. The tests performed demonstrated that the resulting algorithm is not only efficient but also accurate as demonstrated by the analysis of a spatial attention experiment.

Zusammenfassung

In dieser Arbeit wird ein neuer Algorithmus, Standardized Weighted Low Resolution Tomography (swLORETA) genannt, vorgestellt, der einige der Beschränkungen von verteilten Lösungen für eine Quellenlokalisation beseitigt.

Der swLORETA-Algorithmus enthält eine Wichtung für das Leitungsfeld, das auf eine singular value decomposition (SVD) basiert. Damit wird die Tendenz der linearen Quellenlokalisation im Allgemeinen und von sLORETA im Besonderen, die Quellen zu nahe zu den Sensorpositionen zu lokalisieren, kompensiert. Die veränderte Wichtung trägt auch zu einer Abnahme der Rausch-Empfindlichkeit der Lösung bei. Eine Erweiterung von swLORETA in den Zeit-Frequenz-Bereich wurde entwickelt. Dies geschah durch Anwendung der Hilbert-Transformation auf Zeitreihen, die durch swLORETA erzeugt wurden. Schlieβlich wurden Bildgebungsmethoden für die Kohärenz und die Phasen-Synchronisation eingeführt, um die funktionalen Verbindungen im Gehirn zu untersuchen.

Die tomographischen Eigenschaften von swLORETA und sLORETA wurden mit Hilfe simulierter und realer Daten verglichen. In den Simulations-Studien wurde die Rekonstruktion von einzelnen wie multiplen Dipolen bei Berücksichtigung von Rauschen simuliert, wobei sowohl die Position als auch die Orientierung variiert wurde. Die realen Daten wurden von gesunden Probanden aufgenommen, die ein klassisches räumliches Aufmerksamkeits-Experiment ausführten. Die Testergebnisse dieses Experiments zeigen, dass der Algorithmus nicht nur effizient arbeitet, sondern auch genaue Resultate zur Analyse derartiger Experimente liefert.

Contents

List of Figures

List of Tables

Nomenclature

Abbreviations

ECD equivalent current dipole

EEG/MEG electroencephalography and/or magnetoencephalography signals

EMG electromiogram signals

fMRI functional magnetic image

GCV generalized cross-validation

MN minimum norm inverse solution method

PCD primary current density

PET Positron Emission Tomography

PMAP probabilistic maps

sLORETA standardized Low Resolution Tomography

SNR signal to noise ratio

SPMs statistical parametric maps

SVD singular value decomposition

swLORETA standardized weighted Low Resolution Tomography

Mathematical Symbols

α regularization parameter

$\arg$ complex argument function

$\cdot$ scalar product

ϵ permittivity

$\hat{H}$ Hilbert transform

$\mathbf{A}_{ij}$ denote the (i, j) element of matrix $\mathbf{A}$

$\mathbf{a}_i$ denote the ith element of vector $\mathbf{a}$

$\mathbf{B}$ magnetic field vector

$\mathbf{D}$ electric displacement field

$\mathbf{d}$ EEG/MEG signal vector

$\mathbf{E}$ electric field vector

$\mathbf{H}$ magnetizing field

$\mathbf{I}_n$ identity matrix of dimension $n \times n$

$\mathbf{J}$ total current density

$\mathbf{j}, \mathbf{j}^p$ primary current density vector

$\mathbf{j}^v$ volume current

$\mathbf{K}$ magnetic or electric lead field matrix

$\mathbf{T}$ minimum norm operator

$\mathbf{W}$ swLORETA operator

$\mathcal{N}_n(\mu, \mathbf{\Sigma})$ n dimensional Gaussian distribution of an n size random vector with mean vector μ and $n \times n$ covariance matrix

$\mathrm{diag}(\mathbf{A})$ produce a vector formed by the diagonal elements of the matrix $\mathbf{A}$

$\mathrm{Trace}(\mathbf{A})$ represent the trace of matrix $\mathbf{A}$

μ permeability

μ_0 permeability of free space

$\otimes$ Kronecker tensor product

ψ instantaneuos phase

ρ charge density

Σ_x	covariance matrix for the variable x
$\times$	cross product
A	instantaneuos amplitude
C	coherence index
n_g	number of grid points
n_s	number of sensors
S	Shannon entropy index

1

General Introduction

> I have been impressed with the urgency of doing. Knowing is not enough; we must apply. Being willing is not enough; we must do.
>
> Leonardo da Vinci

In 1875, the Liverpool physician, Dr. Richard Caton recorded for the first time electrical brain activity in vivisected rabbits and monkeys. Half a century later, in 1924, the German physiologist and psychiatrist Hans Berger became the first person to record such signals from the human brain. A whole new era was then open for the neurosciences as the electroencephalogram (EEG) gave the possibility to obtain objective information about brain functioning in a relatively easy, non expensive and, more importantly, non invasive way.

It is not fully understood yet how the EEG is produced. The most accepted hypothesis is that it reflects the summed activity of post-synaptic currents (Paul and Ramesh, 2006). Thus, an action potential in a pre-synaptic axon causes the release of a neurotransmitter into the synapse. This neurotransmitter diffuses across the synaptic cleft and bounds to the receptors of a post-synaptic dendrite. As a consequence, there is a flow of ions into or out of the dendrite, which in turn results in compensatory currents in the extra cellular space. It is believed that these extracellular currents are responsible for the scalp EEG voltages (Paul and Ramesh, 2006). It should be noted that the EEG does not give information about a single neuron. Rather, it gives information about several neurons which fire synchronously and have similar spatial orientation, radial to the scalp. Consequently, the EEG mostly registers the activity of apical dendrites in the cortex that have a parallel, radial arrangement.

The EEG is not the only imaging technique that assists neuroscientists in the the study of brain functions. As the neuronal electrical activity can be measured on the scalp, it is also possible to measure the magnetic field associated to it. This was done for the first time in 1968 by the Canadian born physics David Cohen. Since its introduction, the magnetoencephalogram (MEG) systems have experienced a fast growth. From the first equipments, which used only a few detectors, today there are dewars helmet-shaped which contain as many as ≈ 300 sensors that cover most of the head. Those sensors were initially

copper induction coils, today they are extremely sensitive superconducting quantum interference devices that can cope with both the weakness of the signal and the strength of the competing environmental noise.

Compared to other techniques such as positron emission tomography (PET) and functional magnetic image (fMRI) one of the main advantages of EEG and MEG as research and clinical tools is their temporal resolution, which is in the order of milliseconds. Unfortunately, they both have also a major drawback: their spatial resolution. In other words, it is impossible to know with certainty which brain area has generated the signal measured at the scalp. This is due to the fact that the cerebrospinal fluid, the skull and the scalp placed between the brain current sources and the sensors smear the current flow before it reaches the scalp. During the last years, many researchers have tried to overcome this limitation by developing methods that solve what has been called the biomagnetic inverse problem (Ebersole and Wade, 1990; Caplan et al., 2001). The main difficulty to overcome in order to develop such methods is determined by the physics nature of the problem: the measurements do not contain enough information about the generators as proven by Helmholtz in 1853 (Helmholtz, 1853). This limitation, termed the non-uniqueness of the inverse problem, prescribed the existence of an infinite number of "correct" answers.

In order to limit the amount of "correct" answers, it is necessary to introduce models that incorporate additional information or constrains about the anatomical and mathematical properties of the current inside the head. By using different "*priors*" information several aspects of the intracranial current can be modelled and thus different types of inverse solutions methods, i.e. dipolar methods, distributed etc.(Hämäläinen and Ilmoniemi, 1994) can be developed.

Despite the recent development of algorithms that have zero localization error under ideal conditions (Pascual-Marqui, 2002), there are still two main problems that seriously affect linear inverse solution algorithms: the tendency to underestimate deep generators in favor of cortical ones and the instability of the solution in the presence of noise. The reason for the first of these difficulties rests on the fact that electric and magnetic fields are inversely related to the square of the distance. Consequently, the fields generated by deep sources decay too fast and produce weak signals at sensor locations. The second difficulty is particularly important since EEG/MEG signal has a low SNR.

In this work, it is proposed a modification of the Standardized Low Resolution Electromagnetic Tomography (sLORETA) (Pascual-Marqui, 2002) named Standardized Weigthed Low Resolution Electromagnetic Tomography (swLORETA). It will be shown that compared to sLORETA, swLORETA has better tomography properties in the presence of noise and, at the same time, has less bias toward superficial sources. This suggests that EEG/MEG may contains the necessary information to estimate deep sources, which supports the claims of some authors in this field (Ioannides et al., 1995; Taylor et al., 1999).

Additionally, the new algorithm will be extended to characterize the EEG/MEG signal not only in terms of the anatomical localization of the sources within the brain but also in terms of its dynamic frequency content. As it has been shown that several brain rhythms can be associated to different normal and pathological states (Bhattacharya, 2001; Strelets et al., 2006; Whittington, 2008; D. Moretti, 2009) it is important to find the neural populations responsible of their generation to fully understand their nature.

This manuscript is organized as follows. In chapter (2) an introduction to the EEG/MEG is provided. In chapter (3) the newly developed swLORETA inverse solution method is introduced. In chapter (4) its formulation is extended to the time-frequency space. This will allow characterizing the EEG/MEG generators also in terms of their frequency dynamics. In chapter (5) the time-frequency extension will be used to characterize the large scale integration necessary for the emergency of a unified cognitive brain response. Conclusions and outlook are given in chapter (6). Two appendixes (A) and (B) give additional mathematical details about the Tikhonov regularization scheme and the Hilbert transform, respectively.

Some of the methods presented in this work have been published and are part of a software package named ASA (Advance Source Analysis `http://www.ant-neuro.com/products/asa`) widely used for the neuroscientists community.

2 *The Inverse Problem*

> The work of James Clerk Maxwell changed the world forever.
>
> Albert Einstein

2.1 Introduction

Neuroscientists are interested in explaining how the brain is able to orchestrate the cognitive life. In other words, how does it transforms an input signal, such as a visual stimulus, into a flow of concatenated, meaningful perceptions? One of the main aspects of such a quest is determining which brain areas generate the EEG/MEG signal recorded on the scalp in response to a given stimulus. In other words, it is important to find out the distribution of cerebral current sources that best explain the scalp measurements. Unfortunately, this is a difficult task and so it has been called the inverse problem. In the following paragraphs, the main difficulties that the inverse problem poses will be explained.

First of all, the inverse problem is ill posed because it does not have a unique solution: radically different source configurations may explain the data equally well. This is due to the existence of silent sources that cannot be measured on the scalp and to the principle of superposition, which states that when two or more sources are active simultaneously their measured field is the vector sum of each individual field. Additionally, the inverse problem is highly underdetermined because there is a limited amount of sensors/electrodes that can be placed on the scalp and numerically instable because of the presence of noise.

To limit the space of possible solutions, additional information or constrains about the physical and mathematical properties of the current inside the head have to be introduced. Dipolar methods, for example, handle the many-to-one nature of the problem by characterizing the sources in terms of a limited number of current dipoles that are fitted to the data using some measure of the reconstruction error. Although these methods have been widely used in epilepsy (Lantz et al., 1996; Ebersole and Wade, 1990), and somatosensory research (Hoechstetter et al., 2001; Baumgartner et al., 1998) there is a growing evidence that they may fail during complex cognitive tasks. In such situations, a wide

spread neural networks at the base of the EEG/MEG generation seems a more plausible hypothesis. For this reason, the distributed inverse methods will be the main focus of this thesis. These methods, as their general name indicates, assume the existence of a large number of dipolar EEG/MEG sources distributed over the entire brain. To estimate a unique solution they also introduce additional information about some aspect of the primary current density (PCD) using, for example, the Bayesian framework or equivalent via a regularization scheme (Tikhonov and Arsenin, 1997; Tarantola, 1987; Mackay, 1992).

The first step towards the solution of the inverse problem is to find a model that explain how the current flow is related to the electrical potential on the scalp or the magnetic field measured above the head. This task is often referred as the bioelectromagnetic forward problem. This chapter will be dedicated to review the forward problem and will provide the mathematical framework for the solution of the inverse problem.

2.2 Quasistatic Approximation of Maxwell's Equations

The Maxwell's equations and the continuity equation ($\nabla \cdot \mathbf{J} = -\partial\rho/\partial t$ $\mathbf{J}$ and ρ are the total current density and the charge density, respectively) can be used to calculate the electric field $\mathbf{E}$ and the magnetic induction $\mathbf{B}$ for a bioelectromagnetic signal, e.g. an electric generator in the brain, if the conductivity ρ and the source generators are known. Usually, for applications in biomagnetism, Maxwell's equations are considerably simplified by doing two approximations.

The first approximation concerns the magnetic permeability μ of the different tissues in the head, which is approximately set to the permeability of free space, i.e, $\mu = \mu_0 = 4\pi \times 10^7\,\mathrm{H/m}$. Thereby, Maxwell's equations take the form:

$$\nabla \cdot \mathbf{D} = \rho \tag{2.1}$$

$$\nabla \times \mathbf{E} = -\frac{\partial \mathbf{B}}{\partial t} \tag{2.2}$$

$$\nabla \cdot \mathbf{B} = 0 \tag{2.3}$$

$$\nabla \times \mathbf{H} = \mathbf{J} + \frac{\partial \mathbf{D}}{\partial t}. \tag{2.4}$$

If the material are consider to be linear and isotropic, $\mathbf{D}$ and $\mathbf{B}$ are defined by:

$$\mathbf{B} = \mu\mathbf{H} \tag{2.5}$$

$$\mathbf{D} = \epsilon\mathbf{E} \tag{2.6}$$

where ϵ is the permittivity of the medium.

In a passive non-magnetic medium, the current density vector $\mathbf{J}$ consists of an ohmic volume current $\mathbf{j}^v = \sigma\mathbf{E}$ and a primary current $\mathbf{j}^p$ (see subsection 2.3). By substituting equation (2.5) and (2.6) into (2.4) it is obtained:

$$\nabla \times \mathbf{B} = \mu_0 \left(\mathbf{j}^p + \sigma \mathbf{E} + \epsilon \frac{\partial \mathbf{E}}{\partial t} \right). \tag{2.7}$$

If the bioelectromagnetic phenomena is considered at frequency w (typically in the $< 1000\,\mathrm{Hz}$ range), the electrical field can be written as:

$$\mathbf{E} = \mathbf{E}_0 \exp(iwt),$$

and equation (2.7) can be restated as:

$$\nabla \times \mathbf{B} = \mu_0 \left(\mathbf{j}^p + \sigma \mathbf{E}_0 \exp(iwt) + i\epsilon w \mathbf{E}_0 \exp(iwt) \right). \tag{2.8}$$

The second approximation, the so called quasistatic approximation, implies that the $\partial \mathbf{E}/\partial t$ and $\partial \mathbf{B}/\partial t$ are ignored as source terms and only static fields for $\mathbf{E}$ and $\mathbf{B}$ are considered. Note that the time derivate term in equation (2.7) should be smaller than the ohmic current for this approximation to be valid: $\epsilon |\partial \mathbf{E}/\partial t| \ll |\sigma \mathbf{E}$. Equation (2.8) shows that this is the case provided $\epsilon w \ll \sigma$. Using an average conductivity of $\sigma = 0.3\,\Omega^{-1}\mathrm{m}^{-1}$ for brain tissue, $\epsilon = 10^5 \epsilon_0$ and a frequency of $w = 2\pi f = 200\pi \mathrm{s}^{-1}$ then $\epsilon w/\sigma \approx 1.8 \times 10^{-3} \ll 1$.

In addition, it is possible to demonstrate that the contribution of $\partial \mathbf{B}/\partial t$ to $\mathbf{E}$ in equation (2.2) is small too. From equation (2.8) and considering that $\nabla \times (\nabla \times \mathbf{E}) = -\partial/\partial t (\nabla \times \mathbf{B})$ it is obtained,

$$\nabla \times (\nabla \times \mathbf{E}) = -iw\mu_0 \left(\sigma + iw\epsilon \right) \mathbf{E}. \tag{2.9}$$

Solutions to this equation have spatial changes on the characteristic length scale (Hämäläinen et al., 1993):

$$\lambda_c = |w\mu_0 \sigma (1 + iw\epsilon/\sigma)|^{-1/2}. \tag{2.10}$$

With the parameters given above it is obtained $\lambda_c = 65\,\mathrm{m}$, which is much larger than the diameter of the head. This implies that the contribution of $\partial \mathbf{B}/\partial t$ to $\mathbf{E}$ is small.

In summary, the field do vary in time, but the time dependence adds no distinct source term to the right side of equation (2.2) and (2.4). Therefore, we can simplify Maxwell's equation into the quasistatic form:

$$\nabla \cdot \mathbf{D} = \rho \tag{2.11}$$

$$\nabla \times \mathbf{E} = 0 \tag{2.12}$$

$$\nabla \cdot \mathbf{B} = 0 \tag{2.13}$$

$$\nabla \times \mathbf{H} = \mathbf{J} \tag{2.14}$$

Since $\nabla \times \mathbf{E} = 0$, the electric field can be expressed with a scalar potential $\mathbf{E} = -\nabla V$, with V being the electric potential.

2.3 Primary and Secondary Current

In the study of the bioelectromagnetic fields, the current density $\mathbf{J}(\mathbf{r})$ at each position $\mathbf{r}$ is usually split into two contributions: the intracellular current flow and its accompanying extracellular current (Hämäläinen et al., 1993; Paul and Ramesh, 2006). This intracellular current flow is the result of the macroscopic electric field that acts on the charges carriers in the surrounding tissues giving the so-called volume current $\mathbf{j}^v$. All other contributions to the current density $\mathbf{J}$ are referred to as the primary current $\mathbf{j}^p$. Since they represent the active origin of the neuromagnetic field as the primary source, the volume or return current is passive. If the cellular level details are neglected and the whole head is regarded as a homogeneous conductor, then the current density can be written as:

$$\mathbf{J}(\mathbf{r}) = \mathbf{j}^p(\mathbf{r}) + \sigma(\mathbf{r})\mathbf{E}(\mathbf{r}) = \mathbf{j}^p(\mathbf{r}) + \sigma(\mathbf{r})\nabla V(\mathbf{r}) \tag{2.15}$$

Splitting the current density in this way, illustrates the fact that the neural activity gives rise to primary current mainly in a given cell or its close surroundings whereas the volume current flows passively everywhere in the medium. By finding the primary current(s), the active brain sources can be located.

2.4 Forward Problem

Bioelectromagnetic fields are caused by electric currents in conducting body tissues (e.g the brain, the heart or muscles). The computation of the magnetic field given the electric sources details (i.e., magnitude and position relative to the detector) is often referred to as the bioelectromagnetic forward problem. Using the above equations, the expression for calculating electrical potential V and the magnetic induction $\mathbf{B}$ at a point $\mathbf{r}$ due to a current density $\mathbf{J}$ existing at $\mathbf{r}'$ can be derived. Such equations are referred to as the Bio-Savart law or the continuous counterpart of the Ampére-Laplace law (Landau and Lifshitz, 1962)and they provide solutions for the bioelectromagnetic forward problem,

$$\mathbf{B}(\mathbf{r}) = \frac{\mu_0}{4\pi}\int \frac{\mathbf{J}(\mathbf{r}')\times\mathbf{R}}{R^3}\mathrm{d}^3\mathbf{r}' \tag{2.16}$$

$$V(\mathbf{r}) = \frac{1}{4\pi\sigma}\int \frac{\mathbf{J}(\mathbf{r}')\cdot\mathbf{R}}{R^3}\mathrm{d}^3\mathbf{r}' \tag{2.17}$$

where $\mathbf{R} = \mathbf{r} - \mathbf{r}'$ and $R = \|\mathbf{r} - \mathbf{r}'\|$.

Equation (2.16) and (2.17) are derived from Maxwell's equation (2.13) and (2.14) under the quasistatic approximation. With a few simplifications (Hämäläinen et al., 1993) and under the assumption that the current density at $\mathbf{r}'$ approaches zero sufficiently fast when $\mathbf{r}'$ goes to infinity, it can be obtained:

$$\mathbf{B}(\mathbf{r}) = \frac{\mu_0}{4\pi}\int \frac{\nabla'\times\mathbf{J}(\mathbf{r}')}{R^3}\mathrm{d}^3\mathbf{r}' \tag{2.18}$$

With (2.15) and the identity $\nabla\times(\sigma\nabla\cdot V) = \nabla\sigma\times\nabla V$ inserted in equation (2.18) then:

$$\mathbf{B}(\mathbf{r}) = \frac{\mu_0}{4\pi}\left(\int \frac{\nabla' \times \mathbf{j}^p(\mathbf{r}')}{R^3}\mathrm{d}^3\mathbf{r}' - \int \frac{\nabla'\sigma \times \nabla' V}{R^3}\mathrm{d}^3\mathbf{r}'\right) \tag{2.19}$$

While the first term of equation (2.19) is the direct contribution of $\mathbf{j}^p$, the second term is due to $\mathbf{j}^v$. Note that there is no contribution from the second term, in the case of an infinite homogeneous conductor $(\nabla'\sigma = 0)$. With the identity $\nabla\sigma \times \nabla V = -\nabla \times (V\nabla \cdot \sigma)$ and a comparison of equations (2.16), (2.18) and (2.19) it is obtained:

$$\mathbf{B}(\mathbf{r}) = \frac{\mu_0}{4\pi}\int \left(\mathbf{j}^p + V\nabla' \cdot \sigma\right) \times \frac{\mathbf{R}}{R^3}\mathrm{d}^3\mathbf{r}' \tag{2.20}$$

Because the source of the magnetic field is the total current density $\mathbf{J}$, both $\mathbf{j}^p$ and $\sigma\mathbf{E}$ contribute to $\mathbf{B}$. However, in equation (2.19) $\sigma\mathbf{E}$ is replaced by an equivalent fictitious current $V\nabla \cdot \sigma$ which in general has no direct physical meaning (Hämäläinen et al., 1993). By taking the divergence of (2.14) and (2.15) it is obtained:

$$\nabla \cdot (\sigma\nabla \cdot V) = \nabla \cdot \mathbf{j}^p \tag{2.21}$$

Under the appropriate constraints, a solution for V is possible (Hämäläinen et al., 1993). If V is known, then $\mathbf{B}$ can be calculated directly from equation (2.20).

2.5 Piecewise Homogeneous

If the conducting medium is considered as a piecewise homogeneous conductor, then $\nabla\sigma$ is non-zero only at the boundaries and it is possible to expand the second term in equation (2.20) as a sum of surface integrals over the boundaries of all the discontinuities of σ (Geselowitz, 1970; Hämäläinen et al., 1993).

$$\mathbf{B}^v(\mathbf{r}) = -\frac{\mu_0}{4\pi}\sum_{j=1}^{n}\left(\sigma_j^{out} - \sigma_j^{in}\right)\int \frac{V(\mathbf{r}')\,\hat{\mathbf{n}}_j \cdot \mathbf{R}}{R^3}\mathrm{d}S_j' \tag{2.22}$$

where σ_j^{in} and σ_j^{out} are the conductivities inside and outside the conducting object of the surface S_j, $\hat{\mathbf{n}}$ is an outward unit vector normal to the surface S_j , and $\mathrm{d}S_j$ a surface element. Analogous to equation (2.22), the electrical potential V^v is given by (Geselowitz, 1967):

$$V^v(\mathbf{r}) = -\frac{1}{4\pi\sigma}\sum_{j=1}^{n}\left(\sigma_j^{out} - \sigma_j^{in}\right)\int \frac{V(\mathbf{r}')\,\hat{\mathbf{n}}_j \cdot \mathbf{R}}{R^3}\mathrm{d}S_j' \tag{2.23}$$

where σ denotes the electrical conductivity of the medium surrounding $\mathbf{r}$.

In the calculation of the magnetic field described in equation (2.22), the volume currents can be replaced by an equivalent surface current distribution $(\sigma_j^{in} - \sigma_j^{out})V(\mathbf{r}')\hat{\mathbf{n}}_j(\mathbf{r}')$ on the boundaries of S_j and are often termed as "*secondary currents*". The above expressions show how secondary sources contribute to the magnetic field and to the electrical potential. The fact that the direction of secondary currents is perpendicular to the boundary between media of different conductivities, explains why the

contribution to the field is only tangential to the underlaying surface and hence the radial component of the magnetic field is not affected by secondary currents. Given a spherically symmetric conductor, the corresponding secondary sources are distributed across the spherical surface with the current pointing everywhere in the radial direction. The field is consequently everywhere tangential to the sphere and hence measurements to the component of the fields that are normal to the surface provide information about the primary source alone (Hämäläinen et al., 1993).

2.6 The Equivalent Current Dipole Model

The Equivalent Current Dipole Model (ECD) can be used as a simple model to describe the relationship between neural activity and the generated electrical and magnetic field. It is used to approximate the flow of electrical current in a small area of interest. For a single current dipole $\mathbf{Q}$, the map of the radial magnetic field B_r has one maximum and one minimum. The dipole, which lies halfway between the extrema, can be thought of as a short current element I, with the length l and negligible cross-section. This vector is fully characterized by its position and orientation in space. The dipole moment $\mathbf{Q}$, is defined as $\mathbf{Q} = I \cdot l$, with the units Am. A typical strength of a dipole, caused by synchronous activity of probably tens of thousands of neurons, is $10\,\mathrm{nAm}$. If current dipole model is used to describe the electrical properties of biological sources, then it has to be taken into account that the description is only adequate when a small region of active tissue, i.e. where the largest linear dimension of the region is much smaller than its distance to the measuring point, is considered.

In the previous section, it was shown that the magnetic induction $\mathbf{B}$ and the electrical potential V are given by equations (2.16) and (2.17).

Considering a more general case with a distribution of primary current density (PCD) $\mathbf{j}^p$ over a certain brain volume, a current dipole can be thought of as a concentration of $\mathbf{j}^p(\mathbf{r})$ to a single point $\mathbf{r}_Q$:

$$\mathbf{j}^p(\mathbf{r}) = \mathbf{Q}\delta(\mathbf{r} - \mathbf{r}_Q) \tag{2.24}$$

where $\delta(\mathbf{r} - \mathbf{r}_Q)$ is the Dirac delta function.

The integral of the time-delayed Dirac's delta function is given by:

$$\int_{-\infty}^{+\infty} f(\mathbf{x})\delta(\mathbf{x} - \mathbf{x}_0)\mathrm{d}\mathbf{x} = f(\mathbf{x}_0) \tag{2.25}$$

By using equations (2.24) and (2.16) the resulting magnetic field $\mathbf{B}$ for the primary current density generated by a dipolar source is given by the well-known Biot-Savart law:

$$\mathbf{B}(\mathbf{r}) = \frac{\mu_0}{4\pi}\frac{\mathbf{Q}(\mathbf{r}_Q) \times \mathbf{R}_Q}{R_Q^3} \tag{2.26}$$

where $\mathbf{R}_Q = \mathbf{r} - \mathbf{r}_Q$ and $R_Q = \|\mathbf{r} - \mathbf{r}_Q\|$. Vectors $\mathbf{r}_Q$ and $\mathbf{r}$ represent the position where the current dipole $\mathbf{Q}$ is located and the point where the magnetic field is evaluated, respectively. A similar relation can be found for the electrical potential V using equation (2.17).

Since a point like source is magnetically silent (no magnetic signals is produced) it is sometimes convenient to consider $\mathbf{Q}$ as an infinitesimal line element (ILE) of current I pumped from a sink at $\mathbf{r}_1$ to a source $\mathbf{r}_2$ with a very small source-sink separation.

A single post-synaptic activity at a dendrite of a pyramidal cell has typically a dipole strength of about $\mathbf{Q} \approx 3 \times 10^{-13}\,\mathrm{Am}$ (Williamson and Kaufmann, 1990). Thus, for a single pyramidal cell, which may be $4\,\mathrm{cm}$ from a detector and using equation (2.24), the above dipole strength will produce such a weak magnetic field ($\approx\ 2 \times 10^{-17}\,\mathrm{T}$) that it is not detectable outside the head. But since there are approximately 10^5 pyramidal cells per mm^2 of cortex with hundreds or thousands of synapses per neuron, the resulting magnetic field can be detected. Assuming that n current dipoles are operating simultaneously and pointing in the same direction the magnetic field $\mathbf{B}$ can be expressed by the vector sum of all single fields:

$$\mathbf{B} = \mathbf{B}_1 + \mathbf{B}_2 + \cdots + \mathbf{B}_n \tag{2.27}$$

A magnetic field of $100\,\mathrm{fT}$, which is about the order of a typical response to a stimulation, requires more than 5000 neurons simultaneously active. If the locations of the active current dipoles are close together, say within a few cubic millimeters, it can be considered that the magnetic field (or strictly speaking, the magnetic induction) $\mathbf{B}$ is generated by only one equivalent current dipole. However, it has to be taken into account that the bigger the area is, the less accurate is the description of the biological activity provided by the ECD model (Hämäläinen et al., 1993; Hämäläinen and Ilmoniemi, 1994). Nevertheless, as long as the activity is generated within one or two well-separated small regions the ECD model is satisfactory.

In summary, the equivalent current dipole model considered as an ILE is widely used as the simplest model to describe the unidirectional primary current density in a few cubic centimeters of an active brain.

2.7 Lead Fields

In previous sections it has been shown that there is a linear relation between B related to the PCD. Thus, for each detector i the output of a magnetometer $\mathbf{B}_i$ can be expressed as a linear function of the form:

$$\mathbf{B}_i = \int_Q \mathbf{k}_i(\mathbf{r}) \cdot \mathbf{j}^p(\mathbf{r}) \mathrm{d}^3\mathbf{r}. \tag{2.28}$$

with the vector field $\mathbf{k}_i(\mathbf{r})$ playing the role of the kernel. This vector field ($\mathbf{k}_i(\mathbf{r})$) describes the sensitivity distribution of each sensor and depends on the conductivity σ and on the coil configuration of the magnetometer or gradiometer system (Sarvas, 1987; Hämäläinen et al., 1993; Hämäläinen and Ilmoniemi, 1994). The integral in equation (2.28) extends over a finite volume Q (often called the source space) where the current distribution is believed to lie.

By analogy with equation (2.28), the lead field $\mathbf{k}_i^E$ of an electric measurement V_i is given by:

$$V_i = \int_Q \mathbf{k}_i^E(\mathbf{r}) \cdot \mathbf{j}^p(\mathbf{r}) \mathrm{d}^3\mathbf{r}. \tag{2.29}$$

with V_i being the potential difference between the ith electrode and a reference electrode.

Assuming the ECD model for the PCD, the magnetic field can be obtained by substituting equation (2.24) in (2.28) as:

$$\mathbf{B}_i = \mathbf{k}_i(\mathbf{r}_Q) \cdot \mathbf{Q}.$$

Using this equation the three components of the lead field matrix $\mathbf{k}_i(\mathbf{r}_Q)$ can be found for any dipole position $\mathbf{r}_Q$ as long as the magnetic field $\mathbf{B}_i$ is provided. Furthermore if the PCD is modelled as a superposition of n_g simultaneous ECD then the magnetic field takes the form:

$$\mathbf{B}_i = \sum_{j=1}^{n_g} \mathbf{k}_i(\mathbf{r}_j) \cdot \mathbf{Q}_i. \tag{2.30}$$

Using equation (2.30) we can define ns simultaneous equations for the n_s sensors output as:

$$\mathbf{B} = \mathbf{KQ} \tag{2.31}$$

where $\mathbf{K}$ is an $n_s \times 3n_g$ matrix with the element $\mathbf{k}_{ij}$ as the lead field vector for the ith sensor due to the jth dipole,

$$\mathbf{K} = \begin{pmatrix} \mathbf{k}_{1,1} & \mathbf{k}_{1,2} & \cdots & \mathbf{k}_{1,n_g} \\ \mathbf{k}_{2,1} & \mathbf{k}_{2,2} & \cdots & \mathbf{k}_{2,n_g} \\ \cdots & \cdots & \cdots & \cdots \\ \mathbf{k}_{n_s,1} & \mathbf{k}_{n_s,2} & \cdots & \mathbf{k}_{ns,n_g} \end{pmatrix}$$

Vector $\mathbf{Q}$ is ordered in blocks so that all three spatial components of a specific dipole appear directly one after the other in the form:

$$\mathbf{Q}^p = \left(\ldots, \mathbf{Q}_k^{p,x}, \mathbf{Q}_k^{p,y}, \mathbf{Q}_k^{p,z}, \ldots\right)^T,$$

T represents vector transpose. $\mathbf{B}$ is an n_s dimension vector built from the $\mathbf{B}_i$ in each sensors in the same way as $\mathbf{Q}$.

If the source space is further discretized into a grid with n_g volume elements, the average primary current density $\mathbf{j}^p$ in voxel V_k is intertwined with the current dipole in this voxel by:

$$\mathbf{Q}_k = \mathbf{j}_k^p \Delta V_k.$$

Given this relation and considering equation (2.31), a relation between the PCD and the magnetic field can be obtained as :

$$\mathbf{B} = \mathbf{K}\mathbf{j}^{p}. \tag{2.32}$$

An expression equivalent to (2.32) can be found for the electrical case. In this case, the vector that represents the potential difference between the ith electrode and a reference electrode plays the role of $\mathbf{B}_i$ while $\mathbf{K}^E$ plays the role of $\mathbf{K}$. Since the form of equation (2.32) is the same for both the magnetic and electric cases in the next chapters they will not be explicitly differentiated. Thus $\mathbf{K}$ and $\mathbf{d}$ will be used to refer to the lead field matrix and the EEG/MEG signal vector, respectively. In the same way, the superscript p in the notation of the PCD will be drooped. With this notation changes equation (2.32) can be rewritten as:

$$\mathbf{d} = \mathbf{K}\mathbf{j} + \mathbf{n} \tag{2.33}$$

where $\mathbf{n}$ is n_s dimensional vector that represents the additive instrumental noise that affects the signal recorded in the sensors.

Using the above formulation, the following lead field characteristics can be illustrated:

1. they are vector quantities that reflects the sensitivity profile of each sensor;
2. they are affected by the relative location of the source space and the detection coil;
3. they are influenced by the conductivity profile and, hence, different conductor models will correspond to different lead field patterns. It is worth noting that the expansion functions automatically exclude any contribution from magnetically silent sources;
4. since the expansion functions $\mathbf{k}_i(\mathbf{r})$ are completely determined by the geometric details of the sensors for a given source type, the lead field only need to be calculated once for each sensor arrangement.

3

Formulation of swLORETA in the time domain

> Our mind is capable of passing beyond the dividing line we have drawn for it. Beyond the pairs of opposites of which the world consists, other, new insights begin.
>
> Hermann Hesse

3.1 Introduction

As explained in section (1) several methods have been developed in order to determine the neural generators of the EEG/MEG signal recorded on the scalp. One of these methods, sLORETA, was introduced by Pascual Marqui in 2002. Due to its accurate tomographic properties, e.g. zero-localization error for single dipoles in noiseless simulated data (Pascual-Marqui, 2002; Wagner et al., 2004), it has rapidly grown in popularity among EEG/MEG researchers. However, it also has some limitations: its spatial resolution is limited in the presence of noise and when two dipoles are active simultaneously (Pascual-Marqui, 2002; Wagner et al., 2004).

In order to overcome those limitations, it is presented here a new algorithm named Standardized Weighted Low Resolution Tomography (swLORETA). In contrast to sLORETA, swLORETA incorporates a singular value decomposition (SVD) based lead field weighting to compensate the tendency of the linear inverse procedures in general, and sLORETA in particular, to reconstruct the sources close to the location of the sensors. The sensitivity of the solution to the presence of noise is also decreased. As a consequence, swLORETA is superior to sLORETA particularly under noisy conditions and for the reconstruction of deep sources.

The first part of this chapter will be devoted to the mathematical foundations of the Minimum Norm (MN) method (section (3.2)), the basis of sLORETA and swLORETA. Then, sLORETA will be presented in section (3.3). Finally swLORETA will be developed (section (3.4)) and its tomographic properties will be demonstrated using simulated (section (3.5)) and experimental data (section (3.6)).

3.2 The Minimum-Norm Inverse Solution

MN, as well as all distributed source localization methods, solve equation (3.23) assuming that there is a large number of dipolar sources distributed over the brain ($n_g \gg n_s$). Different procedures have been proposed to place these dipolar sources inside the brain depending on the anatomical information available. Usually, this dipolar sources are positioned to form a 3D grid of points inside the head. Furthermore, if an MRI images is at hand, this grid is placed in coregistration with it. Additional information can be used to further restrict the space of possible solutions by assuming that the EEG/MEG signal can only be generated within the gray matter. Thus, only the points that belong to it are used as part of the source space. Other authors also assume that the EEG/MEG sources are perpendicular to the cortex surface that is represented by the white/gray matter interface(Dale and Sereno, 1993). This last constrain will not be considered here.

Due to the assumption about the amount of possible generators introduced by the MN method, the lead field matrix $\mathbf{K}$ rank is less than $3n_g$, therefore equation (2.32) has an infinite number of solutions (the ill-posedness property of the bioelectromagnetic inverse problem (Helmholtz, 1853)). Consequently, to compute a unique solution additional knowledge about the current sources inside the head, besides the anatomical constraints already explained, have to be introduced. In this thesis, the Bayesian framework to incorporate such priors information and the MAP (maximum *à posteriori*) principle to select the "best estimate" for the PCD $\mathbf{j}$ will be used.

A Bayesian model is defined by its functional form, which is given by equation (2.32), and by two probability distributions: a prior distribution $p(\mathbf{j} \mid \beta)$ that summarizes our initial state of knowledge about the mathematical and anatomical properties for $\mathbf{j}$ and the likelihood $p(\mathbf{d} \mid \mathbf{j}, \lambda)$, which states the prediction the theoretical model makes about the data $\mathbf{d}$ when the parameter vector has a particular value $\mathbf{j}$ (Tan and Fox, 2001; Mackay, 1992). An expression for the posterior distribution can then be found using the Bayes rule (Mackay, 1992; Tan and Fox, 2001):

$$p(\mathbf{j} \mid \mathbf{d}, \lambda, \beta) = \frac{p(\mathbf{d} \mid \mathbf{j}, \lambda)\, p(\mathbf{j} \mid \beta)}{p(\mathbf{d} \mid \lambda, \beta)} \tag{3.1}$$

where λ and β are named hyperparameters and express the degree of uncertainty about the priors assumptions and the predictions, respectively; both parameter are supposedly known. $p(\mathbf{d} \mid \lambda, \beta)$ is a normalization constant called the evidence for λ and β that is ignored because it is irrelevant for the inference of $\mathbf{j}$.

The likelihood $p(\mathbf{d} \mid \mathbf{j}, \lambda)$ is defined by making assumptions about the statistical properties of the experimental noise $\mathbf{n}$ in equation (2.32). A typical assumption is that the sensor noise can be expressed in term of a multivariate Gaussian distribution with zero mean and covariance matrix:

$$\mathbf{\Sigma}_{\mathbf{d},noise} = (1/\lambda)\, \mathbf{I}_{ns} \tag{3.2}$$

where $\mathbf{I}_{ns}$ is the identity matrix of size ns, $1/\sqrt{\lambda}$ is the standard deviation of the noise. Therefore, the likelihood function can be written as:

$$p(\mathbf{d}\,|\,\mathbf{j},\lambda) = p(\mathbf{n} = \mathbf{d} - \mathbf{K}\mathbf{j}\,|\,\lambda) = \mathcal{N}_{ns}(\mathbf{K}\mathbf{j}, \mathbf{\Sigma}_{\mathbf{d},noise}), \tag{3.3}$$

where $\mathcal{N}_n(\mu, \mathbf{\Sigma})$ is the n dimensional Gaussian distribution of an n size random vector $\mathbf{x}$, mean vector μ and $n \times n$ covariance matrix $\mathbf{\Sigma}$,

$$\mathcal{N}_n(\mu, \mathbf{\Sigma}) = \frac{1}{(2\pi)^{n/2}\,|\mathbf{\Sigma}|^{1/2}} \exp\left(-\frac{1}{2}(\mathbf{x}-\mu)^T\mathbf{\Sigma}^{-1}(\mathbf{x}-\mu)\right). \tag{3.4}$$

On the other hand, assuming that the PCD follows a Gaussian distribution with zero mean and covariance matrix:

$$\mathbf{\Sigma}_{\mathbf{j}} = (1/\beta)\,\mathbf{I}_{3n_g} \tag{3.5}$$

where $\mathbf{I}_{3n_g}$ is the identity matrix of size $3n_g \times 3n_g$ denotes the choice of the mathematical and anatomical constrains and T denotes matrix transpose. Under this ansatz the prior distribution can be expressed as:

$$p(\mathbf{j}\,|\,\beta) = \mathcal{N}_{3n_g}(\mathbf{0}, \mathbf{\Sigma}_{\mathbf{j}}) \tag{3.6}$$

Substituting equations (3.3) and (3.6) in equation (3.1) the posterior probability is given by:

$$p(\mathbf{j}\,|\,\mathbf{d},\lambda,\beta) \propto \exp\left(-\frac{1}{2}\left\{\lambda\,(\mathbf{d}-\mathbf{K}\mathbf{j})^T(\mathbf{d}-\mathbf{K}\mathbf{j}) + \beta\,\mathbf{j}^T\mathbf{j}\right\}\right) \tag{3.7}$$

$$\propto \exp\left(-\frac{1}{2}\left\{\lambda\,\|\mathbf{d}-\mathbf{K}\mathbf{j}\|^2 + \beta\,\|\mathbf{j}\|^2\right\}\right), \tag{3.8}$$

where $\|\mathbf{x}\|^2$ represents the square of the Frobenius' 2-norm given by $\|\mathbf{x}\|^2 = \mathrm{Trace}(\mathbf{x}^T\mathbf{x})$.

To find the "best linear unbiased estimate" the posterior probability given by equation (3.8) with respect to $\mathbf{j}$ has to be maximized. This is is equivalent to minimize the function:

$$F(\mathbf{d};\mathbf{j}) = -2\log\left(p\left(\mathbf{j}\,|\,\mathbf{d},\lambda,\beta\right)\right) \tag{3.9}$$

$$= \lambda\,(\mathbf{d}-\mathbf{K}\mathbf{j})^T(\mathbf{d}-\mathbf{K}\mathbf{j}) + \beta\,\mathbf{j}^T\mathbf{j} + const \tag{3.10}$$

The problem of finding $\mathbf{j}$ can then be formally written as

$$\hat{\mathbf{j}} = \arg\min_{\mathbf{j}}\left\{F(\mathbf{d};\mathbf{j})\right\} \tag{3.11}$$

$$= \arg\min_{\mathbf{j}}\left\{\lambda\,\|\mathbf{d}-\mathbf{K}\mathbf{j}\|^2 + \beta\,\|\mathbf{j}\|^2 + const\right\} \tag{3.12}$$

This problem is equivalent to the *Tikhonov regularization* technique according to the general scheme of balancing between trust in the data and fidelity to priors (Tikhonov and Arsenin, 1997; Tarantola, 1987).

A formal solution to this problem for given values of λ, β, $\mathbf{K}$ and $\mathbf{d}$ may readily be found by setting:

$$\frac{\partial}{\partial \mathbf{j}_k}\left\{\lambda\,(\mathbf{d}-\mathbf{K}\mathbf{j})^T(\mathbf{d}-\mathbf{K}\mathbf{j})+\beta\,\mathbf{j}^T\mathbf{j}\right\}=0 \tag{3.13}$$

where $\mathbf{j}_k$ is the kth component of $\mathbf{j}$ and $k=1,2,\ldots,3ng$. This leads to the following equation for the estimator of $\mathbf{j}$ (see Appendix (A)):

$$\hat{\mathbf{j}}(\alpha)=\left(\mathbf{K}^T\mathbf{K}+\alpha\mathbf{I}_{n_s}\right)^{-1}\mathbf{K}^T\mathbf{d} \tag{3.14}$$

or equivalently (see Appendix (A)),

$$\hat{\mathbf{j}}(\alpha)=\mathbf{K}^T(\mathbf{K}\mathbf{K}^T+\alpha\mathbf{I}_{n_s})^{-1}\mathbf{d}=:\mathbf{T}(\alpha)\mathbf{d} \tag{3.15}$$

where $\mathbf{I}_{n_s}$ is the identity matrix of dimension $n_s\times n_s$ and α is a non-negative number called the regularization parameter which is defined as $\alpha=\beta/\lambda$.

3.2.1 Generalized Cross Validations

In the previous section the equation (3.15), which provides a linear mapping between the data vector $\mathbf{d}$ and the PCD $\mathbf{j}$ given the lead field matrix $\mathbf{K}$, was derived. In order for this map to be completely defined the value of the regularization parameter α, which is assumed to be known, has to be provided. Several methods have been proposed in order to obtain this parameter, i.e "L-curve" (Tan and Fox, 2001). Here the generalized cross-validation (GCV) method (Golub et al., 1979) will be used. The GCV estimate of α is the minimizer of the generalized cross-validation error $GCVE(\alpha)$ given by:

$$GCVE(\alpha)=\frac{1}{n_s}\sum_{i=1}^{n_s}\left(\mathbf{d}_i-\left(\mathbf{K}\mathbf{j}_{[i]}\right)_i\right)^2 w_k(\alpha) \tag{3.16}$$

where $\left(\mathbf{K}\mathbf{j}_{[i]}\right)_i$ is the ith component of vector $\mathbf{K}\mathbf{j}_{[i]}$ and $\mathbf{j}_{[i]}$ is the PCD obtained with the ith data point omitted given by:

$$\mathbf{j}_{[i]}=\mathbf{K}_{[i]}^T\left(\mathbf{K}_{[i]}\mathbf{K}_{[i]}^T+\alpha\mathbf{I}_{ns}\right)^{-1}\mathbf{d}_{[i]},$$

with $\mathbf{K}_{[i]}$ and $\mathbf{d}_{[i]}$ obtained from matrix $\mathbf{K}$ and vector $\mathbf{d}$ obtained by removing its ith row and ith component, respectively. $w(\alpha)$ is given by:

$$w_k(\alpha)=\frac{1-\mathbf{A}_{kk}(\alpha)}{1-\frac{1}{n}\mathrm{Trace}(\mathbf{A}(\alpha))}$$

where $\mathbf{A}(\alpha)=\mathbf{K}\left(\mathbf{K}^T\mathbf{K}+\alpha\mathbf{I}_{3n_g}\right)^{-1}\mathbf{K}^T$.

In a nutshell, the generalized cross-validation error defined in equation (3.16) measures the weighting mean squared difference between the actual output of the ith detector and its predicted output. Such predicted output is obtained from a PCD that have been calculated after removing the contribution of the

detector under analysis. The resulting value of α after generalized cross-validation is given by taking the derivative of $GCVE(\alpha)$ with respect to α and setting it to zero.

3.3 Standardized Low Resolution Electromagnetic Tomography

The sLORETA method computes a statistical map by performing a location-wise inverse weighting of the MN inverse solution results with their estimated variances. By applying this normalization statistical parametric maps (SPMs) are obtained. Those maps provide information about the statistical reliability of the estimated PCD distribution at each brain point over time with millisecond accuracy.

Mathematically, the starting point of sLORETA is the PCD distribution obtained by equation (3.15). The task now is to compute the standard deviation of the PCD to perform the aforementioned normalization. Taking into account the linear relation in equation (2.32) and the independence between the noise and the PCD, the covariance of the magnetic flux $\mathbf{\Sigma_d}$ can be written as (for details see Mardia et al., 1979):

$$\mathbf{\Sigma_d} = \mathbf{K}\mathbf{\Sigma_j}\mathbf{K}^T + \mathbf{\Sigma}_{\mathbf{d},noise} \tag{3.17}$$

which under the assumptions given by equations (3.2) and (3.5) takes the form:

$$\mathbf{\Sigma_d} = \mathbf{K}\mathbf{K}^T + \alpha\mathbf{I}_{ns} \tag{3.18}$$

From equation (3.18) and making use of the linear relation in equation (3.15), the covariance of the estimates PCD is given by:

$$\mathbf{\Sigma}_{\hat{\mathbf{j}}} = \mathbf{T}(\alpha)\mathbf{\Sigma_d}\mathbf{T}(\alpha)^T = \mathbf{K}^T(\mathbf{K}\mathbf{K}^T + \alpha\mathbf{I}_{ns})^{-1}\mathbf{K} \tag{3.19}$$

Finally, the sLORETA solution (Pascual-Marqui, 2002) is obtained from equations (3.19) and (3.15) in the following way:

$$\hat{\mathbf{j}}_{sLORETA,l} = \left\{\left[\mathbf{\Sigma}_{\hat{\mathbf{j}}}\right]_{ll}\right\}^{-1/2}\hat{\mathbf{j}}_l = \left\{\left[\mathbf{\Sigma}_{\hat{\mathbf{j}}}\right]_{ll}\right\}^{-1/2}\mathbf{T}_l\mathbf{d} \tag{3.20}$$

where $\hat{\mathbf{j}}_{sLORETA,l}$ is a 3-dimensional vector corresponding to the PCD at voxel l, $\left[\mathbf{\Sigma}_{\hat{\mathbf{j}}}\right]_{ll}$ is a 3×3 matrix given by the lth diagonal block of the matrix in equation (3.19), $\hat{\mathbf{j}}_l$ is a 3-dimensional vector corresponding to the MN solution at voxel l, and $\mathbf{T}_l$ is the $3 \times n_s$ submatrix of $\mathbf{T}(\alpha)$ belonging to voxel l.

Equation (3.20) is well defined in the sense that the matrix$\left\{\left[\mathbf{\Sigma}_{\hat{\mathbf{j}}}\right]_{ll}\right\}^{-1/2}$ can always be obtained. For this, an SVD of $\left[\mathbf{\Sigma}_{\hat{\mathbf{j}}}\right]_{ll}$ can be used to compute the inverse square roots of the non-zero singular values (Wagner, 1998).

3.4 Standardized Weighted Low Resolution Electromagnetic Tomography

The MN method is known to lead to superficial source distributions. This bias towards superficial currents is associated to the attenuation of the MEG and EEG signals with increasing source distance to the electrodes and follows from equations (2.16) and (2.17). This problem is clearly illustrated by equation (3.12) which is a minimizer of a cost function composed of a least-square error and a penalty term that is a norm of the currents. This minimization process will bias the solution towards one which minimizes the norm, whereas the bias would normally be towards minimizing the error (when β or equivalent $\alpha = 0$). If two different PCD distributions can produce the same magnetic field signals (within a level of accuracy given by the regularization parameter), then the one in which the current sources are deep within the brain will require stronger sources to do so (see equation (2.16) and (2.17)). Thus, the solution with sources closer to the surface will have a smaller norm and consequently will be favored. To compensate for this effect and ensure that sources are likely to influence the EEG/MEG equally at the electrodes irrespective of their depth, deep sources are given *a priori* covariance larger than the covariance given to the superficial ones. Several methods have been proposed to generate the corresponding covariance matrix. One of them indexes the depth by the norm of the lead field for each source and the covariance component of this constraint is defined as a $3ng \times 3ng$ diagonal matrix $\mathbf{\Sigma_j} = \left(\mathrm{diag}\left(\mathbf{K}^T\mathbf{K}\right)\right)^{-1}$ (Ioannides et al., 1990; Grave de Peralta Menendez and Gonzalez Andino, 1998.).

For our new approach, swLORETA, we need to perform a normalization that compensates for the varying sensitivity of the sensors to current sources at different depths. For each current source location l, there are three columns in the lead field matrix $\mathbf{K}$ that corresponds to the three components at that position. These three columns describe how the measured electric/magnetic fields at each sensor depend on the current sources at location l. Therefore, a normalization which compensates for this fact must estimate the relative sensitivity and modify the corresponding columns of $\mathbf{K}$ to make the sensitivities equal for all l (Kohler et al., 1996; Fuchs et al., 1999).

To this end, an SVD is performed on the three columns of the lead field matrix that corresponds to position l. This SVD factors the submatrix as follows:

$$\mathbf{K}_l = \mathbf{U}_l \mathbf{\Gamma}_l \mathbf{V}_l^{\mathrm{T}} \tag{3.21}$$

The orthogonal matrices $\mathbf{U}_l$ and $\mathbf{V}_l$ represent rotations to a coordinate system which diagonalizes $\mathbf{K}_l$. Thus, the matrix $\mathbf{\Gamma}_l$ contains only three diagonal elements, which are the singular values of $\mathbf{K}_l$ ($\hat{e}_l^d \quad d = 1, 2, 3$) and represents the system sensitivity at voxel l. From these singular values the PCD covariance matrix ($\mathbf{\Sigma_j}$) can be constructed as follows:

$$\mathbf{\Sigma_j}^{1/2} = \mathbf{s}^{-1/2} \otimes \mathbf{I}_3 \tag{3.22}$$

where $\otimes$ denotes the Kronecker tensor product, $\mathbf{I}_3$ is the identity 3×3 matrix, and $\mathbf{s}$ is a diagonal

$n_g \times n_g$ matrix with diagonal element s_l be the maximum sensitivity at voxel l, i.e. s_l is the maximum of the diagonal elements of $\mathbf{\Gamma}_l$ ($\mathbf{s}_l = \max_{d=1}^{3} \hat{e}_l^d$) for $l = 1, \ldots, n_g$.

Taking the covariance matrix in this form[1], is equivalent to rewrite equation (3.23) as:

$$\mathbf{d} = \left(\mathbf{K}\, {\mathbf{\Sigma}_\mathbf{j}}^{1/2}\right) \left({\mathbf{\Sigma}_\mathbf{j}}^{-1/2}\, \mathbf{j}\right) + \mathbf{n} \tag{3.23}$$

where the new unknown variable (${\mathbf{\Sigma}_\mathbf{j}}^{-1/2}\mathbf{j}$) have the identity matrix as its variance. Using the normalized lead field $\tilde{\mathbf{K}} = \mathbf{K}\, {\mathbf{\Sigma}_\mathbf{j}}^{1/2}$as the lead field matrix $\mathbf{K}$ in equations (3.15)–(3.19) a "pre-standardized" PCD can be obtained from equation (3.20) as (Pascual-Marqui, 2002):

$$\tilde{\mathbf{j}} = {\mathbf{\Sigma}_\mathbf{j}}^{1/2}\, \hat{\mathbf{j}}_{sLORETA} \tag{3.24}$$

3.5 Analysis of Simulated Data

3.5.1 Description of the Simulations

In this section, the results of a study carried out to test the tomographic properties of the swLORETA approach and to compare it to the sLORETA method will be presented. For this analysis simulated MEG data was used.

The head-sensor arrangement was taken from a real experiment and the spatial setup of the sensors corresponded to the configuration of the magnetometers in a 4D Neuroimaging MAGNES 2500 WH system: 148 magnetometers arranged in an array uniformly distributed (mean inter-channel spacing of $2.9\,$cm). The head was modeled as a spherical, radial symmetric conductor (Hämäläinen et al., 1993), that was used to calculate the lead field with the aid of the Sarvas equation (Sarvas, 1987). An equivalent dipoles model was chosen to simulate the MEG signal. A 3D grid was then fitted to the back of the brain where each point represented an equivalent dipole that could have generated the MEG signals. A total of $9 \times 17 \times 17 = 2601$ points was used with a minimum distance of $7.8\,$mm in the x-axis and $8.7\,$mm in y-axis and z axis. The origin of the coordinate system was the meeting point between the x-direction through the nasion to inion and the y-axis through the left to the right ear; the z-axis was the axis pointing upward (to the vertex of the head). The 3D grid was further clipped by the grey and white matters. Consequently, only 1281 voxels of the total amount of voxels were finally located inside the source space. Due to the location of the source space, only the 90 sensors placed in the back of the helmet were selected for the simulations as shown in figure (3.1). Finally, the radial component of all simulated dipoles was removed before calculating the forward solution because it is silent in the selected head model (Sarvas, 1987).

[1] Note that this approach can be applied to any *prior* covariance matrix for the PCD ($\mathbf{\Sigma}_\mathbf{j}$), as long as it is positive definite, and there exists a meaningful decompositions of the form:
$\mathbf{\Sigma}_\mathbf{j} = \left({\mathbf{\Sigma}_\mathbf{j}}^{1/2}\right)^T \left({\mathbf{\Sigma}_\mathbf{j}}^{1/2}\right)$

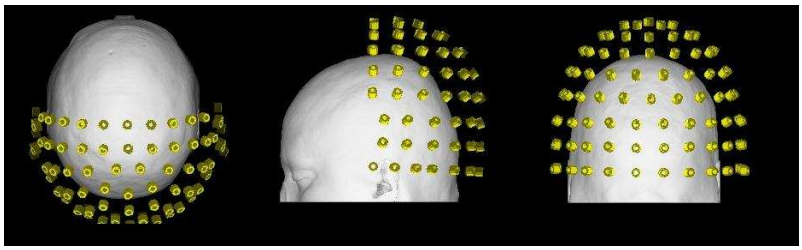

Figure 3.1: Sensor configuration.

3.5.2 Measures to Characterize the Methods

In the case of single dipole simulations, the following three measures were chosen to evaluate the properties of the inverse algorithms.

1. *Localization error*: it was defined as the Euclidean distance between the maximum of the current distribution and the position of the simulated dipole $\mathbf{r_0}$.

2. *Activation volume*: it was calculated by counting all voxels with strength above 60% of the maximum PCD distribution and then dividing that number by the total volume of the source space. Finally, this magnitude was expressed in percentage. The total volume of the source space was defined as the volume of a single voxel ($7.8\,\text{mm} \times 8.7\text{mm} \times 8.7\,\text{mm} = 590.382\,\text{mm}^3$) multiplied by the total number of voxels inside the source space (1281).

3. *Activation probability*: it counted how many times the simulated dipole position is active with a value greater than the 60% of the maximum PCD distribution and divided this value by the total number of realizations (300 noise realizations are performed for each dipole position (see section (3.5.3))). The selection of regions of interest according to the amount of voxels where the PCD lies above a particular threshold has been used often in real experiments (Alonso-Prieto et al., 2007; Barnikol et al., 2006).

In the case of two dipole simulations a measure named "*averaged activity deviation* (d')" is introduced to account for the localization error and the spread of the estimated PCD:

$$d' = \left(\frac{\sum_{i=1}^{n_g} \|\mathbf{j}_i\| \min_k \{\|\mathbf{r}_k - \mathbf{r}_i\|^2\}}{\sum_i^{n_g} \|\mathbf{j}_i\|} \right)^{\frac{1}{2}} \tag{3.25}$$

where $i = 1, \ldots, n_g$ is the number of voxels in the source space, $\mathbf{r}_k$ is the position of the original dipoles, $\mathbf{j}_i$ and $\mathbf{r}_i$ represents the estimated PCD and the center of the position of voxel i, respectively. Furthermore, values between 0 and 1 were normalized via

$$d = \frac{d'}{d_{\max}} \tag{3.26}$$

where $d_{\max}$ is the maximum possible value for d'. This corresponds to the current source being a δ-function located at the furthest possible voxel location.

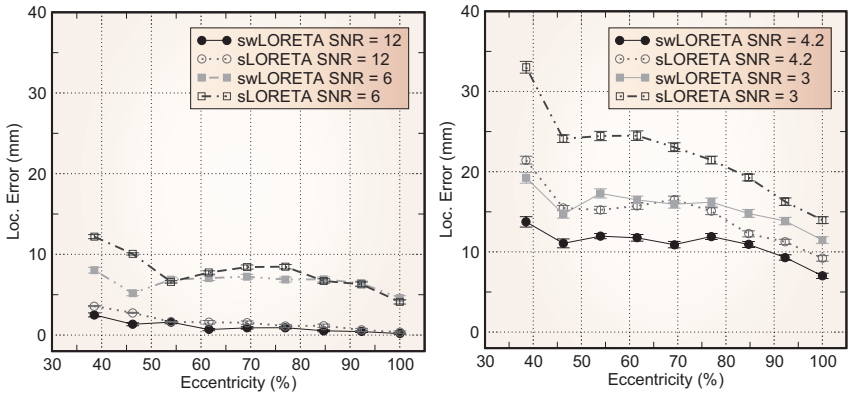

Figure 3.2: Localization error of both methods for single static dipole simulations. The eccentricity is first normalized to the head radius, measured horizontally along the x-axis and then expressed in % . Different SNR levels are tested. The error bars indicate one standard deviation of the localization error.

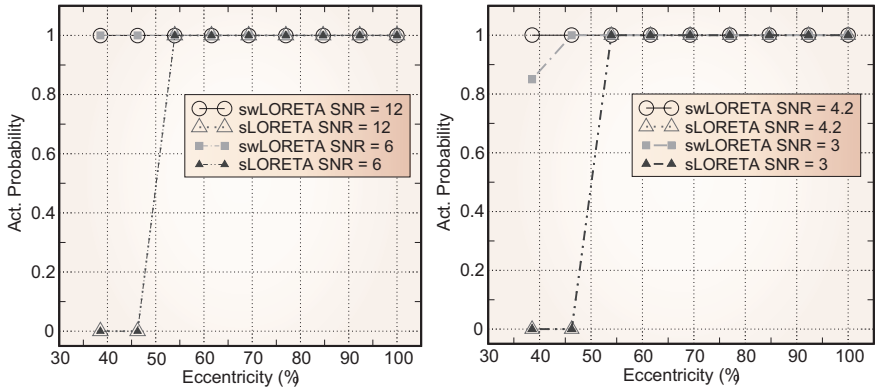

Figure 3.3: Activation probability for the swLORETA and sLORETA methods versus eccentricity.

3.5.3 Single Dipole Simulations

In this section, the tomographic properties of swLORETA will be illustrated using single dipole simulations.

A static dipole was simulated nine times along the x-axis through the center of the source space while the x coordinate of the test dipole varied from $-39\,\text{mm}$ to $-101.2\,\text{mm}$. The y and z coordinates were fixed at $2\,\text{mm}$ and $15\,\text{mm}$, respectively. For each given dipole position, the dipole was oriented in either the y or z direction. The strength of the dipoles was normalized to 1 after removing the radial component. Gaussian white noise with zero mean and standard deviation given by the desired signal-to-noise-ratio (SNR) was added to each detector after the forward solution. The SNR was defined as the maximal magnetic flux over all detectors divided by the standard deviation of the noise. Four different levels of noise were analyzed and 300 noise realizations for each dipole position were used to estimate the mean and standard error. The three measures described in section (3.5.2) were calculated for each of the nine dipoles with y or z orientations and then the result of each measure was averaged over both orientations (figures (3.2-3.4)).

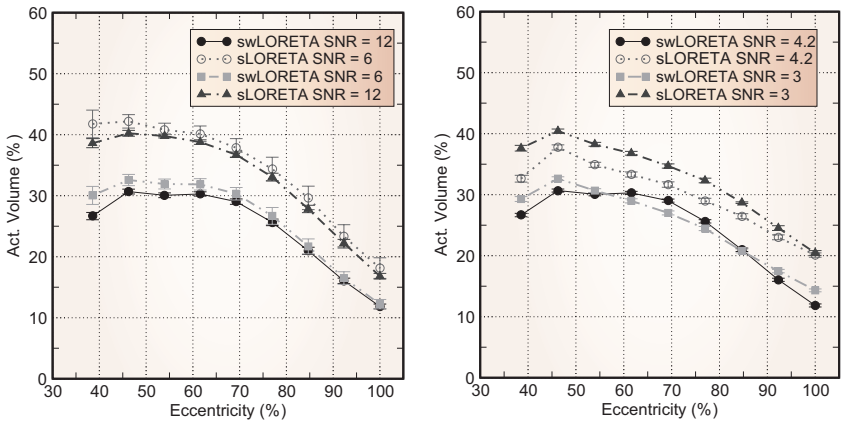

Figure 3.4: Activation volume measured using a threshold of 60% of the maximum versus eccentricity.

The localization error of both methods is shown in figure (3.2). As expected, for both methods the localization error decreased as the eccentricity increased but swLORETA presented the best performance for all eccentricity and SNR values. Especially, note that the differences between both methods increased when the SNR decreased and the swLORETA localization error was always the smallest. This tendency was especially marked for deep sources.

On the other hand, the activation probability index was always maximal in the case of swLORETA except for the lowest value of SNR and eccentricity (figure (3.3)). In contrast, for sLORETA it was maximal only for eccentricities above 50% while for deep sources it drops to zero. This result was true despite the fact that the activation volume of swLORETA was smaller than the activation volume of sLORETA in all simulated conditions (figures (3.4) and (3.5)). These findings demonstrated the ability of swLORETA to focus the reconstructed PCD around the true position of the dipole.

When a single dipole was placed in all possible positions according to the source space used and with orientations x, y and z, the tomographic properties of swLORETA remained better than those of sLORETA (figure (3.6)).

3.5.4 Two Dipoles Simulations

In a second step a 2-dipole configuration set that consists of several two-dipole arrangements was implemented. The new arrangements differ only with respect to their positions and mutual orientations. Thus, the z-component of all dipole positions was fixed ($z = 15\,\text{mm}$), the superficial position of dipole no. 2 in the right hemisphere remained the same through all configurations ($x = -93\,\text{mm}$ and $y = 44\,\text{mm}$) and current dipole no. 1 approached dipole no. 2 from the left hemisphere and stayed superficial in all settings.

Parallel and orthogonal relative orientations of the dipoles (figure (3.7)) were tested. In parallel configurations, both dipoles were arranged in a line parallel to the y-axis. In the orthogonal configurations, one dipole was oriented along the y axis, and the other along the z axis. The averaged activity deviation index was used to characterize the properties of both methods.

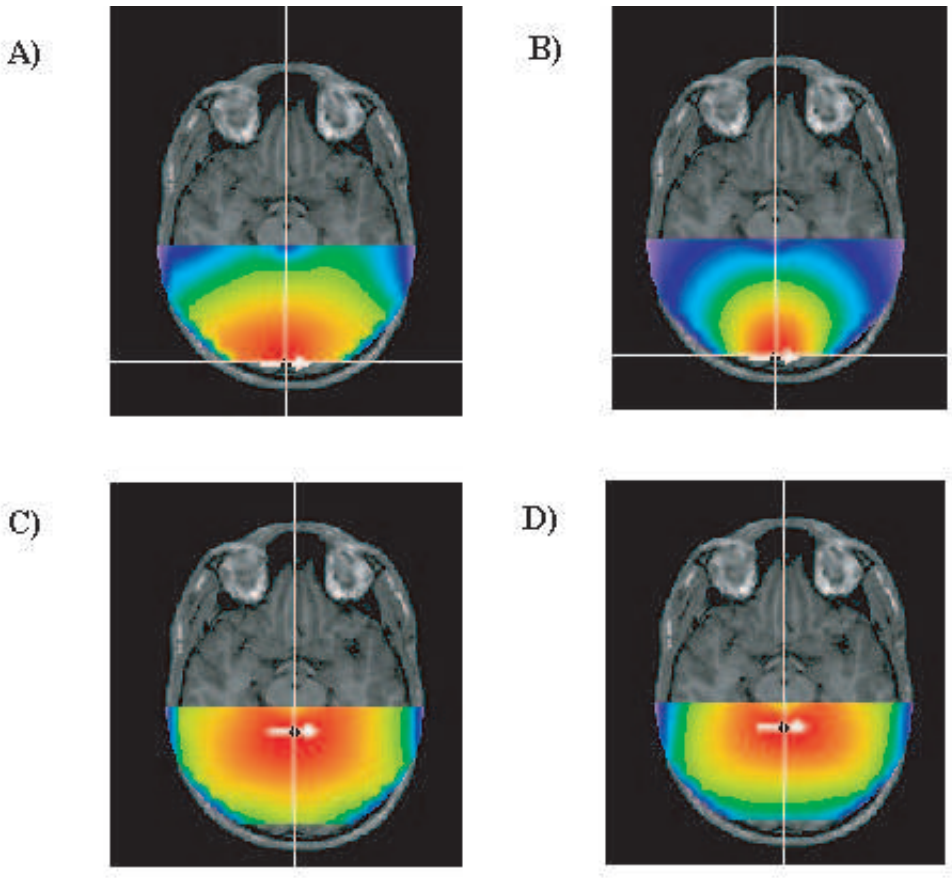

Figure 3.5: A) and C) show the reconstructed current source densities for two different simulated dipole positions using the sLORETA method. B) and D) show the swLORETA solution for the same two configurations. The arrows indicate the positions of the original dipoles. A SNR = 6 was used for this simulation. As can been seen for this figure, the activity volume of swLORETA method is smaller than the activity volume of sLORETA method. The cursor represents the location of the maximum PCD.

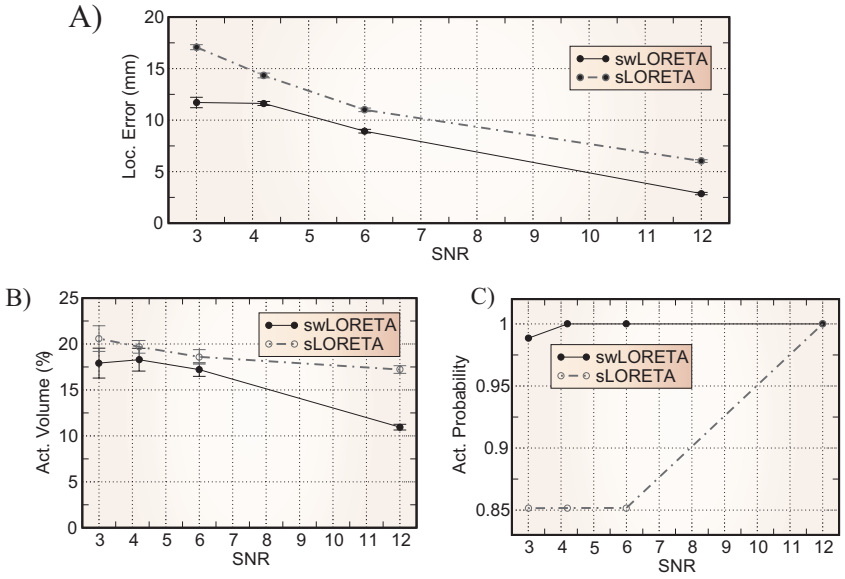

Figure 3.6: Localization error and angle difference averaged across different positions and orientations of a static dipole versus SNR for both methods.

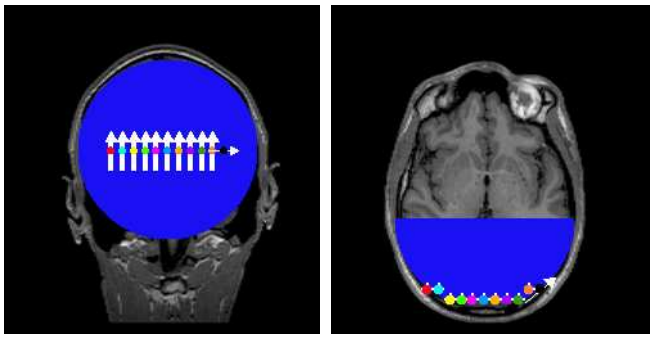

Figure 3.7: Orthogonal configurations: Dipole no. 2 indicated by a black spot does not change its position between the configurations whereas the other dipole is approaching. Each colored spot at dipole no. 1 describes a different configuration.

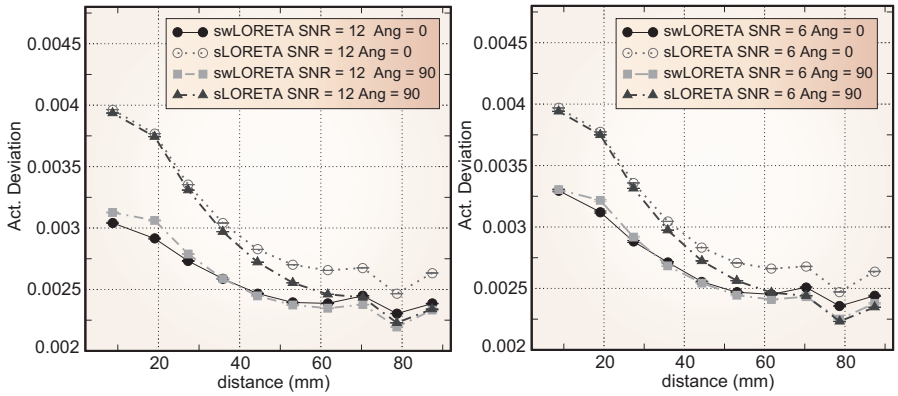

Figure 3.8: Averaged activity deviation versus the dipole distances for different SNR and relative dipole orientations.

As can be seen in figure (3.8), both methods showed the same tendency: for a given angle value (0 or 90), the activation deviation index exhibited the same values for different SNR but all values obtained when angle = 0 were higher than those obtained when angle = 90. Additionally, the activation deviation values decreased when the distance between both dipoles increased. On the other hand, the swLORETA activation deviation index was always smaller than that of sLORETA. These results suggested that the spatial resolution of swLORETA is higher than that of the sLORETA in the presence of two dipoles simultaneously active.

Both methods were able to separate the sources when those sources were distant, equally superficial or had an antiparallel orientation. It is important to note that the methods were able to separate parallel sources only when they were very distant. It is also worth mentioning that the swLORETA method separated sources for the antiparallel better than the sLORETA method (figure (3.9).

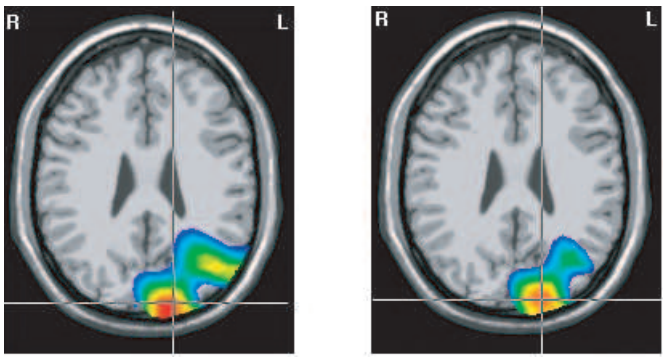

Figure 3.9: Current source reconstruction for nearby antiparallel sources using both sLORETA and swLORETA. The swLORETA reconstruction (left) is able to distinguish the two sources clearly. The sLORETA reconstruction (right) is much less clearly separated. The sources are both equally superficial, and are located 35mm apart. The cursor represents the location of the maximum PCD. (SNR $= 6$).

3.6 Analysis of Experimental Data

In order to test the applicability of swLORETA inverse algorithm under real-life circumstances, a classical visual spatial attention experiment was designed and analyzed. This kind of experiments addresses the attentional mechanisms involved in the selection of relevant information at multiple stages of visual processing. It was selected because the time course of attentional effect as well as the brain regions associated to it have been studied extensively. Consequently, it is possible to elaborate a precise working hypothesis about the active source. The next paragraphs summarizes the findings reported in the spatial attention literature.

In a typical spatial attention task two conditions are compared: an attended condition, in which subjects focus attention on visual stimuli placed in attended locations of the visual field; and an unattended condition, in which similar stimulation environment is present but subjects focus attention elsewhere in the visual field. The paradigmatic finding is that the perception and discrimination of the stimuli placed in the attended location is significantly facilitated (Luck et al., 1996, 1997; Martinez et al., 1999, 2001,

2007). EEG/MEG studies have demonstrated that this facilitation occurs within the first 100 ms after stimuli presentation and remains until about 180 ms since the amplitude of both the P1 ($80 - 120$ ms) and N1 components ($140 - 180$ ms) is higher for the attended conditions especially over the posterior scalp (Luck et al., 1996; Martinez et al., 1999, 2001, 2007). The neural generators of those attention sensitive components have been determined using dipole and distributed source modeling methods as well as co-registration with PET and fMRI. Most of the studies locate the neural generators of P1 component in mid occipital regions around V3/V3a, the immediately anterior middle occipital gyrus, the ventral occipital cortex around V4 and the fusiform gyrus (Luck et al., 1997). Usually, the highest activation is found in the hemisphere contralateral to the attended visual field. The N1 attention effect has been associated to the activation of parietal, ventral occipital-temporal and frontal areas (Russo et al., 2002, 2003). Recordings of single unit activity in monkeys (Luck et al., 1996, 1997; Martinez et al., 1999, 2001, 2007) and fMRI studies in humans (Martinez et al., 2001, 1999) have confirmed the involvement of extrastriate visual areas V2, V3a, V4, MT, the inferotemporal cortex and the posterior parietal cortex

3.6.1 Materials and Methods

Subjects

Twelve right handed subjects (all females, mean age 29 ± 6 years), who had normal or corrected to normal vision, participated in the study after giving their informed consent. All subjects were healthy and had no signs of neurological or psychological impairments. The study was in accordance with the Declaration of Helsinki and the Institutional Committee on Human Research of the University of Ilmeanu where the data was registered.

Stimuli and procedure

The stimulus consisted of a rectangular black and white checkerboard (angular size: $5.5°$) of 25 rectangles (angular size of each rectangle: $0.01°$, Michelson's contrast: 50%) and a black arrow (angular size: $1.7°$). It was placed at the horizontal meridian: the arrow was placed in the center of the screen and the stimulus either in the left or right visual hemifield (distance between arrow and checkerboard: 1 cm) (figure (3.10)). It was displayed on a white background (Michelson's contrast between stimulus and background: 50%), generated using an LCD Samsung monitor (refreshing rate: 60 Hz, mean brightness: 300 cd/m^2) and presented to both eyes. The colors of the checkerboard were reversed in a counterphase square wave temporal pattern at 1.67 Hz (1 contrast reversal every 600 ms). The interval inter-stimulus was a random value between 300 and 500 ms (figure (3.10)). Subjects were comfortably seated in front of the monitor and they were instructed to fixate the arrow through out the experiment while attending to the visual hemifield it pointed to. They had to press a key when they detected that the white checks turned gray. Eight blocks of 100 trials each were presented. Within a block the arrow was always pointing to the same hemifield and targets had a 20% chance to be presented. From the remaining 80% standard trials, 40% was presented in the attended hemifield. Task requirements concerned with working memory load and attention shifting, which could potentially confound the interpretation

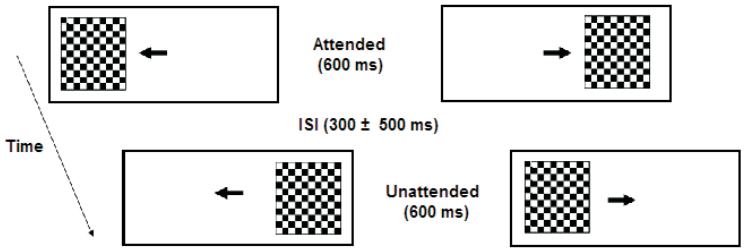

Figure 3.10: Experimental stimuli and design. See text for further details.

of spatial attention effects, were controlled. Thus, subjects were instructed that the cue (central arrow) was going to be pointing always to the same hemifield within a block. Furthermore, cue and stimulus were always presented together. Consequently, subjects need neither to hold the spatial information in working memory nor to shift attention to other locations within a block (except for the first trial of each block which was disregarded from the analysis). Moreover, targets were presented only to maintain a proper level in subjects' attention and motivation during the task but they were not included in the analysis. Instead, only standard attended and unattended stimuli were analyzed In this way, it was avoided possible confounds with brain functions related to target processing and motor response.

Electrophysiological recording

The EEG analog signal was recorded continuously from 62 scalp sites using the A.N.T. (A.N.T., Enschede, The Netherlands) amplifier (gain: 30000) and 62 Ag-AgCl electrodes mounted on a WaveGuard cap according to the $10-5$ electrode system. The impedance of all electrodes was $< 40\,\mathrm{k}\Omega$ at the beginning of the experiment. EEG was recorded using a $0.01 - 200\,\mathrm{Hz}$ bandpass filter and the signals were sampled at $512\,\mathrm{Hz}$. All recordings were referenced to linked mastoids and then average-referenced off-line.

Data processing

The raw data waveforms were high-pass filtered by convolving them with a 4th order Butterworth filter with half power cutt-off of $1\,\mathrm{Hz}$. We also applied a Notch filter centered at $50\,\mathrm{Hz}$. Eye movements were corrected using a spatial filtering method based on pre-selection approach (Ille et al., 2002). In addition, remaining artifacts exceeding $\pm 75\,\mu\mathrm{V}$ in any channel were rejected. Artifact free data was divided into epochs ranging from $-200\,\mathrm{ms}$ to $800\,\mathrm{ms}$ after stimulus onset for both the standard attended and the standard unattended conditions. Then, for each trial, baseline correction was applied by subtracting from the post-stimulus interval the mean amplitude of the pre-stimulus interval between $200\,\mathrm{ms}$ and $100\,\mathrm{ms}$.

ERP analysis

The selected epochs were averaged and then ERP amplitude analysis was performed in order to confirm that the experimental design elicited the P1 and N1 attention effect described in the literature and thus

validate the application of the inverse method. For each subject and experimental condition P1 and N1 components were defined as the most positive and negative peaks that appeared between $80-120$ ms and $140-180$ ms, respectively (Martinez et al., 2007). The right and left electrodes where ERPs were largest were identified among a group of 12 posterior electrode sites in each hemisphere (Cp1-Cp2, Cp3-Cp4, Cp5-Cp6, Tp7-Tp8, P1-P2, P3-P4, P5-P6, P7-P8, PO3-PO4, PO5-PO6, PO7-PO8, O1-O2). Then, the corresponding amplitude values were submitted to statistical analysis. To this end, Friedman ANOVA test ($p < 0.05$) was used and, if the test results were significant, planned comparisons were made using the Wilcoxon Matched Pairs Test ($p < 0.05$; Bonferroni corrected for multiple comparisons).

Source analysis

Afterwards, brain sources of P1 and N1 components were modeled using swLORETA. To this end, the grand averaged waveforms were first obtained for each condition separately and then two analysis windows ($80-120$ ms and $140-180$ ms) were determined. Finally, swLORETA was applied. In order to confirm the obtained results, the analysis was repeated for each subject as well. Regions of interests were selected by applying a 65% cut off threshold to the activation strength of the sources at the time of the peak. Note that difference waves were not used and instead the reconstruction on each condition was performed separately. This was done to avoid possible confounds in P1 and N1 components latency and amplitude which in turn may affect the source localization analysis.

3.6.2 Results

ERP results

As in previous studies P1 and N1 components increased their amplitude during the attended condition. Friedman ANOVA analysis demonstrated that the differences between attended and unattended conditions were significant for the P1 ($Chi^2 = 62.03$; $df = 7$; $p < 0.00$) and for the N1 components ($Chi^2 = 41.28$; $df = 7$; $p < 0.00$). Planned comparisons using Wilcoxon Matched Pair Test (Bonferroni corrected) showed that the P1 attention effect was present only in the electrode placed in the brain hemisphere contralateral to the stimulated visual hemifield (table (3.1)). For the N1 component the attention effect was present in both brain hemispheres irrespective of the stimulation hemifield although the mean amplitude was higher over the contralateral hemisphere (table (3.2)). Figure (3.11) illustrates the grand averaged scalp topography of both components for all conditions together with the ERP waveforms at the electrode location where components presented the highest amplitude.

Source analysis

Brain areas active during the time window of P1 component were localized in striate visual area BA 17, middle occipital gyrus next to BA 18, and middle temporal gyrus next to BA 37 irrespective of the experimental conditions: attended or unattended stimuli (figure (3.12)). Interestingly, the activation strength was always higher in the attended condition (figure (3.12)). Additionally, in the attended condition the right hemifield stimulation evoked bilateral activations while the left hemifield stimulation

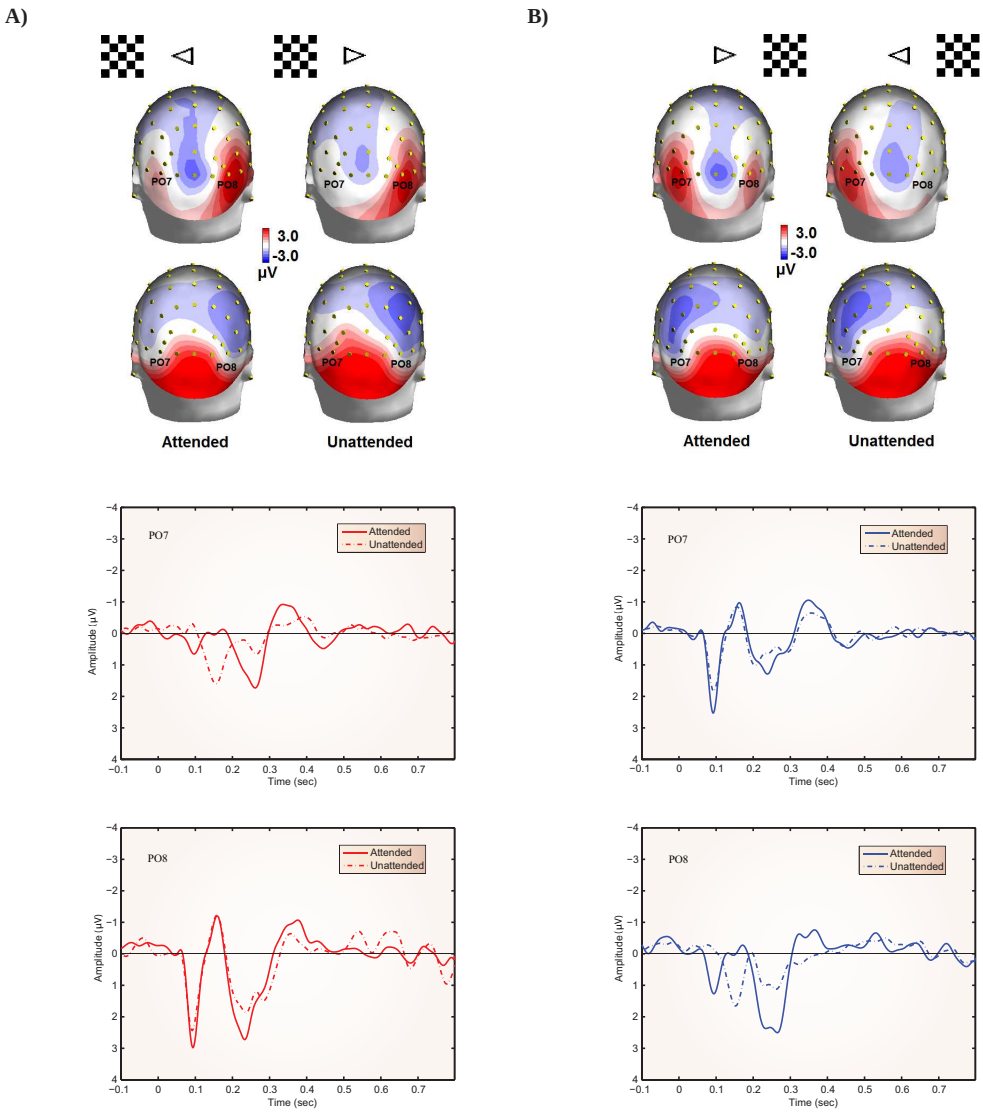

Figure 3.11: Grand averaged scalp topography of P1 and N1 components for both conditions and stimulation hemifields. The bottom part of the image shows the grand averaged waveforms for two electrodes, PO7 and PO8.

P1 amplitude (μV)				
Stimulation hemifield/ Electrodes location	Mean amplitude $\pm$ SD		Z	p-level
	Attended	Unattended		
Left/Right	3.89 ± 1.77	2.87 ± 1.34	3.06	< 0.01
Right/Left	3.02 ± 1.40	2.22 ± 1.08	2.35	< 0.01
Left/Left	1.37 ± 1.13	0.51 ± 0.75	2.43	ns
Right/Right	1.31 ± 1.30	0.59 ± 0.86	2.35	ns

Table 3.1: Results of the statistical comparisons between attended and unattended conditions for the P1 components. ERP amplitudes evoked by the attended stimulus in a given electrode location (right or left hemispheres) were compared to the amplitude evoked by the unattended stimulus in a similar electrode location (Wilcoxon Matched Pairs test, $p < 0.01$, Bonferroni corrected).

N1 amplitude (μV)				
Stimulation hemifield/ Electrodes location	Mean amplitude $\pm$ SD		Z	p-level
	Attended	Unattended		
Left/Right	-3.09 ± 1.66	-1.82 ± 1.07	3.06	< 0.01
Right/Left	-2.83 ± 1.13	-1.98 ± 1.04	3.06	< 0.01
Left/Left	-1.90 ± 1.24	-0.82 ± 0.87	2.90	< 0.01
Right/Right	-2.55 ± 1.44	-1.24 ± 0.73	2.82	< 0.01

Table 3.2: Results of the statistical comparisons between attended and unattended conditions for the N1 components. ERP amplitudes evoked by the attended stimulus in a given electrode location (right or left hemispheres) were compared to the amplitude evoked by the unattended stimulus in a similar electrode location (Wilcoxon Matched Pairs test, $p < 0.01$, Bonferroni corrected).

evoked contralateral activations (figure (3.12)). The unattended condition always evoked contralateral activations.

Brain sources found to be active during the time window of N1 component were located in the occipital gyrus next to BA 18 and 19, in the temporal fusiform gyrus BA 37 and in the middle frontal gyrus next to BA 10 of both hemispheres for both stimulation conditions. As in the case of P1 component, attended conditions presented the highest activation strength (figure (3.13)).

3.6.3 Discussion

In this section, the swLORETA method was applied to a classical spatial attention experiment in order to test its tomographic properties in a life-like environment.

It was found that both experimental conditions evoked the activation of similar areas but their activation strength differed. This result is in line with the idea that spatial attention modulation behaves as a selective amplification of neuronal activity between 80 and 200 ms after stimuli onset (Hillyard and Anllo-Vento, 1998). Active areas were localized in the striate visual area BA 17, middle occipital gyrus next to BA 18, and middle temporal gyrus next to BA 37 between 80 and 120 ms, similar to previous studies in macaque monkeys and humans (Hillyard and Anllo-Vento, 1998; Luck et al., 1997, 1996).

Additionally, the results suggest the existence of attention modulations in striate visual area, V1. This outcome has previously been found in fMRI and iEEG studies but has been more elusive in scalp EEG experiments probably because the attentional modulation of V1 neuronal response is not as strong as the modulation of extrastriate areas. Indeed, it has been suggested that the attentional effect; as the suppressive interactions among competitive, simultaneously presented stimuli; scales with receptive field sizes (Kastner et al., 1999; Pessoa et al., 2003). In other words, it may take place most effectively in anterior extrastriate visual areas, which have big receptive fields, while it may be weak in V1, which has small receptive fields (Kastner et al., 1999; Pessoa et al., 2003). In this study, the experimental design, which minimizes the demands to working memory and attention shifting while emphasizes early visual processing; the quality of the data as well as the tomographic characteristics of swLORETA may have helped to isolate the contribution of such a weak source to the scalp voltage distribution. Nonetheless, it should be considered also that swLORETA have a tendency to smooth out the sources as

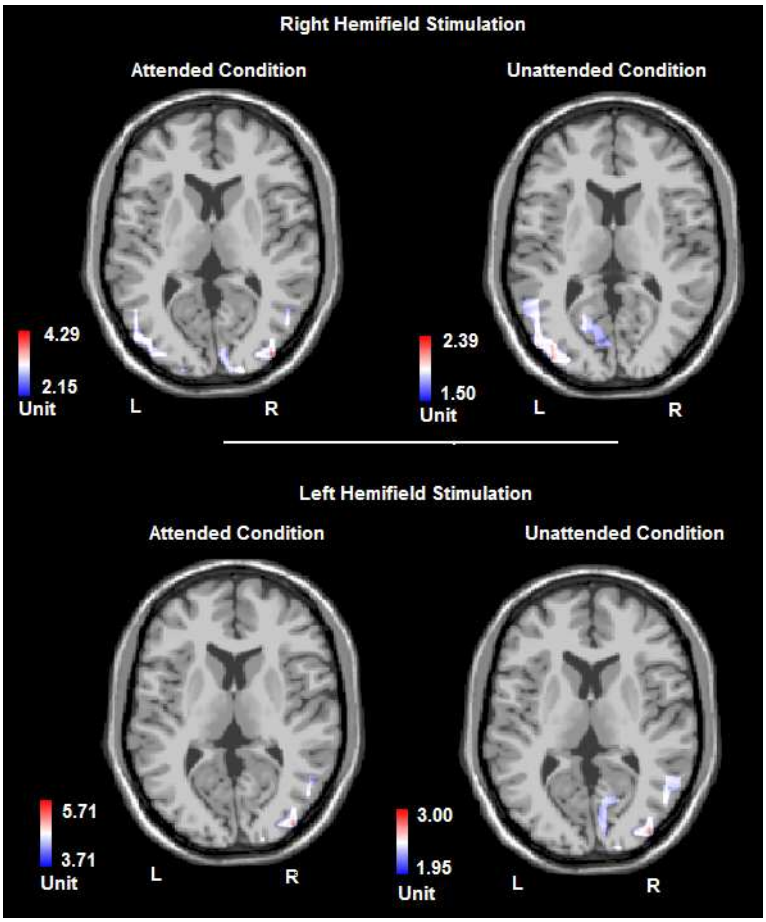

Figure 3.12: swLORETA source reconstruction results. The reconstruction was applied on the Grand Average waveform during the time interval of P1 component.

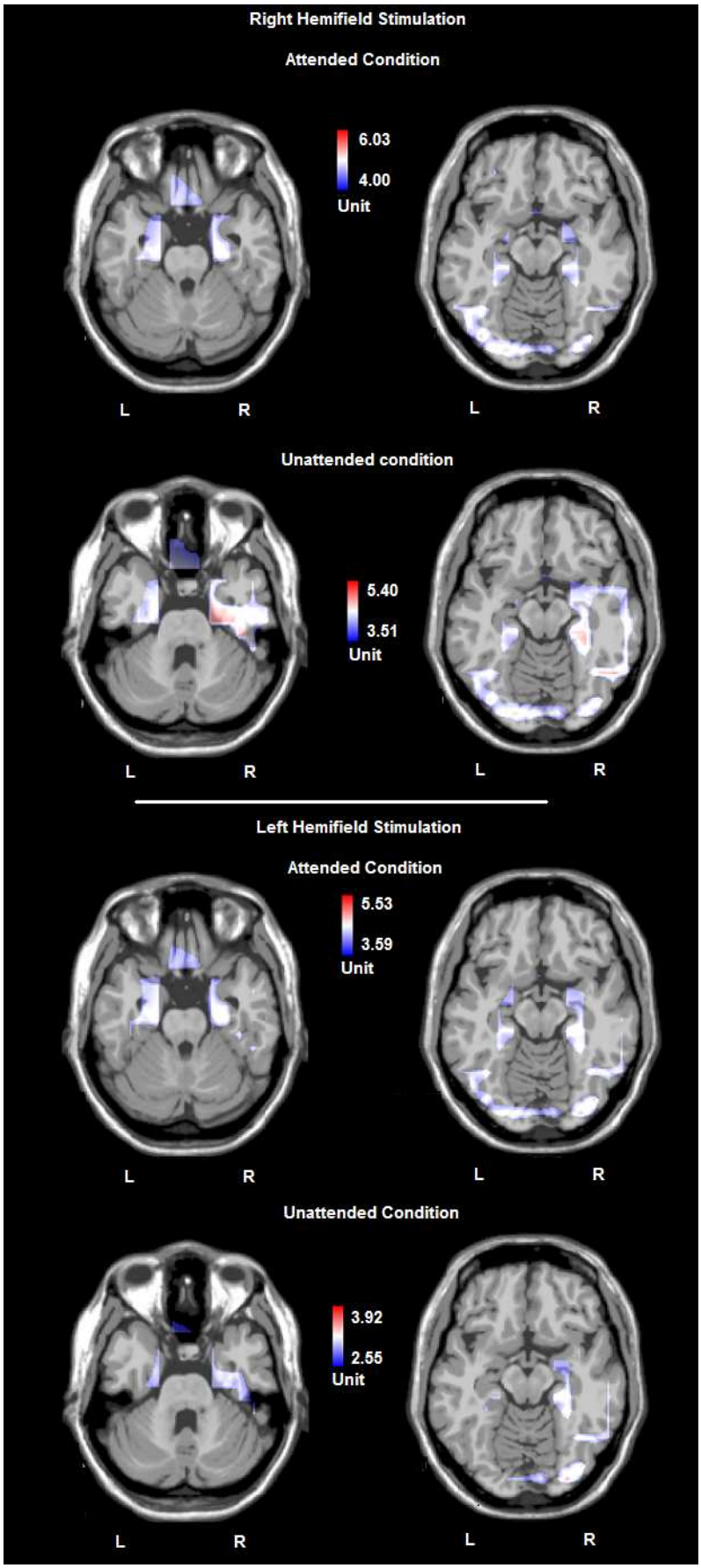

Figure 3.13: swLORETA source reconstruction results. The reconstruction was applied on the Grand Average waveform during the time interval of N1 component.

the simulation studies have shown. This fact may have hindered the possibility of resolving the activation of neighboring areas such as V2 and V3. It has been consistently reported that the activation of this last area is enhanced by attention (Martinez et al., 2007, 2001; Russo et al., 2003). Therefore, we cannot rule out the possibility that the activation found in this study for V1 corresponds to a source in V2 which has been smoothed out by the inverse reconstruction method employed.

Interesting results were also found concerning the differential activation of both brain hemispheres. Thus, the activation strength of the above mentioned brain areas reach the imposed cut off threshold in both brain hemispheres for right hemifield stimulation and only in the right hemifield for left hemifield stimulation. This observation is in line with previous reports that have demonstrated that severe contralesional neglect is usually seen after lesions to the right hemisphere but not after lesions to the left hemisphere (Lynch and McLaren, 1989; Watson et al., 1994). This may indicate that the right hemisphere controls the distribution of spatial attention across the entire visual hemifield and thus can respond to a stimuli presented either in the right or in the left visual hemifield. In contrast, the left hemisphere regulates mainly the contralateral hemifield and thus responds to contralateral stimulation (Gitelman et al., 1999; Spiers et al., 1990; Heilman et al., 1985).

Between 140 and 180 ms attentional modulations were localized in the occipital gyrus (BA 18 and 19), temporal fusiform gyrus (BA 37) and middle frontal gyrus (BA 10). Previously, it has been established that brain regions continue active after their participation in the feedforward sweep (Lamme and Roelfsema, 2000). This recurrent processing is important for incorporating the information coming from higher areas into their responses through lateral and feedback connections (Lamme and Roelfsema, 2000). Consequently, it is not surprising that extrastriate visual areas are found active beyond 100 ms. Additionally, frontal area BA 10 was found active to. This area has been related to executive functions (Alvarez and Emory, 2006; Jurado and Rosselli, 2007) which were indeed emphasized by our experiment. Thus, to achieve a good performance in the applied task processes such as concentrated attention on a given visual hemifield, goals maintaining, stimulus judgment and decision making were required.

Summarizing, the result were in good agreement with previous reports that have used a wide variety of analysis techniques. Consequently, they give support to the conclusion that swLORETA is able to retrieve correctly brain sources under real life conditions.

3.7 Conclusions

The swLORETA method presented in this chapter introduces an SVD lead field weighting to improve the tomographic performance of widely used distributed inverse methods such as MN and sLORETA. In this way, the benefits of the more appropiate lead field weights was combined with the benefits of sLORETA. Indeed, the new approach has several advantages, it is tomographic properties are more robust with respect to the SNR as well as its ability to separate simultaneously active sources, as the single and two dipoles simulations demonstrated. Especially, swLORETA exhibits the maximal probability index, which approximates very well the performance of an inverse method under real experimental conditions. Only for very deep sources (eccentricities below 50%) swLORETA activity probability index is different

from 1. Moreover, swLORETA is able to reconstruct accurately the EEG/MEG generators under real experimental conditions as demonstrated by analyzing a spatial attention experiment.

4 *Time Frequency Domain Inverse Solution*

> Meaning and reality were not hidden
> somewhere behind things, they were in them,
> in all of them.
>
> Hermann Hesse

4.1 Introduction

For a long time it has been suggested that oscillatory neuroelectric activity is one of the candidate mechanisms used by neurons placed in different and sometimes distant regions of the brain to interact over time and produce a unified cognitive experience (Freeman, 1998; Basar et al., 1999; Varela et al., 2001). Thus, time varying patterns of theta, alpha, beta and gamma waves have been related to sensory and cognitive functions such as memory, attention and feature binding (Kahana, 2006; Kelly et al., 2006; Klimesch, 1999; Luu et al., 2004). Consequently, it is important to develop analysis methods able to characterize the dynamics of the brain signals recorded on the scalp in the time and frequency domains, as well as to localize the sources of those time varying spectral components. This combined time-frequency representation overcomes the inadequacy of frequency domain analysis to fully capture the nature of non-stationary signals. Thus, in contrast to frequency domain analysis, it is able to describe how the spectral content of a given signal evolves over time. This characteristic may even become crucial under some circumstances. Imagine, for example, that two EEG signals are acquired in response to the presentation of a top part of a face (condition A) and in response to a bottom part of a face (condition B). When applying FFT, it can be obtained that both signals exhibit similar spectral peaks at $10\,\mathrm{Hz}$ and $3\,\mathrm{Hz}$. From this analysis one can conclude that both experimental conditions provoke a similar brain response. A time-frequency domain analysis, on the other hand, would reveal that the dynamics response of this process is actually different. In order words, while condition A provokes the $3\,\mathrm{Hz}$ peak at $100\,\mathrm{ms}$ and the $10\,\mathrm{Hz}$ peak at $170\,\mathrm{ms}$ the opposite holds for condition B. In this way, it is possible to disentangle apparently similar brain patterns.

In this chapter, it will be explained how swLORETA algorithm can be used to find the anatomical generators of spectral components of the scalp data. Specifically, swLORETA will be used to compute a time-resolved spectrum of the "electric neuronal activity". Finally, swLORETA tomography properties will be illustrated by means of the spatial attention experiment already introduced.

4.2 swLORETA in the Time Frequency Domain

To estimate a time resolved spectrum of the current sources that generate the EEG/MEG a method that involves three basic steps is proposed. These three steps are 1) time resolved spectro-temporal representation of the EEG/MEG data, 2) calculation of the spectro-temporal representation for the swLORETA estimate and 3) calculation of the swLORETA time-frequency power spectrum. Note that to study evoked oscillations, which bears a constant latency and phase relationship with the eliciting event, all 3 steps are applied on the averaged waveforms. To study induced activity, which bears a loose relationship with the stimulus, steps 1 and 2 are repeated for each trial separately and then, the results are averaged across trials in step 3.

4.2.1 The Hilbert Transform

To decompose a signal in its time-frequency domain a variety of methods have been developed, for example, the short time Fourier transform, the wavelet transform (Lachaux et al., 2002) and the Complex demodulation (Papp and Ktonas, 1977). This work will be limited to the use of the analytic signal based on the Hilbert transform (Gabor, 1946; Bendat and Piersol, 2000) but any of the other methods can be used in a similar fashion. A time resolved spectral analysis of a signal $s(t)$ will yield a two dimensional representation of the signal in time-frequency product space. Such spectro-temporal representation is a complex valued function which consists of amplitude value $A(w,t)$ and a phase value $\psi(w,t)$, such that:

$$z(w,t) = A(w,t)\, e^{i\psi(w,t)} \tag{4.1}$$

In other words, to estimate the amplitude or the phase at time t and frequency w one first needs to determine the above complex value. Note that this is also needed to estimate more complex measures, e.g. phase synchronization and coherence, which will be used later in this thesis. The first step to compute this spectro-temporal representation is to decompose the signal $s(t)$ into neighboring frequency components by applying a band pass filter with bandwidth center at w given the signal $s(w,t)$. After that, the complex value representation given by equation (4.1) has to be computed for the band-pass signal $s(w,t)$. One standard method to compute such a complex representation is to form the so called analytic signal. The basic idea is that negative frequency components of the Fourier transform of a real valued signal are redundant so they can be discarded without losing any of the signal's information. This characteristic is due to the symmetry of the frequency domain representation around the origin (see appendix (B) details) that is:

$$S(-w) = S(w)^T$$

where $S(w)$ is the Fourier transform of the real value signal $s(w,t)$ and T denotes the complex conjugate. Moreover, the analytic signal is written in the following complex form:

$$z(w,t) = s(w,t) + i\,\tilde{s}(w,t) \tag{4.2}$$

where $s(w,t)$ is the real valued signal, $\tilde{s}(w,t)$ is the Hilbert transform and i is the imaginary unit. To arrive to this expression the Fourier transform of the analytic signal should be defined as:

$$\begin{aligned} Z(w) &:= \begin{cases} 2S(w) & \text{for } w > 0, \\ S(w) & \text{for } w = 0, \\ 0 & \text{for } w < 0 \end{cases} \\ &= S(w) \cdot 2U(w) \end{aligned}$$

where $S(w)$ is the Fourier transform of the real valued signal $s(w,t)$ and $U(w)$ is the Heaviside step function. This expression only includes the non-negative frequency components of $S(w)$. Nonetheless, this operation is reversible since it is possible to get the original spectrum of the signal by taking into account the Hermitian property of $S(w)$ as:

$$S(w) = \begin{cases} \frac{1}{2}Z(w) & \text{for } w > 0, \\ S(|w|)^T & \text{for } w < 0. \end{cases}$$

Finally, taking the inverse Fourier transform of $Z(w)$ the imaginary part of the analytic signal in equation (4.2) is given by:

$$\tilde{s}(w,t) = \frac{1}{\pi}\text{P.V.} \int_{-\infty}^{\infty} \frac{s(w,\tau)}{t-\tau}\,\mathrm{d}\tau \tag{4.3}$$

Equation (4.3) is named the Hilbert transform of the real valued signal $s(w,t)$ (for more details about the derivation of this equation see appendix (B)). The magnitude $s(w,t)$ and $\tilde{s}(w,t)$ can be used to compute the instantaneous amplitude and phase of equation (4.2) as:

$$\begin{aligned} A(w,t) &= |A(w,t)| = \sqrt{s_w^2(t) + \tilde{s}_w^2(t)} \\ \psi(w,t) &= \arg\left(s(w,t)\right) \end{aligned}$$

where $\arg$ represents the complex argument function.

Both the geometrical interpretation of the instantaneous amplitude $A(w,t)$ and phase $\psi(w,t)$ are

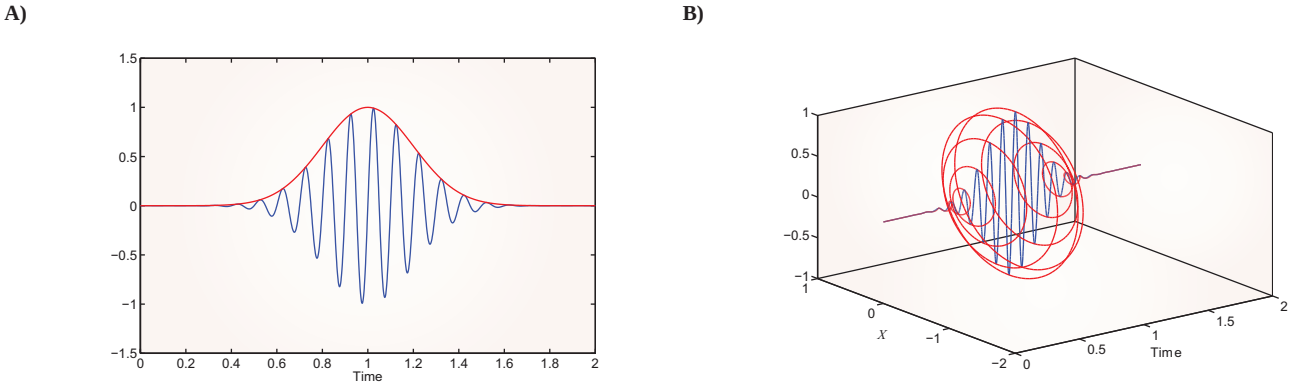

Figure 4.1: A) The phase (red curve) is geometrically interpreted as the angle between a fixed direction (positive x axis) and the current system state (blue curve). B) The signal is shown in red and the magnitude of its analytic signal in blue. Note the envelope effect.

represented in figure (4.1) for each time point. Note that for narrow band signals the modulus of the analytic signal coincide with the envelope of the filter signal $s(w,t)$ (Bendat and Piersol, 2000). In other words, it corresponds to the amplitude of the oscillation which is a measure of the signal spectrum content. In the next sections, the procedure of computing the analytic signal will be called the "Hilbert analysis" and the operation of applying the Hilbert analysis to the function f will be denoted as $\hat{H}f$. Also, the linear property of the Hilbert analysis will be used. This means that given the function $f(t)$ as $f(t) = c_1 f_1(t) + c_2 f_2(t)$ where the Hilbert transform of the $f_1(t)$ and f_2 exist then:

$$\hat{H}f(t) = \hat{H}\left(c_1 f_1(t) + c_2 f_2(t)\right) = c_1 \hat{H} f_1(t) + c_2 \hat{H} f_2(t) \tag{4.4}$$

This property will allow developing a computationally efficient algorithm to determine the spectro-temporal representation of the brain structures that generates the EEG/MEG signals.

4.2.2 Source Spectro-Temporal Estimation

To determine the spectral evolution of the brain areas that produce the recorded EEG/MEG signals it would be sufficient to apply the algorithm described in section (4.2.1) to the swLORETA estimates given by equations (3.20) and (3.24). Unfortunately, this procedure is mathematically correct but computationally expensive because it involves the calculation of the Hilbert transform for each of the usually thousands of source space points. If unaveraged signal is used this number multiplies by the amount of trials. Fortunately, the linear properties of both the Hilbert Transform and swLORETA can be exploited to overcome this difficulty. Thus, the spectro-temporal representation of the swLORETA result for the ith voxel can be written as:

$$\mathbf{\Omega}_l(w,t) = \hat{\mathbf{H}}\,\mathbf{j}_{swLORETA,l}(w,t) \tag{4.5}$$

where $\mathbf{\Omega}_l$ is a 3-dimensional vector which contains the analytic signal for the rows of the swLORETA

estimates, $\mathbf{j}_{swLORETA,l}$ is the 3-dimensional vector corresponding to the swLORETA result at voxel l given by equation (3.24) and $\hat{\mathbf{H}}$ is the operator that applies the Hilbert analysis independently to each row of the vector placed to its right. Considering that, as equations (3.20) and (3.24) point out, swLORETA can be seen as a linear operator applied to the data vector $\mathbf{d}$ comprising:

$$\hat{\mathbf{j}}_{swLORETA,l} = \mathbf{W}_l\,\mathbf{d} \qquad \text{with} \qquad \mathbf{W}_l := \left\{[\mathbf{\Sigma_j}]_l\right\}^{-1/2} \left\{\left[\mathbf{\Sigma}_{\hat{\mathbf{j}}}\right]_{ll}\right\}^{-1/2} \mathbf{T}_l$$

$\mathbf{W}_l$ is a $3 \times ns$ matrix which represents the swLORETA operator, $[\Sigma_{\mathbf{j}}]_l$ is a $3 \times 3ng$ submatrix of $\mathbf{\Sigma_j}$ corresponding to the lth voxel (equation (3.22)), $\left[\mathbf{\Sigma}_{\hat{\mathbf{j}}}\right]_{ll}$ is a 3×3 matrix given by the lth diagonal block of the matrix in equation (3.19), $\mathbf{T}_l$ is the $3 \times n_s$ submatrix of $\mathbf{T}(\alpha)$ associated with voxel l given by equation (3.15). This, together with the linearity of the Hilbert analysis given by equation (4.4), allows to re-state equation (4.5) as:

$$\mathbf{\Omega}_l = \mathbf{W}_l \left(\hat{\mathbf{H}}\,\mathbf{d}\right) \tag{4.6}$$

As in equation (4.5), this magnitude has to be computed for all voxels l in the source space. At first glance, it would appear that this reformulation is inefficient too because ns Hilbert transforms will have to be computed instead of the 3 Hilbert transforms needed in equation (4.5). This is not the case because term $\hat{\mathbf{H}}\,\mathbf{d}$ in equation (4.6) have to be computed only one time for all the l voxel in the source space (since the data term $\mathbf{d}$ is the same for all voxels) and then the result has to be multiplied by the corresponding matrix $\mathbf{W}_l$ in a loop to get the analytic signal for all voxels in brain space. Consequently, only ns (≈ 300) Hilbert transforms have to be computed. Finally, the time-varying power spectrum of the swLORETA estimates for the l voxel can be obtained from equation (4.6) as:

$$\mathbf{P}_l(w,t) = \mathrm{diag}\left(\mathbf{\Omega}_l(w,t)\,\mathbf{\Omega}_l(w,t)^T\right) \tag{4.7}$$

where T denotes the transpose complex conjugate and $\mathrm{diag}(\mathbf{M})$ is the diagonal vector formed by the diagonal elements of the matrix $\mathbf{M}$.

Under the assumption that all the EEG/MEG time series are observations from stationary stochastic processes, equation (4.7) provides the time-varying spectral context of a single realization of that process. Unfortunately, is not sufficient to represent the stochastic process. Therefore, an ensemble of N observations must be used to make a statistical estimate of the power spectrum when the unaveraged EEG/MEG is analyzed. In real EEG/MEG studies this ensemble represents different task repetitions or trials so that their time-varying spectrum can be written as:

$$\mathbf{P}_l(w,t) = \frac{1}{N}\sum_{i=1}^{N} \mathrm{diag}\left(\left\{\mathbf{\Omega}_l(w,t)\right\}_i \left\{\mathbf{\Omega}_l(w,t)^T\right\}_i\right) \tag{4.8}$$

where $\left\{\mathbf{\Omega}_l(w,t)\right\}_i$ is the analytic signal of the swLORETA estimates of the ith trial.

4.3 Analysis of Experimental Data

In this section, swLORETA properties in the time frequency domain will be illustrated using the spatial attention experiment already introduced in section (3.6). In general, the field of source localization of EEG/MEG spectral components is relatively unexplored. Consequently, there is some degree of discrepancies across studies and a working hypothesis should be considered more cautiously. Thus, spatial attention has been related with oscillations in the theta ($3.5 - 7.5$ Hz), alpha ($7.5 - 12.5$ Hz), beta 1 ($12.5 - 18.0$ Hz) beta 2 ($18.0 - 30.0$ Hz) and gamma ($30.0 - 70.0$ Hz) bands (Bland, 1986; Eckhorn et al., 1998; Basar et al., 1999; Delorme et al., 2007; Fan et al., 2007; Deiber et al., 2007, 2008). The differences between reports may be explained by the use of spatial attentional tasks which mix up control process and attentional modulation of visual inputs. Each of these elementary mental operations is likely to have different time and frequency relationships with the incoming stimuli (Deiber et al., 2007; Fan et al., 2007). In our case, we used an experimental design that decreases the demands on the attentional control system, especially working memory, while emphasizes early attentional modulations of visual inputs as well as concentrated attention on a given visual hemifield and goals maintaining. Consequently, we do not expect modulations in the gamma band (previously associated to top-down processes, working memory and feature binding) (Herrmann and Mecklinger, 2000, 2001) but in theta band. Theta oscillations have been associated to spatial attention (Deiber et al., 2008, 2007; Missonnier et al., 2006), and executive attention (Inanaga, 1998; Delorme et al., 2007). Although the physiological basis of theta oscillations are still unclear, previous noninvasive EEG/MEG studies have suggested that the brain areas involved in the generation and maintenance of theta oscillations are the hippocampus, occipital cortex, anterior cingulate cortex, mesial frontal cortex and/or dorsolateral frontal cortex.

Procedure

The characteristics of the subjects who participated in the spatial attention study as well as the methodology employed to pre-process the signal have been already described in section (3.6).

Time frequency analysis of evoked and induced scalp EEG activity

To perform this analysis a group of 12 posterior electrode sites in each hemisphere (Cp1-Cp2, Cp3-Cp4, Cp5-Cp6, Tp7-Tp8, P1-P2, P3-P4, P5-P6, P7-P8, PO3-PO4, PO5-PO6, PO7-PO8, O1-O2) was selected because they exhibited the highest ERP response (see section (3.6.1)). The time-varying power spectrum, given the analytic signal, was computed for each electrodes (see section (4.2.1)). Afterwards, the electrode that presented the highest power in each frequency band (theta: $3.5 - 7.5$ Hz, alpha: $7.5 - 12.5$ Hz; beta 1: $12.5 - 18.0$ Hz, beta 2: $18 - 30$ Hz; gamma $30 - 70$ Hz) was identified and the mean power over two time intervals ($70 - 120$ ms and $130 - 180,$ ms) was extracted for each subject, condition and band. These time intervals were chosen because, as explained in section (3.6), there is overwhelming evidence suggesting that the attention effect takes place during that time. Finally, statistical analysis was applied to determine for which frequency band there were significant differences across conditions.

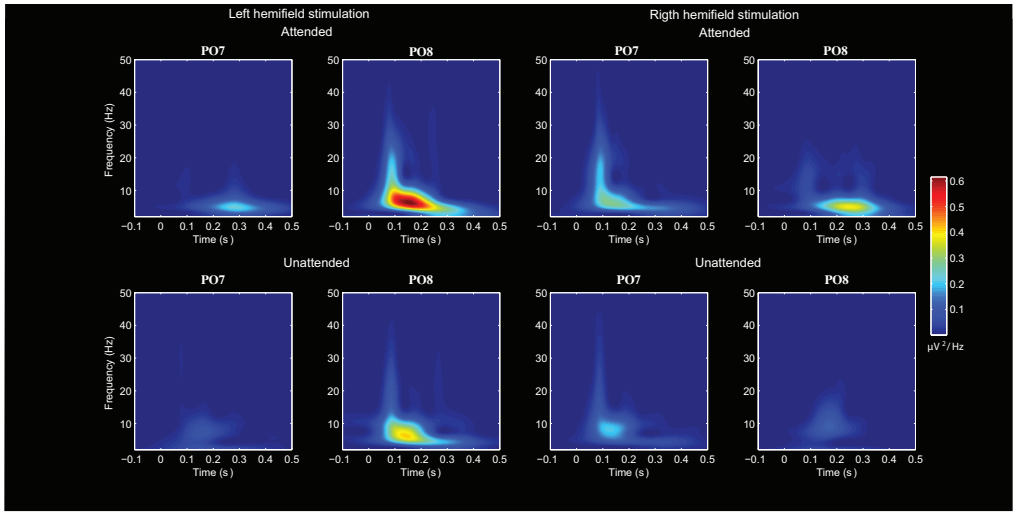

Figure 4.2: The power spectrum of the grand average of two representative electrodes (PO7 and PO8) obtained after applying the Hilbert transform.

Time-frequency source analysis

Once the frequency range of the oscillations modulated by attention was known, their brain generators were determined using equations (4.6), (4.7) and (4.8). Finally, to determine which brain regions exhibited significant differences in the power estimates across time and conditions statistical analysis was applied.

Thus, evoked and induced scalp oscillations were analyzed using Friedman ANOVA test ($p < 0.05$) and, if the test results were significant, planned comparisons were made using the Wilcoxon Matched Pairs Test ($p < 0.05$; Bonferroni corrected for multiple comparisons). In the case of the source analysis the False Discovery Rate Test (FDR) (Benjamin and Yekutieli, 2001) method was used.

4.3.1 Results

Scalp time frequency analysis

Friedman ANOVA analysis revealed that there were significant differences only in the theta power evoked by each condition between 80 and 120 ms ($Chi^2 = 26.06$; $df = 7$; $p < 0.0001$) and between 140 and 180 ms ($Chi^2 = 22.86$; $df = 7$; $p < 0.001$) (figure (4.2)) . Wilcoxon Matched Pairs Test showed that between 80 and 120 ms those differences were present only for the electrode located in the hemisphere contralateral to the stimulation (table (4.1)). Between 140 and 180 ms the differences appeared for the contralateral electrode in the case of left hemifield stimulation and in both the ipsilateral and the contralateral electrode in the case of right hemifield stimulation (table (4.2)).

Induced oscillations, on the other hand, did not present statistically significant differences between conditions (figure (4.3)). Nevertheless, as induced oscillations in some frequency range could have been associated to cognitive processes required by both conditions, the power values across bands for both conditions and brain hemispheres were compared separately. It was found that between 80 and

Evoke theta power ($\mu V^2/Hz$) between 80 and $120\,ms$				
Stimulation hemifield/ Electrodes location	Mean amplitude $\pm$ SD		Z	p-level
	Attended	Unattended		
Left/Right	0.0444 ± 0.0345	0.0257 ± 0.0208	2.75	< 0.01
Right/Left	0.0284 ± 0.0346	0.0122 ± 0.0076	2.82	< 0.01
Left/Left	0.0223 ± 0.0337	0.0099 ± 0.0073	0.94	ns
Right/Right	0.0289 ± 0.0341	0.0131 ± 0.0112	2.35	ns

Table 4.1: Results of the statistical comparisons between attended and unattended conditions for the theta power evoked from 80 to $120\,ms$. Power values evoked by the attended stimulus in a given electrode location (right or left hemisphere) were compared to the power values evoked by the unattended stimulus in a similar electrode location. (Wilcoxon Matched Pairs test, $p < 0.01$ Bonferroni corrected).

Evoke theta power ($\mu V^2/Hz$) between 140 and $180\,ms$				
Stimulation hemifield/ Electrodes location	Mean amplitude $\pm$ SD		Z	p-level
	Attended	Unattended		
Left/Right	0.0490 ± 0.0399	0.0291 ± 0.0268	2.59	< 0.01
Right/Left	0.0338 ± 0.0454	0.0132 ± 0.0864	2.75	< 0.01
Left/Left	0.0283 ± 0.0473	0.0114 ± 0.0863	1.26	ns
Right/Right	0.0362 ± 0.0444	0.0152 ± 0.0142	2.59	< 0.01

Table 4.2: Results of the statistical comparisons between attended and unattended conditions for the theta power evoked from 140 to $180\,ms$. Power values evoked by the attended stimulus in a given electrode location (right or left hemisphere) were compared to the power values evoked by the unattended stimulus in a similar electrode location. (Wilcoxon Matched Pairs test, $p < 0.01$ Bonferroni corrected).

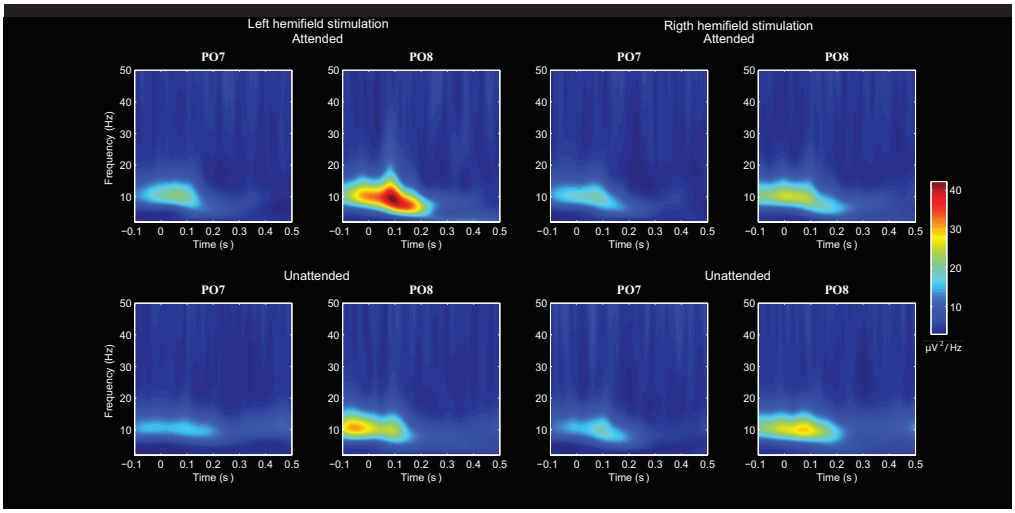

Figure 4.3: Induced power spectrum of a single subject for two representative electrodes (PO7 and PO8) obtained after applying the Hilbert transform.

120 ms there were differences in power across bands for both the attended ($Chi^2 = 166.15$; $df = 19$; $p < .00000$) and the unattended ($Chi^2 = 94.65$; $df = 19$; $p < .00000$) conditions. Similar result was found from 140 to 180 ms for the attended ($Chi^2 = 92.95$; $df = 19$; $p < .00000$) and the unattended conditions ($Chi^2 = 100.31$; $df = 19$; $p < .00000$). The highest mean was consistently found in the theta range (figure (4.4)) but Wilcoxon Matched Pairs Test demonstrated that the differences were significant only for uncorrected data. Similar results were also found for the unattended condition. Due to this finding, source analysis was also applied on induced theta oscillations.

Source Analysis

As it was done for the time domain analysis (see section (3.6)), the source localization method was applied on both the grand averaged waveform and individual data for each condition, separately. For the evoked theta oscillations it was obtained that from 80 to 120 ms there were significant differences in the activation strength of occipital (BA 17, BA 19) and middle occipital areas (BA 18) as well as in the middle temporal region (BA 37) in the hemisphere contralateral to the stimulation (figure (4.5)). From 140 to 180 ms the differences appeared not only in these areas but also in the superior temporal gyrus and in the middle temporal gyrus (figure (4.5)). Sources of the induced oscillations were placed in the bilateral middle frontal gyrus, including BA 10 and 46, and the bilateral inferior frontal gyrus. Figure (4.6) shows the resulting functional probabilistic maps (PMAP).

These maps were builded from the individual time-varying swLORETA power spectrum:

$$p_{map}(x,y,z) = \frac{1}{N}\sum_{i=1}^{N} p_i(x,y,z) \qquad \text{where} \qquad p_i(x,y,z) \;:=\; \begin{cases} 1 & \text{if } \|\mathbf{P}_i(x,yz)\| > 0.5 \cdot \|\mathbf{P}_i(\max)\| \\ 0 & \text{otherwise} \end{cases}$$

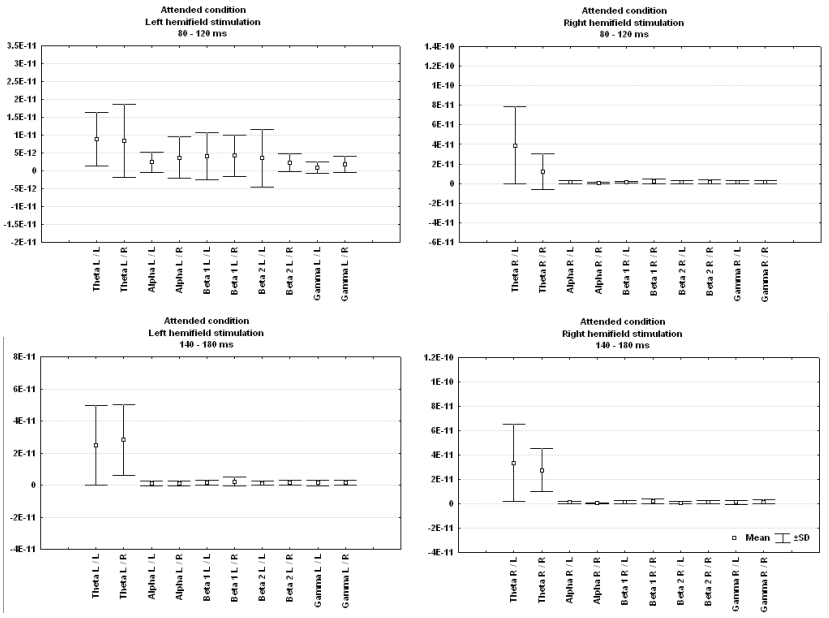

Figure 4.4: Mean and standard deviation of induced power spectrum values for the attended condition. For each value its frequency range, stimulation hemifield and electrode location are indicated. For example, "theta L / L" stands for frequency theta, Left stimulation hemifield / Left electrode hemisphere. Note how the theta mean is the highest across all stimulation hemifields. The differences were significant only for uncorrected data.

where $p_{map}(x, y, z)$ is the value of the PMAP at a given voxel with coordinates (x, y, z) and$\mathbf{P}_i(x, y, z)$ is the time-varying swLORETA power spectrum for the ith-subject at the same voxel. $\mathbf{P}_i(\max)$ is the absolute maximum value of $\mathbf{P}_i$ for the ith-subject and $p_i(x, y, z)$ represents the probability that the voxel is active with the value above the 50% of maxima.

4.3.2 Discussion

The results obtained on the scalp are in agreement with the current state of the knowledge in the field and so they validate the efficacy of swLORETA. Thus, it was obtained that evoked and induced theta oscillations are involved in spatial selective attention which is not surprising since previous studies have demonstrated that theta is involved in several tasks that imposes important demands to the attentional system. For example, in rodents theta oscillations increase when the animals are exploring the environment (moving around, sniffing and orienting) (Bland, 1986; Kahana et al., 2001) and performing spatial as well as non-spatial memory tasks (Givens, 1996; Jensen and Lisman, 2000; O'Keefe and Recce, 1993; Skaggs et al., 1996). Furthermore, it has been shown that long term potentiation is favored at the peak of the theta cycle while depotentiation is favored at its trough (Holscher et al., 1997; Huerta and Lisman, 1993). In humans, comparable results have been reported. Scalp and intracranial EEG/MEG recordings have demonstrated that theta activity raises during verbal working memory (Klimesch, 1999; Raghavachari et al., 2001), episodic memory (Klimesch, 1999), spatial n-back (Gevins et al., 1997; Krause et al., 2000), maze learning (Caplan et al., 2001; Kahana et al., 1999) and attention tasks (Deiber

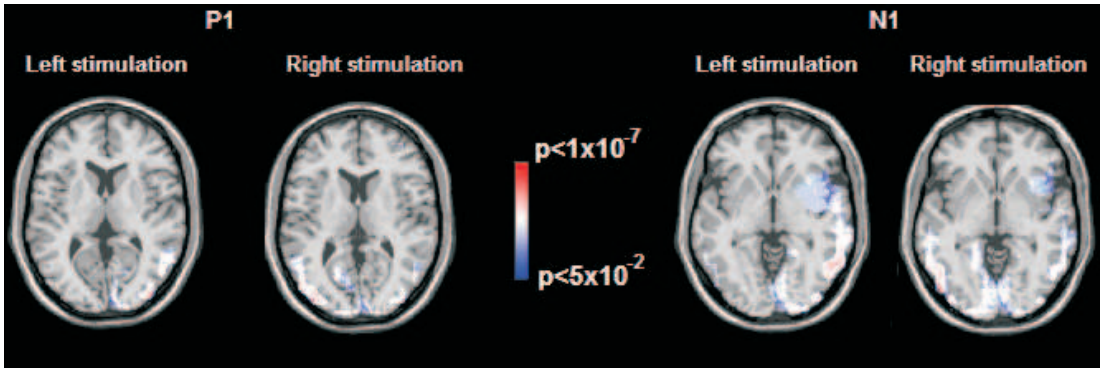

Figure 4.5: Source analysis of evoked theta oscillations. The image shows the statistical map of brain theta power values evoked by the attended condition versus the unattended condition. Only voxels that exhibit significant differences in their power spectrum values are shown. Activations are thresholded at $p < 0.05$, FDR corrected.

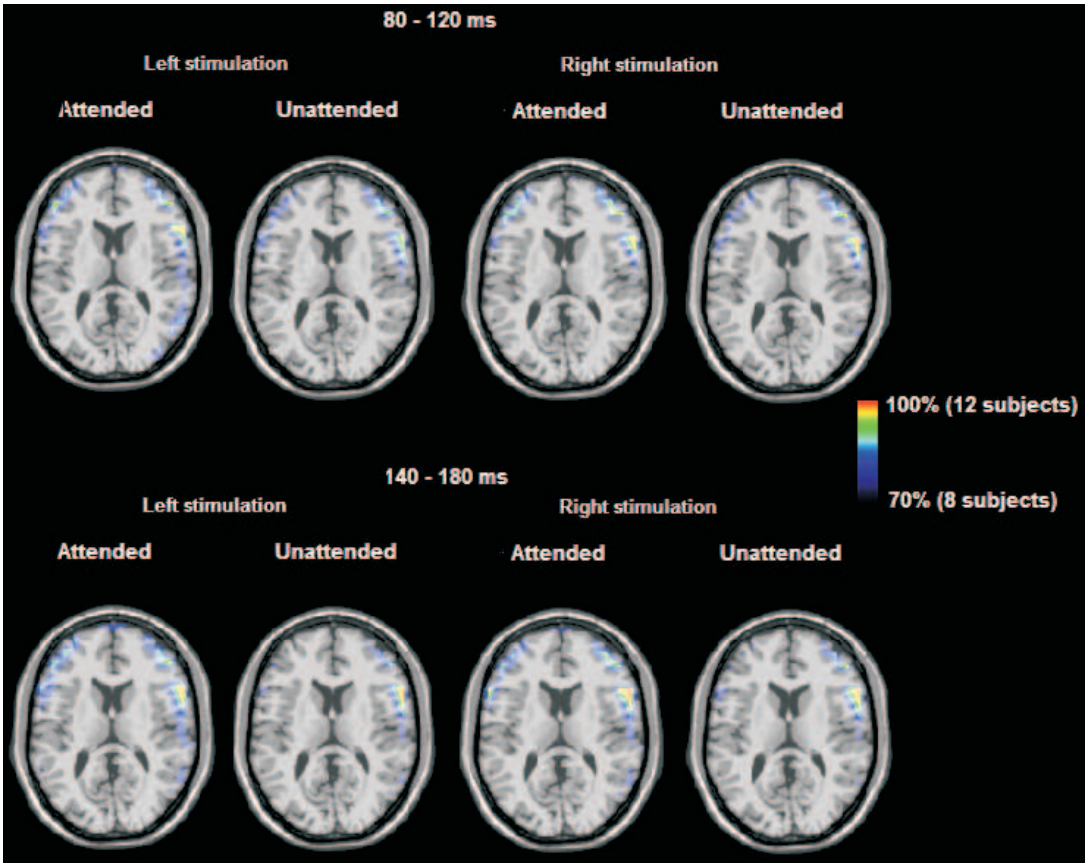

Figure 4.6: Source analysis of induced theta oscillations. The image shows the brain areas that exhibited more than 70% of the individual highest power value at each time point, during more than 10 ms and in more than 70% of subjects.

et al., 2008, 2007; Missonnier et al., 2006).

The varied cognitive content of the experiments for which theta has been found to be relevant allows thinking that this rhythm may have not a single functional role in cognition and/or that it is related to more general processes such as attention or cognitive control (Kahana et al., 2001). In line with this idea, the current results showed that theta has a multifold involvement in spatial selective attention depending on its temporal relationship with the eliciting stimuli and the functional specialization of the generating neuronal networks. This idea will be further discussed in the next two subsections. In contrast to previous reports, we found attentional modulations neither in the gamma nor in the alpha bands. Several reasons may explain this discrepancy. First, contrasting studies have suggested that gamma band may be related either to the selection and identification of relevant information (Herrmann and Mecklinger, 2000, 2001), e.g. targets, or to the miniature saccades associated to target presentation (Yuval-Greenberg et al., 2008). In either case, gamma modulations may not be evident in response to standard stimuli, which were analyzed in this study. Second, gamma oscillations may also be related to the orienting or executive components of the attentional network, as suggested previously (Fan et al., 2007). Any of these components were emphasized by our task. Last but not least, it should be mentioned that some studies have failed to find gamma synchronization or gamma oscillations at all in monkeys (Lamme and Spekreijse, 1998; Tovee and Rolls, 1992; Young et al., 1992) and humans (Juergens et al., 1999). The absence of differences in the alpha band may reflect the fact that the presentation of the standard stimuli did not modulate significantly subjects' level of arousal because they were irrelevant for a proper task performance. Future studies that include experimental conditions able to control this effect are needed to further clarify this issue.

The evoked theta oscillations were found to rise within two time ranges of the attended conditions: $80-120$ ms and $140-180$ ms. This result agrees with our own and previous studies that have shown that ERPs modulations occurs within these two intervals in spatial attention experiments (Russo et al., 2003, 2002; Hillyard and Anllo-Vento, 1998; Hopfinger et al., 2004; Martinez et al., 2007). Within both time periods evoked theta oscillations were localized within structures of the visual pathway responsible for early extraction of visual basic information and object analysis. Comparable sources were found in this and previous studies in the time domain within similar time intervals. This result provides further support for the idea that theta oscillations are involved in visual processing. They also suggests that those oscillations may be closely related to the spatial attention effect observed on the wideband P1 and N1 components (Martinez et al., 2007; Luck et al., 1996; Hillyard and Anllo-Vento, 1998).

Additional sources of theta evoked activity were found in the superior temporal gyrus and the middle temporal gyrus between 140 and 180 ms. From the physiological point of view, the temporal sources were indeed expected because previous neuroimaging studies in humans have reported increased activity in temporal regions during visual spatial attention tasks (Corbetta et al., 1998; Gitelman et al., 1999; Nobre et al., 1997). Furthermore, it has been shown that lesions to superior temporal gyrus provoke neglect in monkeys even for stimuli presented unilaterally (Lynch and McLaren, 1989; Watson et al., 1994). In humans, lesions to the middle temporal gyrus (probably extending into the temporo-occipital region) has also been linked to extinction and other components of contralesional neglect (Bisiach et al.,

1981; Friedrich et al., 1998). Unfortunately, it is still not clear whether these temporal regions are linked to attention-related visual processing of the stimuli or the cue. It has been previously reported that only the attention-directing cues are able to modulate the activity in the superior temporal sulcus, anterior to the temporal-parietal junction (Hopfinger et al., 2000). Therefore, it has been suggested that this region is involved in attentional control circuitry but not in attention-related processing of relevant target stimuli (Hopfinger et al., 2000). In the paradigm used here the relevant cue remained on the screen during the presentation of the stimuli and, thus, it cannot be differentiated between cue and stimuli processing. Further research is needed to give a more precise answer to this issue.

The analysis of induced activity presented a different pattern of results. They were not modulated by attention but were present in both experimental conditions and were not associated to the activation of visual occipital and temporal areas but frontal regions. This outcome may suggest that they are associated to general processes required for a good performance in spatial attention paradigms. Considering that the current experimental design emphasized concentrated attention on a given visual hemifield, goals maintaining, stimulus judgment and decision making it is possible to think that these were the functions supported by the induced oscillations. The brain areas found to be the sources of these induced theta oscillations (bilateral middle frontal gyrus, including BA 10 and 46, and the bilateral inferior frontal gyrus) bring further support for this idea. These regions have usually been related to executive control (Alvarez and Emory, 2006; Jurado and Rosselli, 2007). Furthermore, iEEG studies in humans and monkeys have reported the existence of similar frontal theta activation during problem solving (Inanaga, 1998), continuous mental activity and preparation for rapid motor responses (Delorme et al., 2007). Thus, it has been related to concentrated performance of mental tasks and top down processes.

4.4 Conclusions

In this chapter, swLORETA was extended to the time-frequency domain by applying the Hilbert transform to the time series obtained with the swLORETA inverse solution method. The resulting algorithm is not only efficient but also accurate as demonstrated by the analysis of a spatial attention experiment. In line with previous studies, the obtained results suggest that allocating attention to a specific location in the visual field enhances both evoked and induced theta activity. While visual analysis of the stimuli is associated to evoke oscillations in striate, extrastriate and temporal regions; executive functions are linked to induced theta oscillations generated in frontal areas. It is worth mentioning that our extension, as can be seem from the results section, can be applied to the analysis of both evoked and induced EEG/MEG activity.

5

Functional Connectivity

> All great progress takes place when two sciences come together, and when their resemblance proclaims itself, despite the apparent disparity of their substance.
>
> Henri Poincare

5.1 Introduction

Coherent cognitive life strongly depends on the connections between different and sometimes distant brain regions (Varela et al., 2001; David O., 2002; Weiss and Mueller, 2003). For example, visual processing in primates is characterized by two major functionally segregated and hierarchically organized pathways: a ventral stream, which includes areas V1, V2, V4, as well as further stations in inferior temporal cortex; and a dorsal stream, which includes areas V1, V2, V3, MT/V5, and further stations in posterior parietal areas (Zeki, 1978; Ungerleider and Desimone, 1986; Young, 1992). Although their functional segregation is not strict, lesion studies in monkeys and humans have shown that the dorsal stream favors the analysis of information concerned with motion, low visual contrast, and lower spatial frequency while the ventral stream favors the analysis of information concerned with color and shape (Ungerleider and Desimone, 1986; Young, 1992). However, in our daily vision, objects need to be processed based on, for example, motion and shape cues. How are these different attributes, which are analyzed by each stream; integrated into a unified, coherent perception? During the last years, the problem of information binding or integration has received some attention as it poses one of the most fascinating and fundamental problems in Neuroscience. It has been proposed that the relatedness of neurons that code different features is supported by the formation of transient oscillatory assemblies or functional systems (Singer, 1989; Varela et al., 2001).

Two main methods have been developed to determine this functional relatedness between brain areas: coherence and phase synchronization. Usually, those methods are applied on the scalp level

which can introduce serious pitfalls. This is due to the fact that, as explained in previous sections, at the scalp level the signal registered by each detector is a mixture of the activity produced by several areas. As the inverse methods try to resolve this mixture performing coherence or phase synchronization analysis at the level of the sources should yield to more accurately results and even more important for the inverse methodology, to a better estimation of active areas. For all these reasons, the present chapter will illustrate how to combine the swLORETA algorithm and the Hilbert transform described in chapters (3) and (4) with the phase synchronization (Tass, 1995, 1999, 2004) and coherence index to measure, non-invasively the amount of functional connectivity.

This chapter introduces the coherence (5.2.1) and phase synchronization measures (section (5.2.2)) for the bivariate case. In sections (5.2.3) and (5.2.4) the coherence and phase synchronization imaging methods will be introduced. Finally, sections (5.3.2) and (5.4) will be devoted to assess the accuracy of the proposed method with simulated and real data.

5.2 Functional Connectivity Image Based on swLORETA

5.2.1 Coherence

In neuroscience research, the coherence between two time series that correspond to two different spatial sensors locations is interpreted as a measure of the functional connectivity between these two locations (Singer, 1989; Eckhorn et al., 1998; Gross et al., 2001; Pohja et al., 2005). The coherence function between the pair of signal $x(t)$ and $y(t)$ as a function of frequency w is defined as:

$$C(w) = \frac{|F_{xy}(w)|}{\sqrt{F_{xx}(w)F_{yy}(w)}} \tag{5.1}$$

where $F_{xx}(w)$, $F_{yy}(w)$ and $F_{xy}(w)$ are the power spectra and the cross spectrum of $x(t)$ and $y(t)$ given by:

$$\begin{aligned} F_{xx}(w) &= \left\langle X(w)X(w)^T \right\rangle \\ F_{yy}(w) &= \left\langle Y(w)Y(w)^T \right\rangle \\ F_{xy}(w) &= \left\langle Y(w)X(w)^T \right\rangle \end{aligned}$$

where $X(w)$, $Y(w)$ are the Fourier transforms of the two signals $x(t)$, $y(t)$ and X^T indicates the complex conjugate of X. In this way, it is obtained a frequency function that can only take values between 0 and 1, where 0 indicates no linear correlation between the signals and 1 indicates that the two signals are completely correlated.

When narrow-band signals are analyzed, the coherence function is only meaningful in the narrow range where there is significant power. Outside this region, it has no sense to talk about the signals being correlated (since there is essentially no signal there), and numerically, the estimation of the coherence function ends up being the ratio of two very small numbers, which typically ends up giving non-meaningful values from the entire range 0 to 1. As a result, the coherence at the peak frequency

(Eckhorn et al., 1998; Gross et al., 2001)is usually taken.

Here, a slightly more robust approach is proposed. It is based on the creation of a weighted average of the coherence function over the entire frequency range that is weighted by the amount of power in the signals at each frequency. In effect, the coherence function is just a normalization of the cross-spectrum, so this new approach can be thought of as an alternative normalization that reduces the measure to a single coherence index, defined as:

$$C'(x(t), y(t)) = \Gamma \sum_{w} C(w) \sqrt{F_{xx}(w) F_{yy}(w)} \tag{5.2}$$

where $C(w)$ is the standard coherence function, and $\Gamma = 1/\left(\sum_w \sqrt{F_{xx}(w)F_{yy}(w)}\right)$ is the normalization factor, which is equal to the value that the weighted sum above would obtain for 100% coherence. This is equivalent to

$$C'(x(t), y(t)) = \frac{\sum_w |F_{xy}(w)|}{\sum_w \sqrt{F_{xx}(w)F_{yy}(w)}}$$

This average provides a single positive value in the range between 0 and 1, which represents the weighted average of the cross spectrum over all frequencies. In this way, $C'(x(t), y(t)) = 1$ represents a perfect linear relation between signals $x(t)$ and $y(t)$. On the contrary, $C'(x(t), x(t)) = 0$ means no linear relation between the two given signals. The advantage of this measure over the standard procedure of choosing the value of the coherence function at the peak is two-fold. First, it eliminates the need to statistically identify exactly where the peak is and second, the value obtained will be less sensitive to statistical analysis because it is an average over many frequency bins. From this point forward the ' will be omitted and instead will be used $C(x, y)$ to denote the coherence index between x and y given by equation (5.2).

5.2.2 Phase Synchronization

The notion of synchronization was introduced by the Dutch scientist Christiaan Huygens back in the 17th century. In its classical form, phase synchronization is usually defined as a locking of the phase of the two oscillators $x(t)$ and $y(t)$:

$$\varphi_{x,y}^{n,m}(t) = m\,\psi_x(t) - n\,\psi_y(t) = \chi \tag{5.3}$$

where $\psi_x(t)$, $\psi_y(t)$ is the instantaneous phase, t is time, χ is a constant, and n, m are integers that indicate the ratios of possible frequency locking. This equality can be disturbed by dynamical noise or by chaos, both can be conceptually considered in the framework of stochastic dynamics. In the case of small and bounded noise the stable phase dynamics is only slightly perturbed. Thus, the relative phase $\varphi_{x,y}^{n,m}(t)$ mainly fluctuates around some constant level and consequently, the phase locking condition can be rewritten as:

$$\left|\varphi_{x.y}^{n,m}(t)\right| = |m\,\psi_x(t) - n\,\psi_y(t)| < \chi \tag{5.4}$$

In the case of unbounded noise, i.e data acquisition noise inherent to the EEG/MEG signals, these nearly stationary fluctuations may be interrupted by phase slips, where the relative phase $\varphi_{x,y}^{n,m}(t)$ changes relatively rapidly (by $\pm 2\pi$). Thus, strictly speaking, the phase difference is unbounded and condition (5.4) is not valid anymore. Nevertheless, it has been demonstrated that the distribution of the *normalized cyclic* $n : m$ *phase difference*

$$\Psi_{x,y}^{n,m}(t) = \frac{m\,\psi_x(t) - n\,\psi_y(t)}{2\pi} \bmod 1$$

has one or more dominating peaks (Rosenblum and Pikovsky, 2003). The presence of these peaks can be understood as the phase locking in a statistical sense. In this context, the *normalized cyclic* $n : m$ *phase difference* can be considered as a random variable characterized by a probability distribution. Here, this probability distribution is empirically accessible in the form of a number of realizations of $\Psi_{x,y}^{n,m}(t)$ in the time interval $t \in [t_a, t_b]$. There, in order to characterize the deviation of the *normalized cyclic* $n : m$ *phase difference* from the uniform distribution a synchronization index based on *Shannon entropy* will be used(Tass, 1999). This index is defined as:

$$\rho_{m,n}(x(t), y(t)) = \left[S_{\max} - S(t)\right] / S_{\max} \tag{5.5}$$

where $S(t) = -\sum_{k=1}^{N} p_k \ln p_k$ is the entropy of the actual distribution of $\Psi_{x,y}^{n,m}(t)$,

$$N = \exp(0.626 + 0.41 \log(M - 1))$$

is the optimal number of bins for a distribution of M points (Otnes and Enochson, 1972; Tass, 1999), p_k is the frequency of finding $\Psi_{x,y}^{n,m}(t)$ in the kth bin, and $S_{\max}$ is the entropy of the uniform distribution given by $S_{\max} = \ln N$. $\rho_{m,n} = 1$ represents a perfect phase synchronization (Dirac distribution) and $\rho_{m,n} = 0$ represents a uniform distribution of the *normalized cyclic* $n : m$ *phase difference*. Alternatively, instead of the Shannon-entropy-based index, one can also use the Kuiper test. This tests is a modified version of the Kolmogorov-Smirnov test, which is invariant under changes to the arbitrary choice of zero phase. This provides the probability with which a given distribution can be considered to be uniform (Tass, 2004). The advantages of the entropy index is that, in contrast to other kind of phase synchronization measures like phase coherence (Lachaux et al., 1999; Hurtado et al., 2004), it does not assume an unimodal distribution for the *normalized cyclic* $n : m$ *phase difference.*

5.2.3 Principle of Coherence Imaging

In section (5.2.1) the concept of coherence as a measure of functional coupling was reviewed. Several studies have used the coherence index between sensors covering different scalp areas as a correlate of oscillatory coupling between brain regions. However, as it was shown in chapter (2), this approach is limited because of the complex relation between the PCD and the EEG/MEG signal recorded over the scalp. In this section, a method to estimate coherence between different brain areas and between a brain and an external signal will be introduced. This last case will be considered because it is relevant for

research in the field of, for example, Parkinson patients (Gross et al., 2001). In these type of studies, the tremor generation is studied by determining the coupling between the electromiogram (EMG) and a brain region. When the EMG-to-brain case is considered, the fact that the estimated signal at each brain location is a vector with three components has to be solved. To this end, an extension of the weighted coherence function (equation (5.2)) that produces a single index for all three components will be used. This weighted coherence function between a scalar signal $s(t)$ and a three dimensional vector $\mathbf{j}(\mathbf{r},t)$ is defined as follows:

$$C(s(t),\mathbf{j}(\mathbf{r},t)) = \max_{i=1}^{3} \{C\left(s(t),\mathbf{j}_i(\mathbf{r},t)\right)\} \tag{5.6}$$

where $s(t)$ is the reference signal, $\mathbf{j}(\mathbf{r},t)$ is the PCD at location $\mathbf{r}$, and $\mathbf{j}_i(\mathbf{r},t)$ is the ith component of $\mathbf{j}(\mathbf{r},t)$.

When the brain-to-brain case is considered, a similar problem has to be solved but in contrast to equation (5.6) here both signals are vectors and, thus, an extension to equation (5.6) has to be made as follows:

$$C(\mathbf{s}(\mathbf{r}',t),\mathbf{j}(\mathbf{r},t)) = \max_{i=1}^{3} \left\{C\left(\mathbf{s}_i(\mathbf{r}',t),\mathbf{j}(\mathbf{r},t)\right)\right\} \tag{5.7}$$

where $\mathbf{s}(\mathbf{r}',t)$ and $\mathbf{j}(\mathbf{r},t)$ are the PCD at voxel $\mathbf{r}'$ and $\mathbf{r}$ respectively, $\mathbf{s}_i(\mathbf{r}',t)$ is the component of $\mathbf{s}(\mathbf{r}',t)$ and $C\left(\mathbf{s}_i(\mathbf{r}',t),\mathbf{j}(\mathbf{r},t)\right)$ is the coherence between a scalar and 3-dimensional vector given by equation (5.6). In principle, with equation (5.7) it is possible to compute the coherence between all possible voxel combinations in brain space but it will be computational expensive. It is more efficient to identify first one brain region involved in the response of interest. This can be achieved for example by selecting the voxel which shows the maximum power spectrum during the time and frequency of interest (see section (4.2.2) for more details) and use it as the reference signal $\mathbf{s}(\mathbf{r}',t)$ for the computation of the coherence index with all other voxels in the source space. Another criteria can be to use prior information given by fMRI or PET. In this case the voxel with the highest response can be selected and used as the reference signal $\mathbf{s}(\mathbf{r}',t)$.

The maximum value over the three components in equations (5.6) and (5.7) was chosen instead of an average or modulus of the three components because the maximum is more robust with respect to rotations of the coordinate system. For example, consider two highly coherent signals: $S1$, which is the external one and $S2$, which is placed along the x axis. Then, add a small amount of noise to all three axes, so that the x axis, primarily the signal $S2$, is stronger than the y or z components. Additionally, place the same signal $S2$ halfway between the x and y axis. In this second case, both x and y are primarily the signal $S2$. In these two cases, the mean coherence over all three axes will be very different and it will be much higher for the second case. The maximum coherence over all three axes, however, will be much more stable under such rotations because the rotation above mentioned will only slightly reduce the coherence between s and x.

To avoid spurious detection of coherence, surrogates are prepared by replacing $s(t)$ and $j_k(\mathbf{r},t)$ with surrogate signals $\bar{s}(t)$ and $\bar{j}_k(\mathbf{r},t)$. The surrogate signals are generated using the DFS (Digitally

Filtered Surrogate) method (Dolan and Spano, 2001). This produces surrogate data which have the same power spectra as the original signals and are, in all respects, linear stochastic processes. This means that any and all correlations between $s(t)$ and $j_k(\mathbf{r},t)$ are eliminated from the surrogate data. Any degree of coherence between the surrogate signals is therefore due only to statistical fluctuations. Of course, the range of values that the coherence index will take for such uncorrelated signals will depend on factors such as the power spectra of the signals and the length of the data sets. These surrogates, thus, allow setting up a confidence level for what constitutes a value of C statistically different from zero. A population of 300 surrogate data sets were generated, and the coherence index was calculated for each set. The 99th percentile of the distribution of surrogate coherence indexes then serves as a baseline for the coherence analysis, and is subtracted from equation (5.6):

$$C(s(t),\mathbf{j}(\mathbf{r},t)) = \max_{i}^{3}\{\max\{C\left(s(t),\mathbf{j}_i(\mathbf{r},t)\right) - C^a,\,0\}\} \tag{5.8}$$

where C^a is the above mentioned 99th percentile of the coherence index distribution for the surrogate signals $\bar{s}(t)$ and $\bar{\mathbf{j}}(\mathbf{r},t)$. In a similar way, it is defined the 99th percentile for the coherence function presented in equation (5.7).

5.2.4 Principle of Phase Synchronization Imaging

As in section (5.2.3), a generalization of the synchronization index (Tass et al., 2003) is used to take into account the synchronization between a scalar signal, $s(t)$, and a three dimensional vector $\mathbf{j}(\mathbf{r},t)$:

$$\rho_{m,n}(s(t),\mathbf{j}(\mathbf{r},t)) = \max_{i}^{3}\{\rho_{m,n}\left(s(t),\mathbf{j}_i(\mathbf{r},t)\right)\}. \tag{5.9}$$

where j_i is the ith component of $\mathbf{j}$. The signal $s(t)$ represents an external signal such as an EMG measurement or sensory stimulus. The synchronization between two three dimensional vector $\mathbf{s}(\mathbf{r}',t)$ and $\mathbf{j}(\mathbf{r},t)$, is defined as:

$$\rho_{m,n}(\mathbf{s}(\mathbf{r}',t),\mathbf{j}(\mathbf{r},t)) = \max_{i=1}^{3}\left\{\rho_{m,n}\left(\mathbf{s}_i(\mathbf{r}',t),\mathbf{j}(\mathbf{r},t)\right)\right\}$$

To avoid a spurious detection of synchronization, a baseline correction is again introduced by means of surrogate analysis. As mentioned above, the null-hypothesis is no longer that there is no correlation between the signals at all (that issue has already been resolved using the coherence tomography analysis) but that the signals can be modelled as interacting linear stochastic processes. This indeed, is a more specific null-hypothesis. For this purpose, surrogates that preserve both the power-spectra of the original signals, as well as any linear correlations between them are needed. This is accomplished using the CDFS (Coherent Digitally Filtered Surrogate) method (Dolan and Neiman, 2002; Dolan, 2004). This method generates pairs of surrogate signals for which the power spectra of the original signals are preserved and the coherence function of each pair is the same as for the original signals. Because it is desirable to test against the null-hypothesis of any sort of linear correlations, the version of this method described in (Dolan, 2004), which preserves not only the coherence function but also the phases of the

cross-spectrum, is used here. Again, 300 surrogate realizations are used. The synchronization index is calculated in each case, and the 99th percentile of the resulting distribution of values is used as a baseline.

$$\rho_{m,n}(s(t), \mathbf{j}(\mathbf{r},t)) = \max_{i}^{3}\{\max\{\rho_{m,n}\left(s(t), \mathbf{j}_i(\mathbf{r},t)\right) - \rho^a_{m,n},\, 0\}\}. \tag{5.10}$$

5.3 Analysis of Simulated Data

5.3.1 Description of the Simulations

In this section the results of a study carried out to test the tomographic properties of the phase synchronization and coherence image will be presented. This study was performed using simulated data. Although the phase synchronization image was formulated for the general $n : m$ case, for these simulations it was limited to the $n = m = 1$ case. The ongoing cerebral activity was simulated by using one of the two coupled phase oscillators as the time course of a current dipole at location $\mathbf{r_0}$. A phase oscillator is an oscillator with constant amplitude and it serves as a generic model that approximates various types of oscillators in physics and biology (Kuramoto, 1984; Winfree, 2001; Tass, 1999). The oscillators were simulated using the Kuramoto model (Kuramoto, 1984):

$$\dot{\psi}_i = w_i + \frac{\Gamma}{2}\sin(\psi_j - \psi_i) \qquad i = 1,2 \qquad i \neq j \tag{5.11}$$

where ψ_i are phase variables, w_i are the natural frequencies of the oscillators, and Γ is the coupling strength. This model represents the phase dynamics of an oscillator with time course $x_i(t) = A_i\cos(\psi_i(t))$, where A_i represents the amplitude of the oscillator. The time course of our simulated dipole is $x_i(t) = \cos(\psi_i(t))$ with constant amplitude $A_i = 1$. Additionally, $w_1 = 1.0$, $w_2 = 1.0$, and $\Gamma = 3.0$.

The magnetic flux for each time was computed and Gaussian white noise was added to the signals after the forward solution. In this case, statistically independent white noise signals was added to each detector. Each of these noise signals is mean zero, with standard deviation given by the desired signal-to-noise-ratio. To deal effectively with time-varying dipoles the SNR definition was re-defined as follows. First, the detector with the maximal signal strength over time was selected. That means that it was the detector for which the standard deviation of the magnetic flux over time was maximal. The standard deviation of this signal was then divided by the standard deviation of the noise to get the SNR. Note that the noise strength was the same for all detectors, so those detectors which, in the absence of noise, measured very weak magnetic fluxes consisted primarily of noise. This random noise was intended to represent the measurement noise of the detectors. Other potential sources of noise, which had to be modelled as signals that could be correlated between detectors, were not considered. Figure (5.1) shows the signals for each MEG detector with a SNR = 6 for the most superficial dipole.

Afterwards, the swLORETA method was used to compute the PCD. The coherence and synchronization indexes between the original phase oscillator and the estimated PCD for all voxels in the source

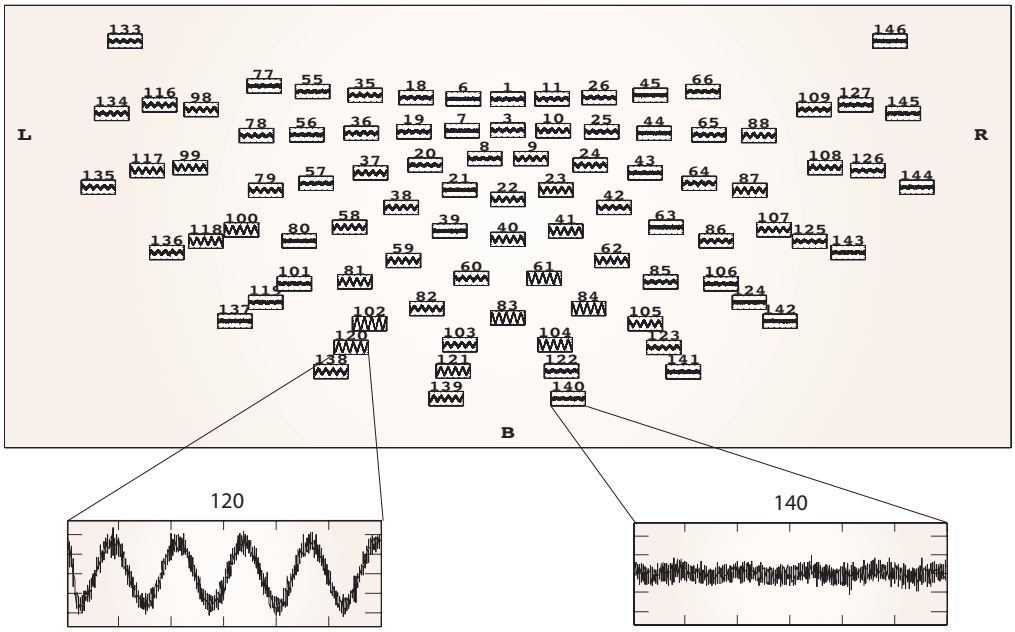

Figure 5.1: Time courses of the simulated MEG signal. Each rectangle corresponds to an MEG sensor. In this case, a white noise with a SNR = 6 was added to the original signals. Channel 120 represents the detector with the maximum signal strength over time.

space were obtained by means of equations (5.8) and (5.10), respectively. In these simulations, the positions of the simulated dipoles were the same as those of the dipoles described in subsection (3.5.3). For each dipole position, the y and z orientations were considered and the results for both orientations were averaged. In order to estimate the mean and the standard error, 300 noise realizations were used for each dipole position and direction.

5.3.2 Results

Results are presented in figures (5.2) and (5.3). These figures point out the dependency of the localization error and activity volume on the eccentricity for both methods. swLORETA synchronization tomography showed a very small localization error for all eccentricity values. In contrast, although the localization error of swLORETA coherence tomography decreased while the eccentricity increased, it is only comparable with the swLORETA synchronization tomography for eccentricity values higher than 90%. Additionally, both the localization error and the activation volume of swLORETA synchronization tomography were smaller than the localization error and the activation volume of swLORETA (data not shown here).

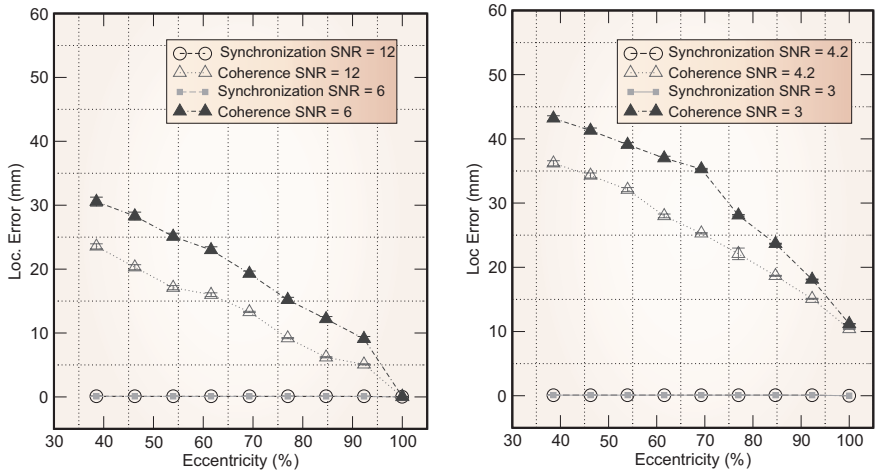

Figure 5.2: Localization error of swLORETA synchronization and swLORETA coherence tomography.

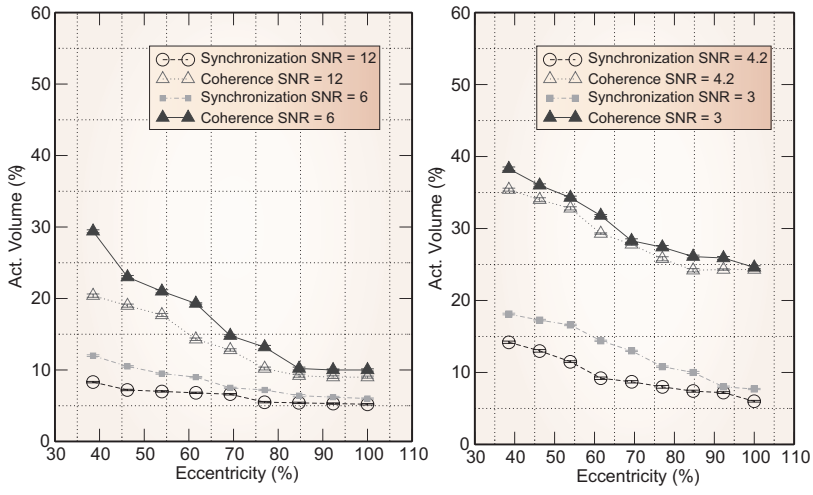

Figure 5.3: Activation volume of swLORETA synchronization and swLORETA coherence tomography.

5.4 Phantom Experiment

5.4.1 Description of the Experiment

This section focuses on a second study performed to test the previously presented algorithms. This time, the data was generated using a phantom, a composite fiber glass sphere of $8\,\mathrm{cm}$ diameter figure (5.4) and recorded by means of 140 magnetometers of the 4D Neuroimaging MAGNES 2500 WH system (see section (3.5.1) for details). The advantage of this type of studies is that the dipoles placed inside the phantom are well characterized in term of their position and strength. Consequently, the localization error of a given inverse method can be objectively tested. The phantom was fitted to the helmet portion of the sensors array and contained 5 dipoles withs known fixed positions and tangential orientations. The distance between adjacent dipoles was $1\,\mathrm{cm}$. The phantom was also filled with saline solution to allow the current to flow when energizing a dipole and produce a changing magnetic field. Each dipole was constructed by a twisted pair of fine wires running along the inside of the fibreglass rod at the outside of the sphere with opposite ends separated by $0.5\,\mathrm{cm}$. These wires were connected to a switch box and a function generator outside the MEG shielded room. The function generator provided a variety of waveforms, including sine-waves, square-waves and other standard waveforms. The amplitude and frequency of this waveforms was adjusted manually.

Each dipole was energized independently with a $10\,\mathrm{Hz}$ sinusoidal waveform during $30\,\mathrm{s}$ at a sample rate of $1000\,\mathrm{Hz}$. In this way, 5 different MEG data sets were generated. Afterwards, they were band pass filtered between $0.1\,\mathrm{Hz}$ and $20\,\mathrm{Hz}$. Data previously collected in the same system from a resting human subject, was also added to achieve a typical SNR. Finally, the original $10\,\mathrm{Hz}$ sinusoidal waveform was used as the external signal in equations (5.10) and (5.8). The PCD was obtained by using a 3D grid fitted to the top semi-sphere of the phantom. A total of $17 \times 17 \times 9 = 2601$ points were used with a minimum distance of $8.7\,\mathrm{mm}$ in the x-axis and y-axis and $7.8\,\mathrm{mm}$ in z axis. The coordinate system used was already explained in section (3.5.1). Only the 1156 voxels lying inside the phantom were finally used as source space. During the simulation, the phantom's dipoles pointed to the surface of the skull in the z-axis.

Because the position of the current dipoles inside the phantom were known they were used to estimate the localization error of the inverse methods considered here. The localization error was defined as the Euclidean distance between the maximum of the synchronization index (or coherence index) distribution and the real position of the current dipole inside the phantom and is shown in figure (5.5).

5.4.2 Results

The localization error is shown in figure (5.5). As in previous simulations, the localization error exhibited a general decrease while the eccentricity exhibited an increase for both the synchronization and coherence tomographies. This was true despite the fact that the "real" MEG signal was embedded in a more "realistic" noise environment (e.g. the typical background noise present in the MEG shielded room, subject's heart beat and respiration). This noise can have a much more complicated structure than the Gaussian white noise used in all previous simulations and so it is closer to real experimental

Figure 5.4: The phantom before the measurement in the MEG system. Reference coils are fixed to the *head* of the phantom in order to measure the positions of the MEG sensors relative to the head.

conditions.

Figure (5.5) also shows the localization error for the swLORETA. In this case since there were $30\,\mathrm{s}$ of data 30000 possible reconstructed images (one for each time sample) existed. Consequently, in order to compare the performance of the swLORETA with the synchronization and coherence tomography, its localization error was defined as the minimum error over the set of 30000 possible realizations. The localization error for a given realization was taken again as the Euclidean distance between the maximum of the PCD and the position of the current dipole inside the phantom for the realization under analysis. As in previous analysis, the swLORETA localization error decreased with the increase of the eccentricity and had a maximum of $20\,\mathrm{mm}$ for the deepest dipole. When all 3 methods are considered it can be that the swLORETA synchronization tomography performed better for all the tested conditions.

5.4.3 Discussion and Conclusions

In this section, it was demonstrated that a further improvement of the swLORETA source localization algorithm can be attained by incorporating additional information about the reciprocal functional interactions established between different brain regions during mental tasks. It was empirically demonstrated that both swLORETA synchronization tomography and swLORETA coherence tomography were superior to swLORETA. This can be explained but the fact that inverse methods do not estimate the dipoles strenght accurate but, in contrast, preserve its temporal dynamics. Because swLORETA coherence and in particular swLORETA phase synchronization tomography use this information a more robust localization of the underlaying sources is attained.

Additionally, it was seen that swLORETA synchronization tomography performs better than the coherence based tomography. This result is explained by the fact that the synchronization analysis specifically detects the adjustment of the oscillators phases, thereby taking into account linear and nonlinear features of the signals (Tass et al., 1998; Rosenblum et al., 2001). In contrast, standard coherence

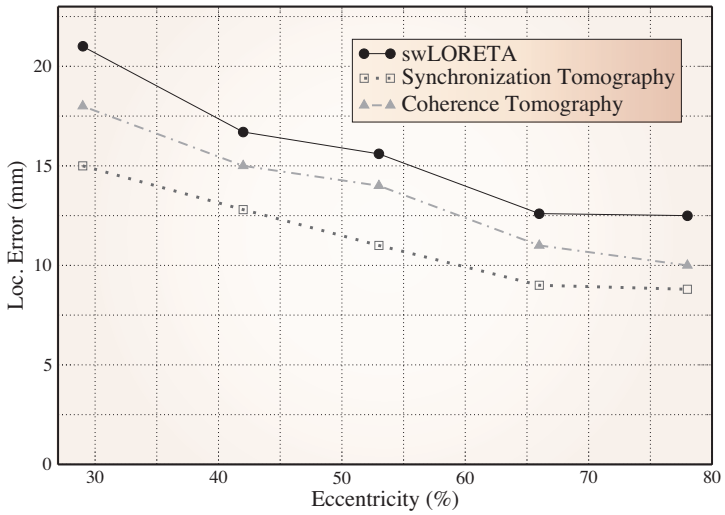

Figure 5.5: Localization error of swLORETA, swLORETA synchronization and swLORETA coherence tomography methods, using a simulated phantom experiment. The different eccentricity values correspond to 5 dipoles with fixed positions and tangential orientations. A 10 Hz sinusoidal waveform lasting 30 s was used to generate the MEG signals.

analysis detects only linear correlations between the signals. This is very important because as MEG and EEG signals are mixtures, i.e. superpositions of magnetic or electrical fields originating from different cerebral sources, coherence cannot distinguish between real phase locking and two mixed signals mutually containing parts of the other (Tass et al., 1998; Rosenblum et al., 2001). Accordingly, when applied to EEG/MEG signals, standard linear coherence leads to a spatial over-estimation of synchronization processes as compared to phase synchronization analysis (Rosenblum et al., 2001). As seen here, this limitation also applies to PCD analysis.

6

Conclusions and outlook

Art is never finished, only abandoned.

Leonardo da Vinci

Several decades have passed since the first attempts to find the underlying sources of the EEG/MEG signals. Despite the amount of research devoted to this problem and the developments achieved, the search for better inverse solution methods continues. Two main reasons keep alive this enterprise: the complicated physics nature of the inverse problem and the appearance of new challenges posed by the advancements in EEG/MEG technology. Think, for example, the contribution that an accurate inverse method could make to the brain computer interface technique. This technique aims to guide in real time an external device according to the subject's ongoing brain activity recorded on the scalp. It goes without saying that the identification of the anatomical structure active at a given time can be a trustable indicator of what the subject which to do with the external device (Lebedev and Nicolelis, 2006).

In this thesis, a new inverse method named swLORETA has been presented. This method, which is a generalization of sLORETA, uses a singular value decomposition based lead field weighting to compensate the tendency of the linear inverse procedures in general, to reconstruct the sources close to the location of the sensors and to decrease the sensitivity of the solution to the presence of noise in the data. It was shown that the new technique improved the tomographic properties of the sLORETA and hence the MN under all simulated condition. Moreover, when the algorithm was tested under a real experimental situation it was able to reconstruct the underlying sources in accordance with previous studies.

Although this was a good step forward, it does not fully exploit the whole range of valuable information contained in the EEG. As neurons oscillates at different frequencies over time it is also important to study the brain regions activated in the time-frequency space. Consequently, swLORETA was extended by combining the time series it provides with the Hilbert transform.

Information about the brain functional connectivity pattern established during a given cognitive task was also computed using the swLORETA algorithm. To this end two indexes were employed: phase synchronization and coherence. It was demonstrated that taking into account the dynamics of the signal

improved the identification of the different members of the neuronal network especially when the phase synchronization index was used.

Finally, using the linear properties of swLORETA in combination with the time-frequency decomposition it was possible to optimize the algorithm to allow its use in real time. Thus, the amount of computations were decreased from ≈ 3000 (typical number of points in the source space) to ≈ 300 (number of sensors).

Several lines of development are still waiting ahead. For example, the information derived from other imaging techniques like fMRI or PET measures can be also used to further improve the performance of swLORETA. Additionally, anatomical connectivity information can be obtained using diffusion tensor image procedure (Behrens et al., 2003; Kaden et al., 2008). This information could be used in addition to the phase synchronization tomography method developed in chapter (5) to take into account not only the functional links established between regions but also their actual anatomical connections.

A

Tikhonov regularization

The minimization ansatz, in finding a unique solution by a trade off between fidelity to the data and fulfillment to the model, is widely used Tikhonov regularization. The degree of the trade off is tuned via the regularization parameter α. For the minimum it follows:

$$
\begin{aligned}
\frac{\partial}{\partial \mathbf{j}_i}\left(\beta \mathbf{j}^T\mathbf{j} + \lambda\left(\mathbf{d}-\mathbf{K}\mathbf{j}\right)^T\left(\mathbf{d}-\mathbf{K}\mathbf{j}\right)\right) &= 0 \\
\frac{\partial}{\partial \mathbf{j}_i}\left(\beta \mathbf{j}^T\mathbf{j} + \lambda\mathbf{d}^T\mathbf{d} - \lambda\mathbf{j}^T\mathbf{K}^T\mathbf{d} - \lambda\mathbf{d}^T\mathbf{K}\mathbf{j} + \lambda\mathbf{j}^T\mathbf{K}^T\mathbf{K}\mathbf{j}\right) &= 0 \\
\beta\frac{\partial}{\partial \mathbf{j}_i}\left(\sum_{k=1}^{3n_g}\mathbf{j}_k\mathbf{j}_k\right) - \lambda\frac{\partial}{\partial \mathbf{j}_i}\sum_{k=1}^{3n_g}\mathbf{j}_k\left[\mathbf{K}^T\mathbf{d}\right]_k & \\
-\lambda\frac{\partial}{\partial \mathbf{j}_i}\sum_{k=1}^{n_s}\mathbf{d}_k\left(\sum_{k=1}^{3n_g}\mathbf{K}_{kl}\mathbf{j}_l\right) + \lambda\frac{\partial}{\partial \mathbf{j}_k}\left(\sum_{k=1}^{3n_g}\mathbf{j}_k\left(\sum_{k=1}^{3n_g}\left[\mathbf{K}^T\mathbf{K}\right]_{kl}\mathbf{j}_l\right)\right) &= 0 \\
\beta\sum_{k=1}^{3n_g}\left(\delta_{ik}\mathbf{j}_k + \delta_{ik}\mathbf{j}_k\right) - \lambda\left[\mathbf{K}^T\mathbf{d}\right]_i - \lambda\sum_{k=1}^{n_s}\mathbf{d}_k\mathbf{K}_{ki} & \\
+\lambda\sum_{k,l=1}^{3n_g}\left(\delta_{ik}\left[\mathbf{K}^T\mathbf{K}\right]_{kl}\mathbf{j}_l + \lambda\delta_{il}\left[\mathbf{K}^T\mathbf{K}\right]_{kl}\mathbf{j}_k\right) &= 0 \\
2\beta\sum_{k=1}^{3n_g}\delta_{ik}\mathbf{j}_k - 2\lambda\left[\mathbf{K}^T\mathbf{d}\right]_i + 2\lambda\sum_{k=1}^{3n_g}\left[\mathbf{K}^T\mathbf{K}\right]_{ik}\mathbf{j}_k &= 0 \\
2\left(\alpha\mathbf{I}_{3n_g} + \mathbf{K}^T\mathbf{K}\right)\mathbf{j} &= 2\mathbf{K}^\mathbf{T}\mathbf{d}.
\end{aligned}
$$

where $\alpha = \beta/\lambda$. From the last equation we get that the PCD (**j**) can be obtained from the EEG/MEG data vector $\mathbf{m}$ in the following way:

$$
\mathbf{j}(\alpha) = \left(\mathbf{K}^T\mathbf{K} + \alpha\mathbf{I}_{3n_g}\right)^{-1}\mathbf{K}^T\mathbf{d}. \tag{A.1}
$$

From equation (A.1) we see that in order to find $\mathbf{j}$ we have to invert the matrix

$$\mathbf{K^T K} + \alpha \mathbf{I}_{3n_g},$$

which is of size $3n_g \times 3n_g$. From chapter (3) we know that n_g is in order of 3000 thus making this matrix large for performing an efficient matrix inversion. In order to find an efficient solution to this equation we appeal to the following matrix identity:

$$\left(\mathbf{K}^T\mathbf{K} + \alpha\mathbf{I}_{3n_g}\right)^{-1}\mathbf{K}^T = \mathbf{K}^T\left(\mathbf{K}\mathbf{K}^T + \alpha\mathbf{I}_{n_s}\right)^{-1}. \tag{A.2}$$

This identity can be proved as follow:

$$\begin{aligned}\mathbf{K}^T\left(\mathbf{K}\mathbf{K}^T + \alpha\mathbf{I}_{n_s}\right) &= \mathbf{K}^T\mathbf{K}\mathbf{K}^T + \alpha\mathbf{K}^T \\ &= \left(\mathbf{K}^T\mathbf{K} + \alpha\mathbf{I}_{3n_g}\right)\mathbf{K}^T,\end{aligned}$$

this gives

$$\mathbf{K}^T = \left(\mathbf{K}^T\mathbf{K} + \alpha\mathbf{I}_{3n_g}\right)\mathbf{K}^T\left(\mathbf{K}\mathbf{K}^T + \alpha\mathbf{I}_{n_s}\right)^{-1}$$

and finally

$$\left(\mathbf{K}^T\mathbf{K} + \mathbf{I}_{n_s}\right)^{-1}\mathbf{K}^T = \mathbf{K}^T\left(\mathbf{K}\mathbf{K}^T + \alpha\mathbf{I}_{n_s}\right)^{-1}. \tag{A.3}$$

Given equation (A.3) we can rewrite equation (A.1) as:

$$\mathbf{j}(\alpha) = \mathbf{K}^T\left(\mathbf{K}\mathbf{K}^T + \alpha\mathbf{I}_{n_s}\right)^{-1}\mathbf{d}.$$

in this equation the matrix we have to invert is of order $n_s \times n_s$ with $n_s \approx 300$. Moreover, this equation can be solved using the SVD decomposition which is based on the following linear algebra theorem: Any $M \times N$ matrix $\mathbf{A}$ whose number of rows M is greater than or equal to its number of columns N, can be written as the product of an $M \times N$ column-orthogonal matrix $\mathbf{U}$, and $N \times N$ diagonal matrix $\mathbf{S}$ with positive or zero elements (the *singular values*), and the transpose of an $N \times N$ orthogonal matrix $\mathbf{V}$:

$$\mathbf{A} = \mathbf{USV}$$

with

$$\sum_{i=1}^{M}\mathbf{U}_{ki}^T\mathbf{U}_{in} = \delta_{kn} \quad 1 \le k, n \le N \tag{A.4}$$

$$\sum_{i=1}^{N} \mathbf{V}_{ki}^T \mathbf{V}_{in} \quad = \delta_{kn} \quad 1 \leq k, n \leq N \tag{A.5}$$

The SVD decomposition can also be carried out when $M < N$. In this case the singular values S_j for $j = M+1, \ldots, N$ are all zero, and the corresponding columns of $\mathbf{U}$ are also zero. Equations (A.4) and (A.5) then holds only for $k, n \leq M$. The SVD decomposition can always be performed and its unique except to (i) making the same permutation of the columns of $\mathbf{U}$, elements of $\mathbf{S}$, and columns of $\mathbf{V}$ (or rows of $\mathbf{V}^T$), or (ii) forming linear combinations of any columns of $\mathbf{U}$ and $\mathbf{V}$ whose corresponding elements of $\mathbf{S}$ are exactly equal.

Using the SVD decomposition of the leadfield matrix $\mathbf{K}$ we can find a computation efficient algorithm to calculate $\mathbf{j}(\alpha)$ from equation (A.1). For that we can take:

$$\mathbf{K} = \mathbf{U}\mathbf{S}\mathbf{V}^T$$

so we have,

$$\begin{aligned} \mathbf{K}\mathbf{K}^T &= \left(\mathbf{U}\mathbf{S}\mathbf{V}^T\right)\left(\mathbf{U}\mathbf{S}\mathbf{V}^T\right)^T \\ &= \left(\mathbf{U}\mathbf{S}\mathbf{V}^T\right)\left(\mathbf{V}\mathbf{S}^T\mathbf{U}^T\right) \\ &= \mathbf{U}\mathbf{S}\mathbf{V}^T\mathbf{V}\mathbf{S}^T\mathbf{U}^T \\ &= \mathbf{U}\mathbf{S}\mathbf{S}^T\mathbf{U}^T \end{aligned} \tag{A.6}$$

where we have taken into account equation (A.5). Using equation (A.6) we have:

$$\begin{aligned} \left(\mathbf{K}\mathbf{K}^T + \alpha\mathbf{I}_{n_s}\right)^{-1} &= \left(\mathbf{U}\mathbf{S}\mathbf{S}^T\mathbf{U}^T + \alpha\mathbf{I}_{n_s}\right)^{-1} \\ &= \mathbf{U}\left(\mathbf{S}\mathbf{S}^T + \alpha\mathbf{I}_{n_s}\right)^{-1}\mathbf{U}^T \end{aligned}$$

we have made used of the following matrix inversion property:

$$(\mathbf{A}\mathbf{B})^{-1} = \mathbf{B}^{-1}\mathbf{A}^{-1}.$$

Finally multiplying by $\mathbf{K}^T = \mathbf{V}\mathbf{S}^T\mathbf{U}^T$ we get:

$$\begin{aligned} \mathbf{K}^T\left(\mathbf{K}\mathbf{K}^T + \alpha\mathbf{I}_{n_s}\right)^{-1} &= \mathbf{V}\mathbf{S}^T\mathbf{U}^T\mathbf{U}\left(\mathbf{S}\mathbf{S}^T + \alpha\mathbf{I}_{3n_g}\right)^{-1}\mathbf{U}^T \\ &= \mathbf{V}\frac{\mathbf{S}^T}{\left(\mathbf{S}\mathbf{S}^T + \alpha\mathbf{I}_{3n_g}\right)}\mathbf{U}^T \end{aligned}$$

From this equation we see that

$$\mathbf{j}(\alpha) = \mathbf{V}\frac{\mathbf{S}^T}{\left(\mathbf{S}\mathbf{S}^T + \alpha\mathbf{I}_{3n_g}\right)}\mathbf{U}^T\mathbf{d},$$

additionally,

$$\mathbf{j}_i = \sum_{j=1}^{n_s}\mathbf{T}_{ij}\mathbf{d}_j,$$

where

$$\begin{aligned}\mathbf{T}_{ij} &= \sum_{k=1}^{3n_g}\mathbf{V}_{ik}\left(\frac{\mathbf{S}^T}{\left(\mathbf{S}\mathbf{S}^T + \alpha\mathbf{I}_{3n_g}\right)}\mathbf{U}^T\right)_{kj} \\ &= \sum_{k=1}^{3n_g}\mathbf{V}_{ik}\left(\sum_{l}^{3n_g}\left[\frac{\mathbf{S}^T}{\left(\mathbf{S}\mathbf{S}^T + \alpha\mathbf{I}_{3n_g}\right)}\right]_{kl}\mathbf{U}^T_{lj}\right).\end{aligned}$$

Since $\mathbf{S}$ is an square diagonal matrix we get:

$$\left[\frac{\mathbf{S}^T}{(\mathbf{S}\mathbf{S}^T + \alpha\mathbf{I})}\right]_{kl} = \frac{\mathbf{S}^T_k\delta_{kl}}{\left(\mathbf{S}^2_k\delta_{kl} + \alpha\right)},$$

where $\mathbf{S}_k$ is the k diagonal element of $\mathbf{S}$.
Taking this into account we can rewrite T_{ij} as:

$$\mathbf{T}_{ij} = \sum_{k=1}^{3n_g}\mathbf{V}_{ik}\left(\frac{\mathbf{S}^T_k}{\left(\mathbf{S}^2_k + \alpha\right)}\right)\mathbf{U}^T_{kj}.$$

From this equation we can see that $\mathbf{T}_{ij}$ is well defined even for $k > n_s$ where the eigenvalues are 0 or close to 0 (null space of $\mathbf{K}$). It is for this eigenvalues where we observe the numerical relevance of the regularization parameter (α) which reduces the weighting for the data which are associated with the small singular values. Since the smallest singular values not only enhance the data (we multiply a value which tend to infinite), it also amplifies the noise in it. Therefore, depending on the level of noise in the data, we need different amounts of protection against the noise-amplifying effects of reconstruction using the small singular values, which essentialy consists in applying a large regularization.

B

Analytic Signal and Hilbert Transform

If $f(t)$ is a real function that can be represented by an inverse Fourier transform then we have the following relationship in the time domain:

$$s(t) = s^T(t) \tag{B.1}$$

but

$$s(t) = \frac{1}{2\pi}\int_{-\infty}^{\infty} S(w)e^{iwt}dw \tag{B.2}$$

taking the complex conjugate of equation () we get:

$$s^T(t) = \left[\frac{1}{2\pi}\int_{-\infty}^{\infty} S(w)e^{iwt}dw\right]^T = \frac{1}{2\pi}\int_{-\infty}^{\infty} S^T(w)e^{-iwt}dw$$

replacing w by $-w'$ we get:

$$s^T(t) = \frac{1}{2\pi}\int_{-\infty}^{\infty} S^T(-w')e^{iw't}dw \tag{B.3}$$

we have made use of:

$$\int_a^b f(x)\mathrm{d}x = -\int_b^a f(x)dx.$$

From equality (B.1) and comparing equations (B.2) and (B.3) we obtain the following relation:

$$S(w) = S^T(w)$$

or

$$S(-w) = S^T(w) \tag{B.4}$$

and we see that F for negative frequencies can be expressed by F^T for positives ones in the case of a

real value function. This mean that the positive frequency spectra is sufficient to represent a real signal.

Taking into account the redundancy of the negative frequency (equation (B.4)) we can define the following function:

$$z(t) = 2\frac{1}{\sqrt{2\pi}}\int_0^\infty S(w)e^{iwt}\mathrm{d}w,$$

but

$$S(w) = \frac{1}{\sqrt{2\pi}}\int s(t)e^{-iwt}\mathrm{d}t$$

therefore

$$z(t) = 2\frac{1}{2\pi}\int_0^\infty dw \int s(t')e^{-iwt'}e^{iwt}\mathrm{d}t'\mathrm{d}w.$$

Using the fact that

$$\int_0^\infty e^{iwx}\mathrm{d}w = \pi\delta(x) + \frac{i}{x}$$

we have

$$\int_0^\infty e^{iw(t-t')}\mathrm{d}w = \pi\delta(t-t') = \frac{i}{t-t'}$$

Hence

$$z(t) = 2\frac{1}{2\pi}\int s(t')\left(\pi\delta(t-t') + \frac{i}{t-t'}\right)\mathrm{d}t'$$

or

$$z(t) = s(t) + \frac{i}{\pi}\int \frac{s(t')}{t-t'}\mathrm{d}t'.$$

The second part is the Hilbert transform of the signal $s(t)$. From this equation is easy to deduce the linearity of the analytic signal discussed in section (4.2.1) as follow:

Given the function $f(t)$ as $c_1 f_1(t) + c_2 f_2(t)$ where the Hilbert transform of $f_1(t)$ and $f_2(t)$ exist then:

$$\begin{aligned}
\hat{H}f(t) &= \hat{H}\left(c_1 f_1(t) + c_2 f_2(t)\right) \\
&= \frac{i}{\pi}\int \frac{\left(c_1 f_1(t) + c_2 f_2(t)\right)}{t-t'}\mathrm{d}t' \\
&= c_1\frac{i}{\pi}\int \frac{f_1(t)}{t-t'}\mathrm{d}t' + c_2\frac{i}{\pi}\int \frac{f_2(t)}{t-t'}\mathrm{d}t' \\
&= c_1\hat{H}f_1(t) + c_2\hat{H}f_2(t).
\end{aligned}$$

Bibliography

E Alonso-Prieto, U Barnikol, E Palmero-Soler, K Dolan, G Hesselmann, H Mohlberg, K Amunts, K Zilles, M Niedeggen, and P Tass. Timing of v1/v2 and v5+ activations during coherent motion of dots: an meg study. *NeuroImage*, 37:1384–1395, 2007.

J Alvarez and E Emory. Executive function and the frontal lobes: a meta-analytic review. *Neuropsychol Rev*, 16(1):17–42, Mar 2006.

U Barnikol, K Amunts, J Dammers, H Mohlberg, T Fieseler, A Malikovic, K Zilles, M Niedeggen, and P Tass. Pattern reversal visual evoked responses of v1/v2 and v5/mt as revealed by meg combined with probabilistic cytoarchitectonic maps. *NeuroImage*, 31:86–108, 2006.

E Basar, C Basar-Eroglu, S Karakas, and M Schurmann. Are cognitive processes manifested in event-related gamma, alpha, theta and delta oscillations in the eeg? *Neurosci Lett*, 259(3):165–8, Jan 1999. 0304-3940 (Print) Journal Article Review.

U Baumgartner, H Vogel, J Ellrich, J Gawehn, P Stoeter, and R D Treede. Brain electrical source analysis of primary cortical components of the tibial nerve somatosensory evoked potential using regional sources. *Electroencephalogr Clin Neurophysiol*, 108(6):588–599, Nov 1998. ISSN 0013-4694 (Print).

T. E. J. Behrens, H. Johansen-Berg, M. W. Woolrich, S. M. Smith, C A. M. Wheeler-Kingshott, P. A. Boulby, G. J. Barker, E. L. Sillery, K. Sheehan, O. Ciccarelli, A. J. Thompson, J. M. Brady, and P. M. Matthews. Non-invasive mapping of connections between human thalamus and cortex using diffusion imaging. *ature Neuroscience*, (6):750 – 757, 2003.

J. S. Bendat and A. G. Piersol. *Random data: analysis and measurement procedures*. Wiley Press, 3rd edition, 2000. ISBN 0-471-31733-0.

B Benjamin and D Yekutieli. The control of the false discovery rate in multiple testing under dependency. *The Annals of Statistics*, 29(4):1165–1188, 2001.

J. Bhattacharya. Reduced degree of long-range phase synchrony in pathological human brain. *Acta Neurobiol*, (61):309–318, 2001.

E Bisiach, E Capitani, C Luzzatti, and D Perani. Brain and conscious representation of outside reality. *Neuropsychologia*, 19(4):543–51, 1981.

B Bland. The physiology and pharmacology of hippocampal formation theta rhythms. *Prog Neurobiol*, 26(1):1–54, 1986.

J Caplan, J Madsen, S Raghavachari, and M Kahana. Distinct patterns of brain oscillations underlie two basic parameters of human maze learning. *J Neurophysiol*, 86(1):368–80, Jul 2001.

M Corbetta, E Akbudak, T Conturo, A Snyder, J Ollinger, H Drury, M Linenweber, S Petersen, M Raichle, D Van Essen, and G Shulman. A common network of functional areas for attention and eye movements. *Neuron*, 21(4):761–73, Oct 1998.

M. Pievani C. Geroldi G. Binetti O. Zanetti K. Sosta P. Rossini G. Frisoni D. Moretti, C. Fracassi. Increase of theta/gamma ratio is associated with memory impairment. *Clinical Neurophysiology*, 120 (2):295–303, Feb 2009.

Anders M. Dale and Martin I. Sereno. Improved localization of cortical activity by combining eeg and meg with mri cortical surface reconstruction: A linear approach. *Journal of Cognitive Neuroscience*, 5:162–176, 1993.

Lachaux J.P. Baillet S. Garnero L.and Martinerie J. David O., Cosmelli D. A theoretical and experimental introduction to the non-invasive study of large-scale neural phase synchronization in human beings. *Journal of Computational Cognition*, 1(4):53–77, 2002.

M Deiber, P Missonnier, O Bertrand, G Gold, L Fazio-Costa, V Ibanez, and P Giannakopoulos. Distinction between perceptual and attentional processing in working memory tasks: a study of phase-locked and induced oscillatory brain dynamics. *J Cogn Neurosci*, 19(1):158–72, Jan 2007.

M Deiber, V Ibanez, P Missonnier, F Herrmann, L Fazio-Costa, G Gold, and P Giannakopoulos. Abnormal-induced theta activity supports early directed-attention network deficits in progressive mci. *Neurobiol Aging*, Jan 2008. 1558-1497 (Electronic) Journal article.

A Delorme, M Westerfield, and S Makeig. Medial prefrontal theta bursts precede rapid motor responses during visual selective attention. *J Neurosci*, 27(44):11949–59, Oct 2007.

K. Dolan. Surrogate analysis of multichannel data with frequency dependant time lag. *Fluctuation and Noise Letters*, 4(1):L75–L81, 2004.

K. Dolan and A. Neiman. Surrogate analysis of coherent multichannel data. *Phys. Rev. E*, 65:026108–1–6, 2002.

K. Dolan and M.L. Spano. Surrogate for nonlinear time series analysis. *Phys. Rev. E*, 64:046128, 2001.

J. S. Ebersole and P. B. Wade. Spike voltage topography and equivalent dipole localization in complex partial epilepsy. *Brain Topography*, 3(1):21–34, 09 1990. URL `http://dx.doi.org/10.1007/BF01128858`.

R. Eckhorn, R. Bauer, W. Jordan, M. Brosch, W. Kruse, M. Munk, and H.J. Reitboeck. Coherent oscillations: a mechanism of feature linking in the visual cortex. *Biol. Cybern.*, 60:121–130, 1998.

J Fan, J Byrne, M Worden, K Guise, B McCandliss, J Fossella, and M Posner. The relation of brain oscillations to attentional networks. *J Neurosci*, 27(23):6197–206, Jun 2007.

WJ Freeman. *Preface to brain function and oscillations*. 1998.

F Friedrich, R Egly, R Rafal, and D Beck. Spatial attention deficits in humans: a comparison of superior parietal and temporal-parietal junction lesions. *Neuropsychology*, 12(2):193–207, Apr 1998.

M. Fuchs, M. Wagner, T. Köhler, and H. Wischmann. Linear and nonlinear current density reconstructions. *J. Clin. Neurophysiol.*, 16(3):267–295, 1999.

D. Gabor. Theory of communication. *J. IEE*, 93:429–457, 1946.

David B. Geselowitz. On bioelectric potentials in an inhomogeneous volume conductor. *Biophys J.*, 7: 1–11, 1967.

David B. Geselowitz. On the magnetic field generated outside an inhomogeneous volume conductor by internal current sources. *IEEE Trans. Magn.*, 6:346–347, 1970.

A Gevins, M Smith, L McEvoy, and D Yu. High-resolution eeg mapping of cortical activation related to working memory: effects of task difficulty, type of processing, and practice. *Cereb Cortex*, 7(4): 374–85, Jun 1997.

D Gitelman, A Nobre, T Parrish, K LaBar, Y Kim, J Meyer, and M Mesulam. A large-scale distributed network for covert spatial attention: further anatomical delineation based on stringent behavioural and cognitive controls. *Brain*, 122 (Pt 6):1093–106, Jun 1999.

B Givens. Stimulus-evoked resetting of the dentate theta rhythm: relation to working memory. *Neuroreport*, 8(1):159–63, Dec 1996.

G. H. Golub, M. Heath, and G. Wahba. Generalized cross-validation as a method for choosinga good ridge parameter. *Technometric*, 21(2), 1979.

R. Grave de Peralta Menendez and S. Gonzalez Andino. A critical analysis of linear inverse solutions to the neuroelectromagnetic inverse problem. *IEEE Trans. Biomed. Eng.*, (45):440 – 448, 1998.

J. Gross, J. Kujala, M. Hämälä inen, L. Timmermann, A. Schnitzler, and R. Salmelin. Dynamic imaging of coherent sources: Studying neural interactions in the human brain. *PNAS*, 98(2):694–699, 2001.

M.S. Hämäläinen and R.J. Ilmoniemi. Interpreting magnetic fields of the brain: minimum norm estimates. *Med. Biol. Eng. Comput.*, 32:35–42, 1994.

M.S. Hämäläinen, R. Hari, J. Risto, R.J. Ilmoniemi, J. Knuutila, and O.V. Lounasmaa. Magnetoencephalography - theory, instrumentation, and applications to non-invasive studies of the working human brain. *Rev. Mod. Phys.*, 65(2), 1993.

K Heilman, R Watson, E Valenstein, K Heilman, and E Valenstein. *Neglect and related disorders*, pages 243–293. 1985.

H. Helmholtz. Ueber einige Gesetze der Vertheilung elektrischer Ströeme in körperlichen Leitern mit Anwendung auf die thierisch-elektrischen Versuche. *Ann. Physik und Chemie*, 9(8):211–33, 1853.

C Herrmann and A Mecklinger. Magnetoencephalographic responses to illusory figures: early evoked gamma is affected by processing of stimulus features. *Int J Psychophysiol*, 38(3):265–81, Dec 2000. 0167-8760 (Print) Clinical Trial Journal Article.

C Herrmann and A Mecklinger. Gamma activity in human eeg is related to hig-speed memory comparison during object selective attention. *Vis. Cogn*, 8:593–608, 2001.

S Hillyard and L Anllo-Vento. Event-related brain potentials in the study of visual selective attention. *Proc Natl Acad Sci U S A*, 95(3):781–7, Feb 1998.

K. Hoechstetter, A. Rupp, A. Stancák, HM. Meinck, C. Stippich, P. Berg, and M. Scherg. Interaction of tactile input in the human primary and secondary somatosensory cortex–a magnetoencephalographic study. *Neuroimage.*, 14(3):759–67, Sep 2001.

C Holscher, R Anwyl, and M Rowan. Stimulation on the positive phase of hippocampal theta rhythm induces long-term potentiation that can be depotentiated by stimulation on the negative phase in area ca1 in vivo. *J Neurosci*, 17(16):6470–7, Aug 1997.

J Hopfinger, M Buonocore, and G Mangun. The neural mechanisms of top-down attentional control. *Nat Neurosci*, 3(3):284–91, Mar 2000.

J Hopfinger, S Luck, S Hillyard, and M Gazzaniga. *Selective attention: Electrophysiological and neuromagnetic studies*, pages 561–574. 2004.

P Huerta and J Lisman. Heightened synaptic plasticity of hippocampal ca1 neurons during a cholinergically induced rhythmic state. *Nature*, 364(6439):723–5, Aug 1993. 0028-0836 (Print) In Vitro Journal Article.

Jose M Hurtado, Leonid L Rubchinsky, and Karen A Sigvardt. Statistical method for detection of phase-locking episodes in neural oscillations. *J Neurophysiol*, 91(4):1883–1898, 2004. ISSN 0022-3077 (Print). doi: 10.1152/jn.00853.2003.

N Ille, P Berg, and M Scherg. Artifact correction of the ongoing eeg using spatial filters based on artifact and brain signal topographies. *J Clin Neurophysiol*, 19(2):113–24, Apr 2002.

K Inanaga. Frontal midline theta rhythm and mental activity. *Psychiatry Clin Neurosci*, 52(6):555–66, Dec 1998. 1323-1316 (Print) Journal Article Review.

A A Ioannides, M J Liu, L C Liu, P D Bamidis, E Hellstrand, and K M Stephan. Magnetic field tomography of cortical and deep processes: examples of "real-time mapping" of averaged and single trial meg signals. *Int J Psychophysiol*, 20(3):161–175, Dec 1995. ISSN 0167-8760 (Print).

A.A. Ioannides, J.P.R. Bolton, and C.J.S. Clarke. Continuous probabilistic solutions to the biomagnetic inverse problem. *Inverse Probl.*, 6:523–542, 1990.

O Jensen and J Lisman. Position reconstruction from an ensemble of hippocampal place cells: contribution of theta phase coding. *J Neurophysiol*, 83(5):2602–9, May 2000.

E Juergens, A Guettler, and R Eckhorn. Visual stimulation elicits locked and induced gamma oscillations in monkey intracortical- and eeg-potentials, but not in human eeg. *Exp Brain Res*, 129(2):247–59, Nov 1999.

M Jurado and M Rosselli. The elusive nature of executive functions: a review of our current understanding. *Neuropsychol Rev*, 17(3):213–33, Sep 2007. 1040-7308 (Print) Journal Article Review.

Enrico Kaden, Alfred Anwander, and Thomas R Knosche. Variational inference of the fiber orientation density using diffusion mr imaging. *Neuroimage*, 42(4):1366–1380, Oct 2008. ISSN 1095-9572 (Electronic). doi: 10.1016/j.neuroimage.2008.06.004.

M Kahana. The cognitive correlates of human brain oscillations. *J Neurosci*, 26(6):1669–72, Feb 2006.

M Kahana, R Sekuler, J Caplan, M Kirschen, and J Madsen. Human theta oscillations exhibit task dependence during virtual maze navigation. *Nature*, 399(6738):781–4, Jun 1999.

M Kahana, D Seelig, and J Madsen. Theta returns. *Curr Opin Neurobiol*, 11(6):739–44, Dec 2001.

S Kastner, M Pinsk, P De Weerd, R Desimone, and L Ungerleider. Increased activity in human visual cortex during directed attention in the absence of visual stimulation. *Neuron*, 22(4):751–61, Apr 1999.

S Kelly, E Lalor, R Reilly, and J Foxe. Increases in alpha oscillatory power reflect an active retinotopic mechanism for distracter suppression during sustained visuospatial attention. *J Neurophysiol*, 95(6): 3844–51, Jun 2006.

W Klimesch. Eeg alpha and theta oscillations reflect cognitive and memory performance: a review and analysis. *Brain Res Brain Res Rev*, 29(2-3):169–95, Apr 1999.

Th. Kohler, M. Wagner, M. Fuchs, H.-A. Wischmann, Drenckhahn R., and A. Theiben. Depth Normalization in MEG/EEG Current Density Imaging. *Engineering in Medicine and Biology Society, 1996. Bridging Disciplines for Biomedicine. Proceedings of the 18th Annual International Conference of the IEEE.*, 2, 31 October 1996.

C Krause, L Sillanmaki, M Koivisto, C Saarela, A Haggqvist, M Laine, and H Hamalainen. The effects of memory load on event-related eeg desynchronization and synchronization. *Clin Neurophysiol*, 111 (11):2071–8, Nov 2000.

Y. Kuramoto. *Chemical Oscillations, Waves and Turbulence*. Springer-Verlag, Berlin, 1984.

J P Lachaux, E Rodriguez, J Martinerie, and F J Varela. Measuring phase synchrony in brain signals. *Hum Brain Mapp*, 8(4):194–208, 1999. ISSN 1065-9471 (Print).

Jean-Philippe Lachaux, Antoine Lutz, David Rudrauf, Diego Cosmelli, Michel Le Van Quyen, Jacques Martinerie, and Francisco Varela. Estimating the time-course of coherence between single-trial brain signals: an introduction to wavelet coherence. *Neurophysiol Clin*, 32(3):157–174, Jun 2002.

V Lamme and P Roelfsema. The distinct modes of vision offered by feedforward and recurrent processing. *Trends Neurosci*, 23(11):571–9, Nov 2000. 0166-2236 (Print) Journal Article Review.

V Lamme and H Spekreijse. Neuronal synchrony does not represent texture segregation. *Nature*, 396 (6709):362–6, Nov 1998.

L. D. Landau and E. M. Lifshitz. *The classical theory of fields*. Pergamon Press, 1962.

G Lantz, M Holub, E Ryding, and I Rosen. Simultaneous intracranial and extracranial recording of interictal epileptiform activity in patients with drug resistant partial epilepsy: patterns of conduction and results from dipole reconstructions. *Electroencephalogr Clin Neurophysiol*, 99(1):69–78, 1996. ISSN 0013-4694 (Print).

M. A. Lebedev and M. A. Nicolelis. Brain-machine interfaces: past, present and future. *Trends Neurosci*, (29):536–546, 2006.

S Luck, S Hillyard, M Mouloua, and H Hawkins. Mechanisms of visual-spatial attention: resource allocation or uncertainty reduction? *J Exp Psychol Hum Percept Perform*, 22(3):725–37, Jun 1996.

S Luck, L Chelazzi, S Hillyard, and R Desimone. Neural mechanisms of spatial selective attention in areas v1, v2, and v4 of macaque visual cortex. *J Neurophysiol*, 77(1):24–42, Jan 1997.

P Luu, D Tucker, and S Makeig. Frontal midline theta and the error-related negativity: neurophysiological mechanisms of action regulation. *Clin Neurophysiol*, 115(8):1821–35, Aug 2004.

J Lynch and J McLaren. Deficits of visual attention and saccadic eye movements after lesions of parietooccipital cortex in monkeys. *J Neurophysiol*, 61(1):74–90, Jan 1989.

David J. C. Mackay. Bayesian interpolation. *Neural Computation*, 4:415–447, 1992.

K. V. Mardia, J.T. Kent, and J.M. Bibby. *Multivariate analysis*. Academic Press, 1979. ISBN 0-12-471250-9.

A Martinez, L Anllo-Vento, M Sereno, L Frank, R Buxton, D Dubowitz, E Wong, H Hinrichs, H Heinze, and S Hillyard. Involvement of striate and extrastriate visual cortical areas in spatial attention. *Nat Neurosci*, 2(4):364–9, Apr 1999.

A Martinez, F DiRusso, L Anllo-Vento, M Sereno, R Buxton, and S Hillyard. Putting spatial attention on the map: timing and localization of stimulus selection processes in striate and extrastriate visual areas. *Vision Res*, 41(10-11):1437–57, 2001.

A Martinez, W Teder-Salejarvi, and S Hillyard. Spatial attention facilitates selection of illusory objects: evidence from event-related brain potentials. *Brain Res*, 1139:143–52, Mar 2007. 0006-8993 (Print) Journal Article.

P Missonnier, M Deiber, G Gold, P Millet, M Gex-Fabry Pun, L Fazio-Costa, P Giannakopoulos, and V Ibanez. Frontal theta event-related synchronization: comparison of directed attention and working memory load effects. *J Neural Transm*, 113(10):1477–86, Oct 2006.

A Nobre, G Sebestyen, D Gitelman, M Mesulam, R Frackowiak, and C Frith. Functional localization of the system for visuospatial attention using positron emission tomography. *Brain*, 120 (Pt 3):515–33, Mar 1997. 0006-8950 (Print) Clinical Trial Journal Article.

J O'Keefe and M Recce. Phase relationship between hippocampal place units and the eeg theta rhythm. *Hippocampus*, 3(3):317–30, Jul 1993.

R. K. Otnes and L. Enochson. *Digital Time Series Analysis*. Wiley Press, New York, 1972.

N. Papp and P. Ktonas. Critical evaluation of complex demodulation techniques for the quantification of bioelectrical activity. *Biomed Sci Instrum*, 13:135–145, 1977.

R.D. Pascual-Marqui. Standardized low resolution brain electromagnetic tomography (sLORETA): technical details. *Method. Find. Exp. Clin.*, 24D:5–12, 2002.

L. N. Paul and S. Ramesh. *Electric Fields of the Brain: The Neurophysics of EEG*. Oxford University Press, 2 edition, 2006.

L Pessoa, S Kastner, and L Ungerleider. Neuroimaging studies of attention: from modulation of sensory processing to top-down control. *J Neurosci*, 23(10):3990–8, May 2003.

M. Pohja, S. Salenius, and R. Hari. Reproducibility of cortex-muscle coherence. *Neuroimage*, 26: 764–70, 2005.

S Raghavachari, M Kahana, D Rizzuto, J Caplan, M Kirschen, B Bourgeois, J Madsen, and J Lisman. Gating of human theta oscillations by a working memory task. *J Neurosci*, 21(9):3175–83, May 2001.

M.G. Rosenblum, A.S. Pikovsky, J. Kurths, C. Schäfer, and P.A. Tass. *Handbook of Biological Physics*, volume 4, chapter Phase Synchronization: From Theory to Data Analysis, pages 279–321. Elsevier Science, 2001.

Michael Rosenblum and Arkady Pikovsky. Synchronization: from pendulum clocks to chaotic lasers and chemical oscillators. *Contemporary Physics*, 44(5):401–416, Jan 2003. doi: 10.1080/0010751031000160312 9.

F Di Russo, A Martinez, M Sereno, S Pitzalis, and S Hillyard. Cortical sources of the early components of the visual evoked potential. *Hum Brain Mapp*, 15(2):95–111, Feb 2002. 1065-9471 (Print) Journal Article.

F Di Russo, A Martinez, and S Hillyard. Source analysis of event-related cortical activity during visuo-spatial attention. *Cereb Cortex*, 13(5):486–99, May 2003.

J. Sarvas. Basic mathematical and electromagnetic concepts of the biomagnetic inverse problem. *Phys. Med. Biol.*, 32(1):11–22, 1987.

W Singer. Search for coherence: a basic principle of cortical self-organization. *Concepts Neurosci.*, 1: 1–26, 1989.

W Skaggs, B McNaughton, M Wilson, and C Barnes. Theta phase precession in hippocampal neuronal populations and the compression of temporal sequences. *Hippocampus*, 6(2):149–72, 1996.

P Spiers, D Schomer, H Blume, J Kleefield, G O'Reilly, S Weintraub, P Osborne-Shaefer, and M Mesulam. Visual neglect during intracarotid amobarbital testing. *Neurology*, 40(10):1600–6, Oct 1990.

V. Strelets, Zh. Garakh, V. Novototskii-Vlasov, and R. Magomedov. Relationship between eeg power and rhythm synchronization in health and cognitive pathology. *Neuroscience and Behavioral Physiology*, 36(6):655–662, 07 2006. URL `http://dx.doi.org/10.1007/s11055-006-0070-4`.

S. M. Tan and C. Fox. Inverse problems 453.707 class notes. *The University of Auckland, Aucland, New Zealand*, 2001.

A. Tarantola. *Inverse Problem Theory*. Elsevier, The Netherlands (ISBN 0-444-42765-1), 1987.

P. Tass, M. G. Rosenblum, J. Weule, J. Kurths, A. Pikovsky, J. Volkmann, A. Schnitzler, and H.J. Freund. Detection of n: m phase locking from noisy data: Application to magnetoencephalography. *Phys. Rev. Lett.*, 81(15):3291–3294, 1998.

P. A. Tass. Phase and frequency shifts of two nonlinearly coupled oscillator. *Phys. Rev. B*, 99(1):111–121, 1995.

P.A. Tass. *Phase Resetting in Medicine and Biology: Stochastic Modelling and Data Analysis*. Springer-Verlag, Berlin, 1999.

P.A Tass. Transmission of stimulus-locked responses in two coupled phase oscillators. *Phys. Rev. E*, 69: 051909–1–24, 2004.

P.A. Tass, T. Fieseler, J. Dammers, K. Dolan, P. Morosan, M. Majtanik, F. Boers, A. Muren, K. Zilles, and G.R. Fink. Synchronization tomography: a method for three-dimensional localization of phase synchronized neuronal populations in the human brain using magnetoencephalography. *Phys. Rev. Lett.*, 90(8):088101, 2003.

J G Taylor, A A Ioannides, and H W Muller-Gartner. Mathematical analysis of lead field expansions. *IEEE Trans Med Imaging*, 18(2):151–163, Feb 1999. ISSN 0278-0062 (Print). doi: 10.1109/42.759120.

A. N. Tikhonov and V. Y. Arsenin. *Solutions of Ill-Posed Problems*. W. H. Winston, Washington, DC., 1997.

M Tovee and E Rolls. Oscillatory activity is not evident in the primate temporal visual cortex with static stimuli. *Neuroreport*, 3(4):369–72, Apr 1992.

L. G. Ungerleider and R. Desimone. Projections to the superior temporal sulcus from the central and peripheral field representations of v1 and v2. *J Comp Neurol*, 248(2):147–63, 1986.

F. Varela, J. Lachaux, E. Roriguez, and J. Martinerie. The brainweb: Phase synchronization and large-scale integration. *Nat. Rev. Neurosci.*, 2(4):229–239, 2001.

M. Wagner. *Rekonstruktion neuronaler strome*. Shaker Verlag, Aachen, 1998.

M. Wagner, M. Fuchs, and J. Kastner. Evaluation of sLORETA in the presence of noise and multiple sources. *Brain Topogr.*, 16(4):277–280, 2004.

R Watson, E Valenstein, A Day, and K Heilman. Posterior neocortical systems subserving awareness and neglect. neglect associated with superior temporal sulcus but not area 7 lesions. *Arch Neurol*, 51 (10):1014–21, Oct 1994.

Sabine Weiss and Horst M Mueller. The contribution of eeg coherence to the investigation of language. *Brain Lang*, 85(2):325–343, 2003. ISSN 0093-934X (Print).

A. M. Whittington. Can brain rhythms inform on underlying pathology in schizophrenia? biological psychiatry. 63(8):728–729, April 2008.

S.J. Williamson and L Kaufmann. *Theory of Neuroelectric and Neuromagnetic Fields*, volume 6, pages 1–39. Auditory evoked Magnetic Fields and electric Potentials, 1990.

A.T. Winfree. *The Geometry of Biological Time*. Springer-Verlag, New York, 2001.

M Young, K Tanaka, and S Yamane. On oscillating neuronal responses in the visual cortex of the monkey. *J Neurophysiol*, 67(6):1464–74, Jun 1992.

M. P. Young. Objective analysis of the topological organization of the primate cortical visual system. *Nature*, 358(6382):152–5, 1992.

S Yuval-Greenberg, O Tomer, A Keren, I Nelken, and L Deouell. Transient induced gamma-band response in eeg as a manifestation of miniature saccades. *Neuron*, 58(3):429–41, May 2008.

S. Zeki. Functional specialization in the visual cortex of the rhesus monkey. *Nature*, 274:423–428, 1978.